Cyprus University of Technology

Faculty of Engineering and Technology
Department of Mechanical Engineering and Material Science and Engineering

Doctoral Thesis

"Metal-oxide interfaces and additive engineering for high performance perovskite solar cells"

Apostolos Ioakeimidis

Supervisor: Professor Stelios A. Choulis

Limassol, 23 November 2021

“Metal-oxide interfaces and additive engineering for high performance perovskite solar cells”

Presented by

Apostolos Ioakeimidis

B.Sc. Physics, Aristotle University of Thessaloniki
M.Sc. Nanoscience and Nanotechnology, Aristotle University of Thessaloniki

Submitted to the Department of Mechanical Engineering and Materials Science and Engineering, Cyprus University of Technology
in partial fulfillment of the requirements for the degree

Doctor of Philosophy

CYPRUS UNIVERSITY OF TECHNOLOGY

Supervisor:

Prof. Stelios Choulis

Committee Member

Prof. Monica Lira-Cantu

Committee Member (President)

Associate Professor Yulia Galagan

Limassol, 23 November 2021

Declaration

I declare that, except where otherwise stated, this dissertation is entirely my own work and has not been submitted in any form to any other University for any degree.

Apostolos Ioakeimidis

Acknowledgments

I would like to express my deep and sincere gratitude to my supervising Professor Stelios Choulis for giving me the opportunity to be member of his research group Molecular Electronics and Photonics (MEP) as well as for the continuous support and guidance during my Doctoral candidature. My sincere thanks also to my PhD advisory committee members, Associated Prof. Gregorios Itskos and Assistant Prof. Polyvios Eleftheriou for their valuable comments and advices on my PhD yearly progress reports. I would also like to thank European Union which under the European Research Council's (ERC) Horizon 2020 research and innovation Funding (grant agreement No. 647311) financially support this Thesis as well as the Cyprus University of Technology and the Department of Mechanical Engineering and Materials Science and Engineering for their technical and financial support.

Furthermore, I would like to express my special thanks to Associate Professor Gerasimos Armatas and Prof. Stella kennou who supported my scientific research investigation as well as my colleagues Dr. Ioannis Papadas, Dr. Dimitris Tsikritzis, Dr. Efthymios Georgiou, Dr. Panayiotis Pouloupatis, Fedros Galatopoulos, Sergey Pozov, Aleksandra Chrysou and Ioanna Antoniou for the pleasant and professional cooperation I always have with them.

With all my hurt I would like to thank my family and friends for their total support through all these year

Abstract

The need for renewable energy sources has become a necessity for a prosperous future of human society. Moreover, for the establishment of renewable technologies it is demanded to lower even more the cost. Thus, perovskite solar cells, as a promising candidate for the next generation PVs, require new materials and processes in order to increase the reliability and power conversion efficiency while also lower the cost enabling perovskite PVs to become a competitive, mainstream PV technology.

In this Thesis, it is first shown the fabrication of metal-oxide $NiCo_2O_4$ thin film using doctor blade coating, which is synthesized by the low-energy demanding synthesis of solution combustion. The film is introduced as an efficient hole transporting layer (HTL) layer in a 230 nm thick $MAPbI_3$ perovskite active layer for the fabrication of solar cells. The devices deliver a PCE in the range of 15.5 %, with negligible hysteresis for a 15 nm optimum thickness $NiCo_2O_4$ layer. A thicker $MAPbI_3$ perovskite layer (~350 nm) was applied to enhance the PCE of the devices, following the literature reported optimum thickness for the particular perovskite formulation. The resulted perovskite solar cells exhibited a lower PCE mainly due to a reduction of the fill factor and Voc, ascribed to higher recombination at the $NiCo_2O_4$/perovskite interface given that a higher number of hole charge carriers reach the interface before they are collected. To overcome this limitation $NiCo_2O_4$ is further modified by co-doping with Li and Cu improving the selectivity and transport properties of the contacts by proper modifications of the energetic levels and by increasing the electrical conductivity of the charge carriers, respectively. The engineered Cu, Li doped $NiCo_2O_4$

resulted in higher PCE perovskite solar cells (16.5%) due to improved interface properties.

Then, by deeper investigation of the solution combustion synthesis method, we study a range of applied temperatures (150, 200 and 300 ^{o}C) and fuel concentration (acetylacetonate) (without, 0.1 and 1.5 ratio to oxidizer) for the fabrication of metal-oxide Cu:NiOx. The objective was to identify the lowest required temperature for the synthesis of functional and high performing Cu:NiOx HTL for use as HTL in perovskite solar cells. It is revealed that solution combustion synthesis behavior of Cu:NiOx films is different compared to bulk analogues, supporting reports which concluded that the low temperature solution combustion synthesis of crystalline materials is unlikely to occur in thin films. Specifically, we show that the required temperature for the synthesis of crystalline Cu:NiOx films in around 300 ^{o}C which is higher compared to bulk analogue where a complete combustion process occurs at ~150 ^{o}C resulting in crystalline bulk forms. The various temperature and fuel concentration processed Cu:NiOx films were introduces in $Cs_{0.04}(MA_{0.17}FA_{0.83})_{0.96}$ $Pb(I_{0.83}Br_{0.17})_3$ based perovskite solar cells showing that the devices annealed at temperatures 150 and 200 ^{o}C delivered limited PCE solar cells, while on the other hand the 300 ^{o}C annealed Cu:NiOx resulted in high performing perovskite solar cells. The highest performing devices obtained for Cu:NiOx precursor ink annealed at 300^{o}C containing 0.1 ration of acetyl acetonate delivering a PCE of 16.58 %.

Finally, by applying the optimized conditions for the combustion synthesis (300 ^{o}C and 0.1 ratio acetylacetonate) undoped NiOx films are used as HTL in perovskite solar cells based on the methylammonium free perovskite formulation $CsFAPBI_3$

where the hybrid perovskite active layer was engineered by molecular additive to improve the reliability and the humidity degradation resistance. Nitrobenzene was selected as additive (1% v/v) considering the nitro group which can interact with PbI_6 cage of the perovskite leading to a passivation effect and the benzene group is a hydrophobic group that can protect from moisture ingress. The engineered devices delivered a higher Voc compared to unmodified reference with the best devices PCE in the range of 18 %, ascribed to structural defect passivation. Also, the additive based devices delivered a higher mean PCE with much narrower distribution due to reduced roughness/thickness inhomogeneity of the perovskite layer. The additive usage improved the air stability with the most stable device retaining over 85% of its initial PCE after 1500 h in air, whereas the additive-free devices decline by more than 65%. Improved humidity degradation resistance was further demonstrated by accelerated humidity study (75% relative humidity (RH)) confirming the enhancement of devices stability owing to the defect passivation and inhibition of moisture permeation effects induced by the use of Nitrobenzene.

Table of Content

List of Figures

List of Tables

Abbreviations

PCE power convention efficiency

TWh terawatt-hours

PV photovoltaic

LCOE levelized cost of electricity

MW MegaWatt

DC direct current

VBM valence band maximum

CBM conduction band minimum

PVSC perovskite solar cells

ETL electron transporting layer

HTL hole transporting layer

TCO transparent conductive oxide

ITO indium-doped tin oxide

FTO fluorine-doped tin oxide

SEM scanning electron microscopy

PVD physical vapor deposition

AFM atomic force microscopy

SPM scanning probe microscopy

STM scanning tunneling microscopy

UV-Vis ultraviolet - visible

PL photoluminance

XPS X-ray photoelectron spectra

UPS Ultraviolet photoelectron spectra

EIS electro impedance spectroscopy

M-S Mott-Schotttky

TEM transmission electron microscopy

HRTEM high resolution transmission electron microscopy

SAED selected area electron diffraction

XRD X-ray diffraction

J-V current density - Voltage

EQE external quantum efficiency

IQE internal quantum efficiency

NP nanoparticle

BE binding energy

1 Introduction

According to physical science the energy is defined as the capacity of doing work and it may exist in various forms, such as, kinetic, potential, thermal, electrical, chemical etc. which can neither created nor destroyed (first law of thermodynamics) but interconverted to various forms. World's evolution is related to the ability of various systems to harvest and convert energy in usable forms; Thus, human society, as one of such systems, needs energy in order to survive and develop. Moreover, throughout human history the dominant civilizations are characterize not only by the ability to transform energy in usable forms but also by the efficiency that can achieve this.[1] Consequently, high power (energy amount per time period) conversion efficiency (PCE) systems are prerequisite for the advancement of the human society.

A stricter relationship between the energy and a rapid economic development was established after the industrial revolution during the nineteenth century driven by the invention of highly efficient fossil-fueled internal combustion engine which replaced wood-fueled steam engine (Figure 1.1).

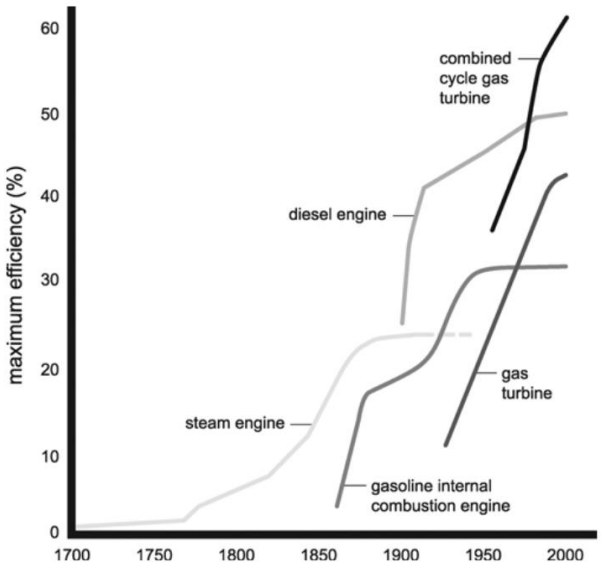

Figure 1.1 Maximum efficiency of prime movers, 1700–2000. There has been an order of magnitude gain during the last two centuries, from about 6% for steam engines to about 60% for the combined-cycle gas turbines.[2]

The higher energy density (amount of energy per gram) of fossil fuels compared to wood fuels led to an increase in the energy consumption (Figure 1.2) but it also marked the beginning of the current anthropogenic geological epoch.[3] Thus, the realization of the finite amounts of fossil fuels as well as the climate change related to man-made carbon dioxide emissions (Figure 1.3), despite the rapid development of the global economy, have raised concerns about the viability and sustainability of the current society development model.

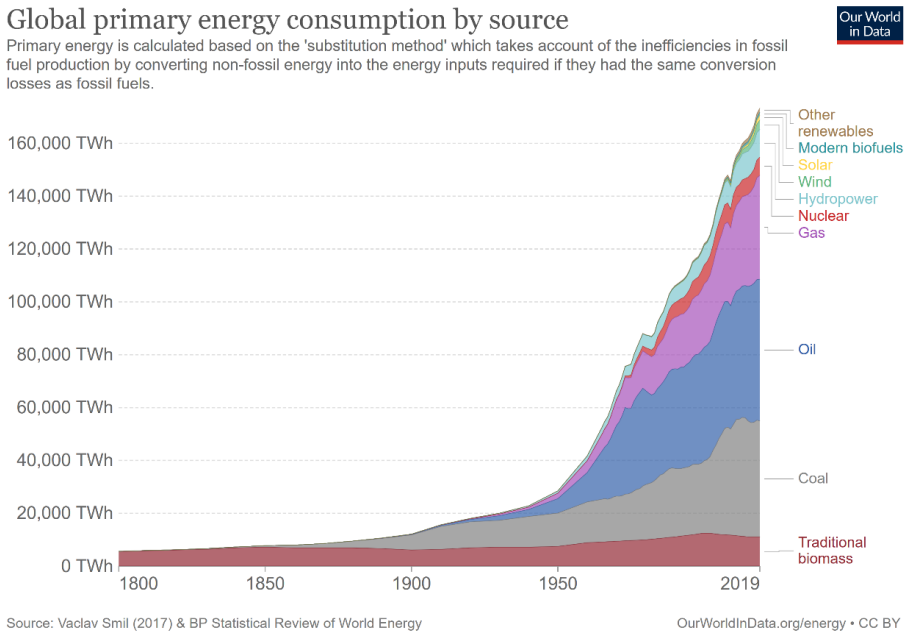

Figure 1.2 Global primary energy consumption, measured in terawatt-hours (TWh) per year. [4]

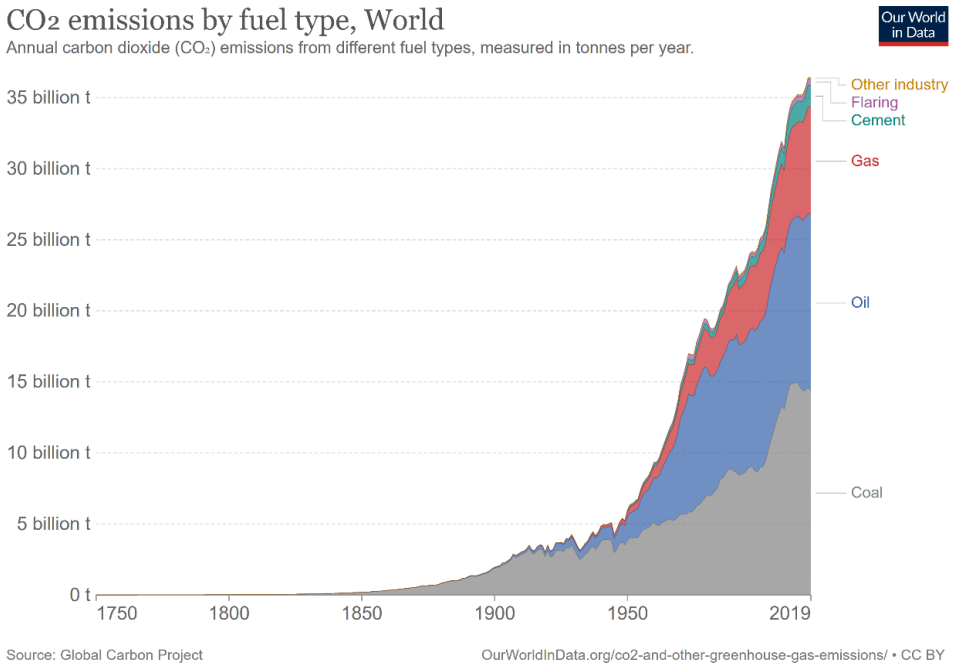

Figure 1.3 Global CO_2 emissions from different fuel types 1750-2019, measured in tonnes per year.[5]

To address this issue, it should be reduced the dependence on fossil fuel either by lowering the energy demands applying energy saving strategies and/or using renewable energy resources which are inexhaustible and much less pollutant. Regarding the use of renewable resources it is known that these energy convention systems are less competitive compare to established systems, but they have the significant advantage of reduced carbon emissions.[6] Over the past decades the energy consumption from renewable sources has been increased but it stills lagging far behind the traditional sources (Figure 1.2). European Union has set the targets for fulfilling at least 20% of its total energy needs with renewables by 2020.[7] Depending on the renewable resource that is used for the energy conversion the systems are divided accordingly, i.e solar, wind, geothermal, hydroelectric energy systems and each one has its own advantages.[8] Concerning the solar energy, around 100,000 Terawatt (TW) hit the earth's surface which can meet by far the current global consumption of primary energy (157,133 Terawatt hour (TWh) per year)[9]; Various technologies have been developed to harness this energy and they can organized according to the energy conversion path that is used - i.e., photon-to-electric, photon-to-chemical, and photon-to-thermal-to-electric. (Figure 1.4).[10]

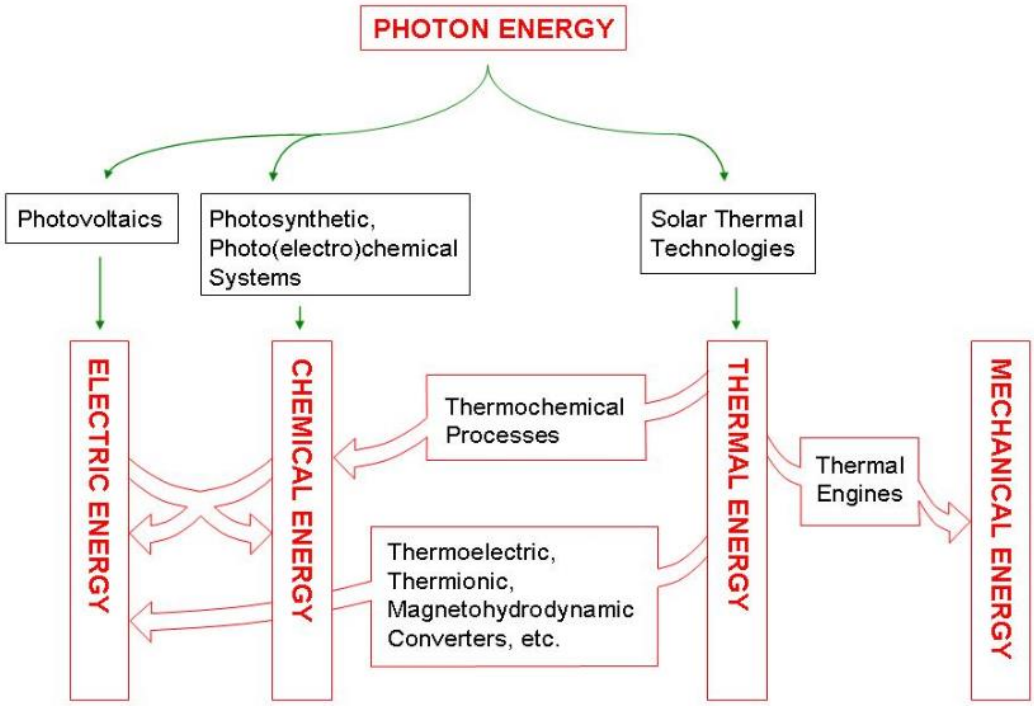

Figure 1.4 Solar energy conversion paths and technologies. [10]

The photon-to-electron conversion is realized through the photovoltaic phenomenon using photovoltaic systems (PV). These systems offer several discrete advantages over the other technologies, such as environmental friendliness, non-pollutive and low maintenance cost. On the other hand the main disadvantages were the toxic chemical wastes that are used during the production process, and the higher production cost compare to the most of the renewable technologies.[11] Over the last years the global levelized cost of electricity (LCOE) for the PVs (Figure 1.5) has experienced a steep decrease compare to other main renewable technologies thanks among other to the intense research and development of advanced PVs, while as of the 2019 the LCOE is around 0.068 $/KWh for Utility-scale PV.[12] As a result the global installed solar power capacity (Figure 1.6) has significantly increased to 707.50 GW by 2020 rendering PVs a mainstream solar technology.

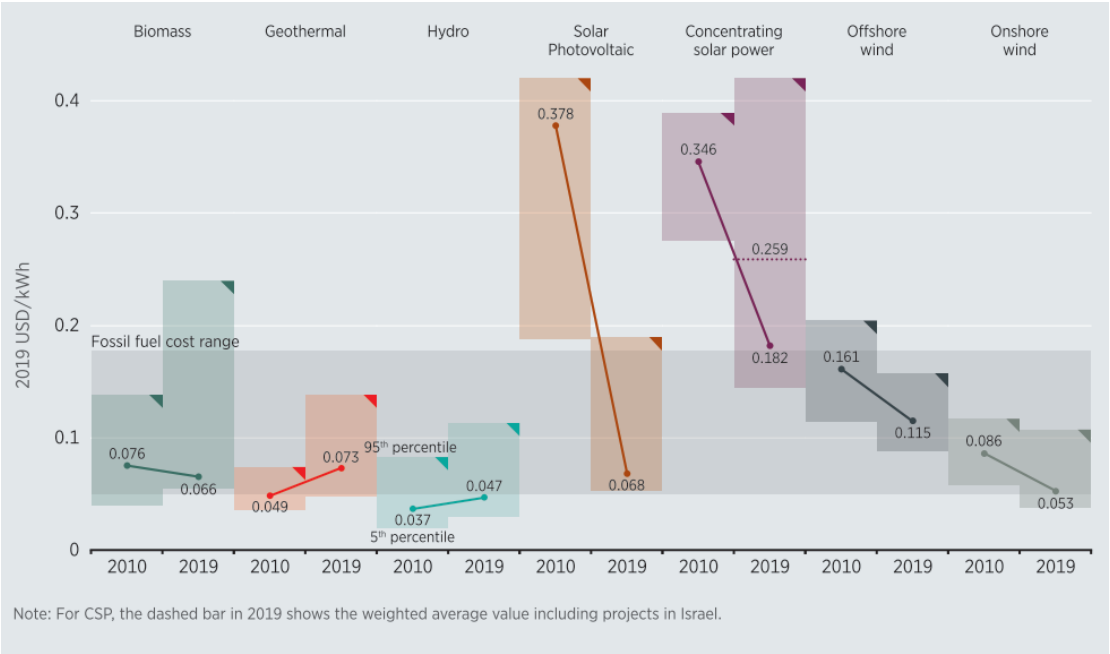

Figure 1.5 Trends in global renewable energy levelized cost of electricity in the time period from 2010 until 2019.[12]

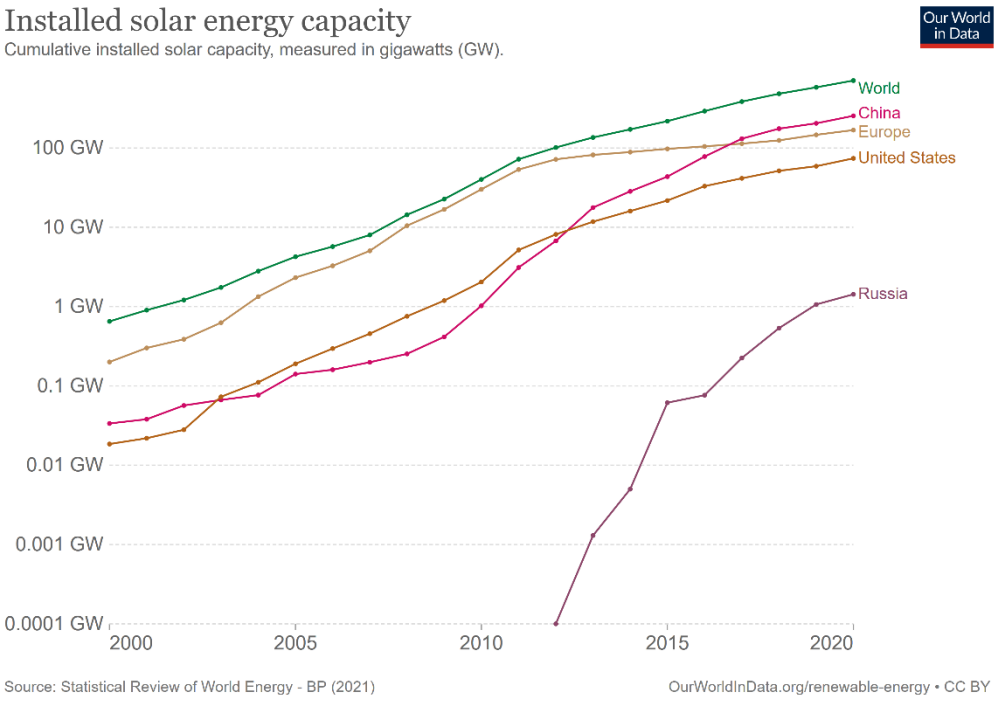

Figure 1.6 Global installed solar power capacity, 2000-2020 MW)[13]

1.1 Photovoltaic Technologies

PV systems are composed of multiple photovoltaic cells (also called solar cells) that generate electric power by converting sunlight to direct electric (DC) current. The conversion is performed by semiconducting materials which exhibit the photovoltaic effect. The latter was first observed by Edmond Becquerel in 1839 and even though it was demonstrated in an electrochemical cell, it usually occurs in semiconductors which are excited by energetically sufficient light producing voltage, the so-called photovoltage. The photovoltaic effect can also be observed in a semiconductor upon heating by a source, like light, inducing a thermal gradient which creates voltage through Seebeck effect.

Since the fabrication of the first low efficiency (~1%) solar cell by Fritz in 1883 a lot of breakthrough innovations in materials, structures and processes have enabled efficiencies higher than 40%.[14] These numerous changes that have been implemented throughout these years have led to a classification of the PV technologies based on generation (Figure 1.7) or the primary active material (Figure 1.8).[15,16]

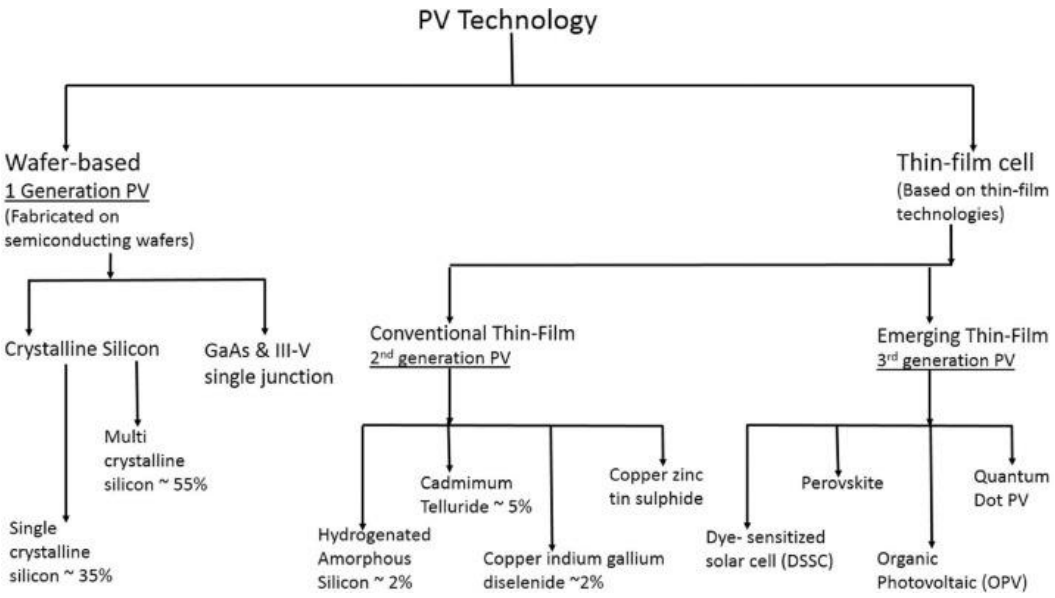

Figure 1.7 Generation PV classification of photovoltaic technologies with their current market share in percentage.[15]

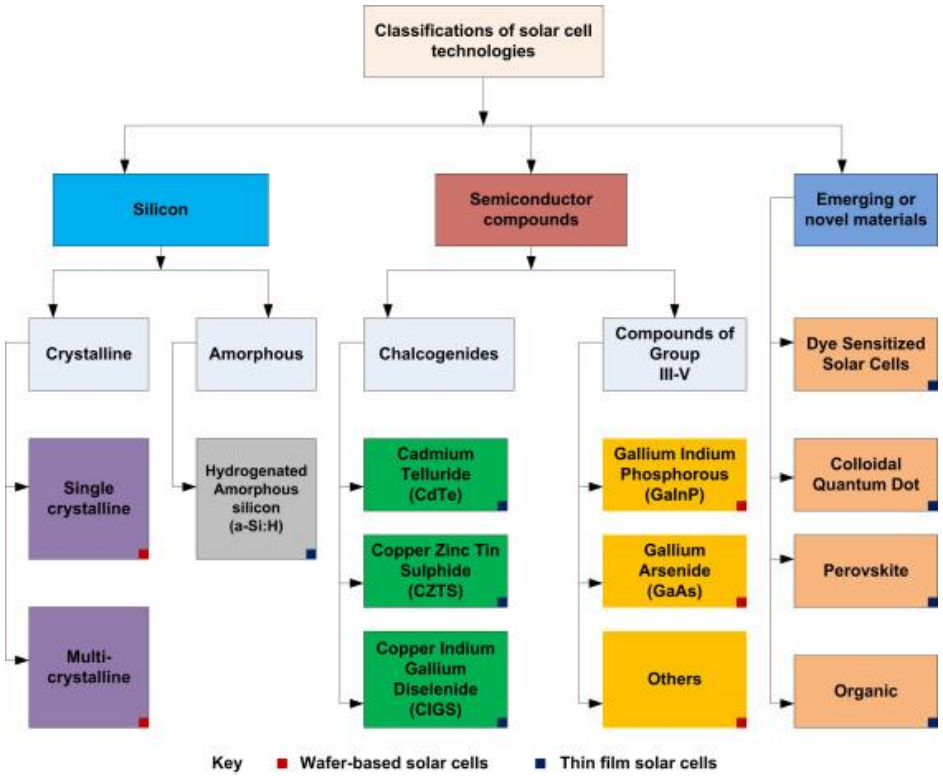

Figure 1.8 Classification of solar cells based on the primary active material.[17]

In principles, the first-generation PVs, which dominates the market share, consist of thick Silicon (Si) films (up to 200μm) that deliver high efficiency but in

exchange of the high cost. The second-generation was developed with scope to lower the fabrication cost by reduction of crystallinity as well as the bulk amount needed for active material compared to the first-generation PVs. This second-generation PVs utilized thin films (few nm to tens of μm) as active material with the challenge of increasing the absorption coefficient to compensate the reduced thickness. Various materials were implemented (e.g. α-Si:H, CIGS, CdTe) which successfully lowered the cost, but the performance was poorer compare to first-generation PVs and thus larger surfaces are needed. As a result, a need was born for increased PV efficiency with inexpensive materials and low production cost (e.g. use of thin films, low-cost fabrication methods) which pushed the development of the third-generation PVs. This class includes various structures (e.g. tandem, stacked multijunction cells) and novel materials, such as dye-sensitized, quantum dot, organic and perovskite solar cells. The development of these materials was based on the significant attention paid, not only on the high optical absorption, but also to the efficient charge collection which would result in an enhanced energy transformation of the solar spectrum.

Among all the emerging materials for photovoltaic application, perovskite solar cells have gain increased attention by the scientific community (Figure 1.9) due to its abrupt growth in efficiency within a few years. Since the first reported dye sensitized perovskite solar cell in 2009 by A. Kojima et. al. the efficiency was increase from 3.81% to over 19% in 2015.[18] Since then, the rate of performance's increment has slowdown with the record announced efficiency as of 2021 to be 25.5% by Ulsan National Institute of Science and Technology (KRICT), while OXFORD PV™ has announced an efficiency of 29.5% for perovskite-Si tandem cell.[19] It is noteworthy that the rate which the perovskite's efficiency growth is the fastest compare to any other PV

technology as it is depicted in the development trend of the different types of PV technologies (Figure 1.10).

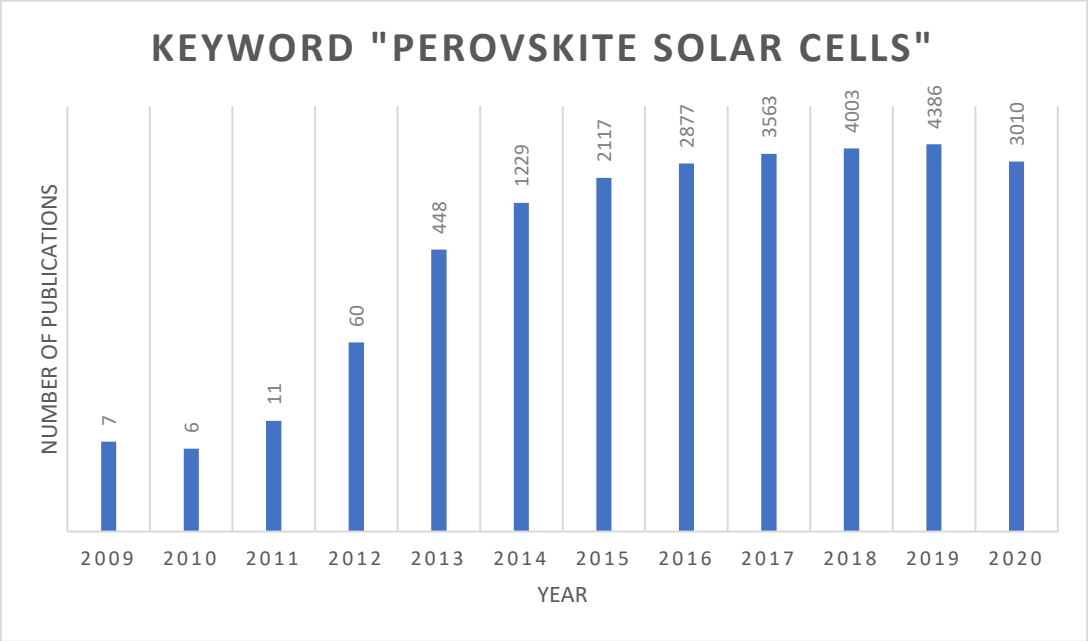

Figure 1.9 Number of publications per year resulting from the search of keyword "perovskite solar cell" in Web of Science™

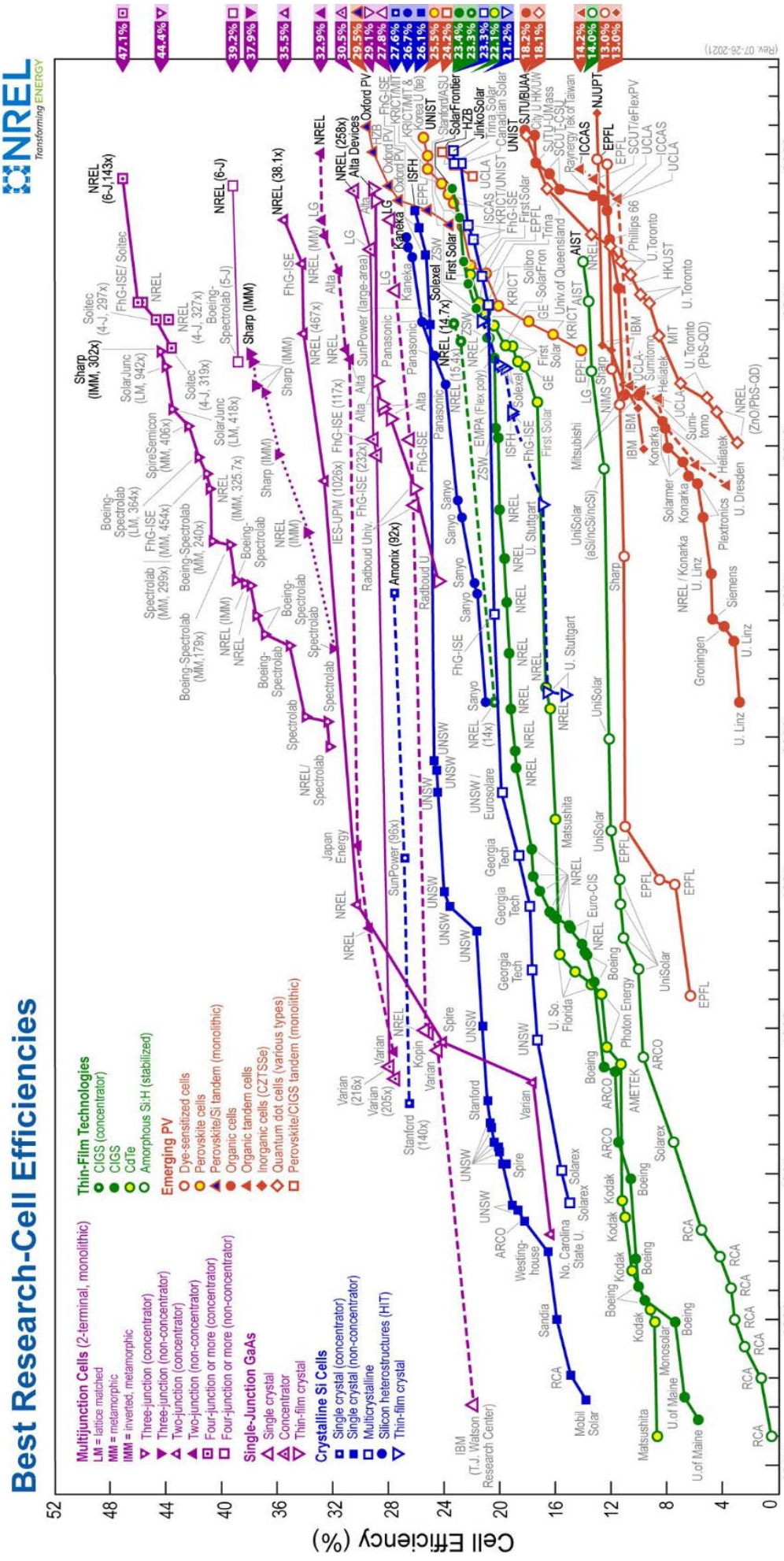

Figure 1.10 Graph recording cell efficiencies over the past three decades of various PV technologies. The values represent lab fabricated devices. Adapted from National Renewable Energy Laboratory (NREL).

1.2 PhD Thesis Outline

The transfer report is organized in the following 7 chapters

- Chapter 1 provides an introduction to solar cells and motivation for this PhD Thesis
- Chapter 2 provides the theoretical background of solar cell's working principles and a literature review about the perovskite's material properties and perovskite solar cells.
- Chapter 3 describes the materials and methods used in this PhD thesis
- Chapter 4 presents and discusses the fabrication and analysis of perovskite solar cells based on solution combustion synthesis of undoped and Cu, Li doped $NiCo_2O_4$ HTL
- Chapter 5 presents and discusses the investigation of solution combustion synthesis conditions of Cu:NiOx films compared to bulk as well as the required synthesis parameters for implementation of Cu:NiOx films as functional HTL in perovskite solar cells
- Chapter 6 presents and discusses the use of Nitrobenzene as additive in methylammonium free (Cs,FA) perovskite active layer for improvement of reliability and humidity degradation resistance of perovskite solar cells applying as HTL the solution combustion synthesized NiOx.
- Chapter 7 presents the conclusion and ideas for future works

2 Theoretical Background and Literature Review

2.1 Chapter Summary

This chapter is divided in two main parts. In the first part a theoretical background for the working principles of solar cells is provided. All the notes as well as the pictures are based on the 3rd chapter of the book Luque A., Hegedus S. (2011) Handbook of Photovoltaic Science and Engineering, Second Edition, John Wiley & Sons, Ltd, the books by Neamen, D. A. (2012) semiconductor physics & devices: basic principles, fourth edition, McGraw-Hill Companies, Inc. and by Kaxiras, E. (2003) Atomic and Electronic Structure of Solids, Cambridge University Press. The structuring of this part starts with an introduction to the basic properties of semiconductors followed by description of p-n junction and finishes with the basic principles of solar cells. In the second part, the material properties of organic-inorganic perovskite that render them ideal absorber for solar cells are introduced. Then, the common device structures are exhibited followed by the presentation of main HTL categories with focus on doped and codoped metal oxides.

2.2 Solar Cells Working Principles

2.2.1 Basic Concepts of Semiconductors

The semiconductors are materials with electrical conductivity ranging between the metals and insulators. Important parameters that affect their electrical characteristics are the physicochemical properties of the component elements (e.g. atoms, molecules) and the degree of periodicity that the elements have been arranged which is called crystallinity. If this periodicity is very high the semiconductors are called monocrystal, if it is limited within groups of a few elements are called amorphous, while if this arrangement is extended over many elements forming multiple regions of monocrystals are called polycrystalline semiconductors. In the latter case these monocrystalline regions are called grains which are separated by the grain boundaries. In principles, the grain boundaries degrade the electrical characteristics and thus monocrystalline semiconductors exhibit superior electrical properties. The way that the atoms interact to form the various structures of semiconductors are called atomic bonds (quantum mechanics theory) and are classified to ionic, covalent, metallic and Van der Walls. Qualitatively, the ionic bond is formed when an atom (or molecule) has an excess electron while another miss one to complete their outer shell (quantum mechanics theory) and thus an electron transfer occurs forming two opposite charged elements that bound. The covalent bond is formed when two atoms (or molecules) donate each one an electron and this pair of electrons is shared by the atoms (or molecules) to complete their outer shells. The metallic bond is formed when loosely

connected electrons to atoms are donated forming an "electron cloud" that holds together the formed ions by electrostatic forces. Finally, the Van der Walls bonds are formed when the effective centers of the positive and negative charge of an element are not centered resulting in weak dipole that can interact with each other. The type of bonds between the elements in crystals depend on the type of elements and the final arrangement (degree of periodicity) of atoms in a structure will be defined when these bonds (interactions) reach a total minimum energy under thermal equilibrium. The periodicity of the elements in a semiconductor defines their electrical properties.

In a perfect periodic crystal, the dynamic description of a moving electron can be established from its wave function (Ψ) which is obtained by solving the time-independent Schrödinger equation:

$$\nabla^2\psi + \frac{2m}{\hbar^2}[E - U(\vec{r})]\psi = 0 \quad (1)$$

where m is the electron mass, ħ is the reduced Planck constant, E is the energy of the electron, and $U(\vec{r})$ is the periodic potential energy inside the semiconductor. The solution of (1) (beyond the scope of this thesis) by making use of a mathematical function by Bloch to describe the periodically varying potential energy:

$$\psi(\chi) = u(x)e^{ikx} \quad (2)$$

where *i* is the imaginary unit and *k* is the wave number are enough to define the energy band structure (the allowed electron energies and the relationship between the electron's energy (E) and momentum ($p = \hbar k$)) of a semiconductor.

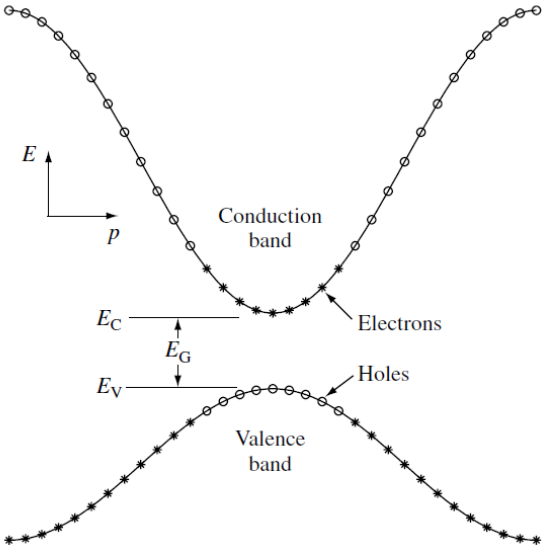

Figure 2.1 A simplified energy band diagram for T>0 for a direct band gap (*E*g) semiconductor.

A simplified description of the energy band structure presumes that in T = 0 K (absolute zero) the valence band are filled by electrons and the conduction band is totally empty. Given that y-axis measures the energy, no allowed energy states exist for the electrons between the valence band maximum (VBM) and conduction band minimum (CBM). These forbidden energies states are called Energy band gap (Eg). In the description above the VBM and CBM are identified at the same point of *p* and in this case the semiconductor is called direct, whereas if the VBM and CBM are not identified at the same *p* the semiconductor is called indirect. The importance of this classification will be revealed later when it will be discussed the electron excitation by photons. Moreover, if the T > 0 K and $kT > Eg$ (Figure 2.1) there is a high probability that electrons (thermally excited electrons) will occupy energy states at the conduction (E_C) band leaving behind empty energy states at the valence band (E_V) which conveniently can be regarded as positively charged carriers of current called *holes.*

As it was states above for T > 0 (but in thermal equilibrium) there is a ratio of electron that have removed from the valence band. Further, the electrons in the solids follow the Pauli Exclusion Principle which states that two or more identical fermions (particles with half-integer spin) cannot occupy simultaneously the same quantum state within a quantum system and thus electrons in crystals obey the Fermi-Dirac distribution function

$$f(E) = \frac{1}{1 + e^{(E-E_F)/kT}} \quad (3)$$

where E_F is the Fermi energy, k is the Boltzmann's constant and T is the Kelvin temperature. As it is clear from (3) the distribution is a strong function of temperature and determines the probability of states with energy (E) (higher than E_F) to be occupied by electrons or, alternatively, the ratio of filled states to available states at each energy. At T = 0 K the electrons are in the lowest possible energy and the equation (3) is a step function (Figure 2.2) where all energies below E_F are filled with electrons. For T > 0 K, thermal excitation will cause some electrons to occupy energies states higher than E_F leaving some states below E_F empty. It is noteworthy, that the Fermi energy determines the statistical distribution of electrons and does not have to correspond to an allowed energy level. For T > 0 K and $E = E_F$ the Fermi-Dirac distribution is ½ which means the probability of a state to be occupies at $E = E_F$ is ½ (The crossing point of all distribution curves at Figure 2.2). Therefore, the Fermi level for T > 0 K (in contrast to Fermi energy for T = 0 K) is considered to be a level, such that at thermodynamic equilibrium would have a 50% probability of being occupied at any given time by electron. It can be argued that the Fermi energy for an intrinsic (undoped) semiconductor (discussed later) is near the middle of the energy band gap.

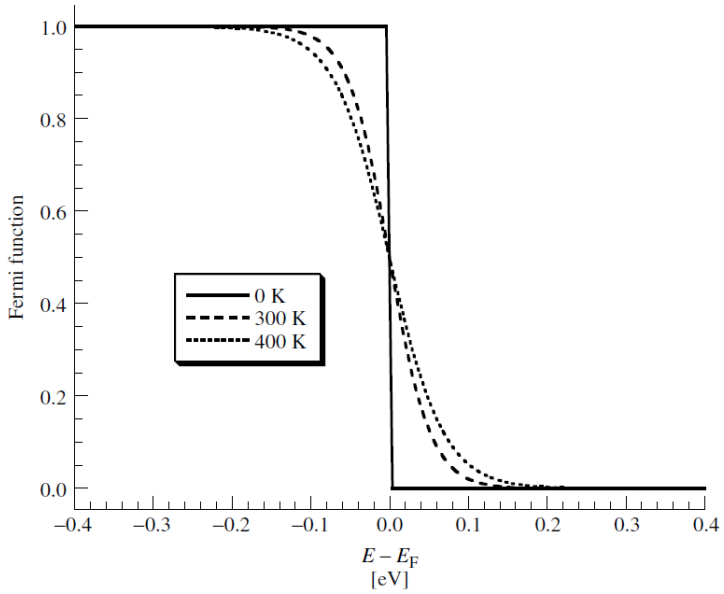

Figure 2.2 The Fermi – Dirac distribution at various temperatures

Further, it can be derived that, if the Boltzmann approximation is valid, the electron (n_o) and hole (p_o) carrier concentrations can be approximated

$$n_o = N_C e^{(E_F - E_C)/kT} \quad (4)$$

and

$$p_o = N_V e^{(E_V - E_F)/kT} \quad (5)$$

where the parameter N_C and N_V are called the effective density of states function in the conduction and valence band, respectively. In this case the semiconductor is said to be nondegenerate and importantly, the product of electron and hole concentrations is independent (in thermal equilibrium) of Fermi energy's location and is calculated by

$$p_0 n_0 = n_i^2 = N_C N_V e^{(E_V - E_C)/kT} = N_C N_V e^{-E_g/kT} \quad (6)$$

In an intrinsic semiconductor in thermal equilibrium the number of holes (p_0) and electron (n_0) are the same ($n_0 = p_0 = n_i$) and using equation (6) it can be computed that

$$n_i = \sqrt{N_C N_V} e^{(E_V - E_C)/2kT} = \sqrt{N_C N_V} e^{-E_g/2kT} \quad (7)$$

which is usually very small making it behave very much like insulators and thus are not very useful as conductor of electricity. By combining equations (4) and (7) the Fermi level in an intrinsic semiconductor ($E_F = E_{F_i}$) is given by

$$E_{F_i} = E_{midgap} + \frac{kT}{2} ln\left(\frac{N_V}{N_C}\right) \quad (8)$$

which is, as it was stated, practically very close to the middle of the band gap $E_{midgap} = \frac{E_V + E_C}{2}$. More precisely, the E_{F_i}will be exactly at the E_{midgap} if the effective density of states in the conduction and valence band are the same ($N_C = N_V$). Whereas it will be slightly above or below E_{midgap} if $N_C < N_V$ or $N_C > N_V$, respectively. Alternatively, it can be shown that the interaction of a moving electron or hole within the periodic potential (band structure effects) of the semiconductor results in the definition of an effective mass (compare to free electron's mass) for electrons (m_n^*) and holes (m_p^*). Using these definitions and the expression (8) the Fermi level in an intrinsic semiconductor can be defined as

$$E_{F_i} = E_{midgap} + \frac{3kT}{4} ln\left(\frac{m_p^*}{m_n^*}\right) \quad (9)$$

so, it can be derived that E_{F_i}will be exactly at the E_{midgap}if the $m_n^* = m_p^*$. Whereas it will be slightly above or below E_{midgap} if $m_n^* < m_p^*$ or $m_n^* > m_p^*$, respectively.

Beyond the description of the structures through the formation of perfect crystals, the periodicity of the atoms is usually interrupted by imperfections or defects. They can be categorized to point, linear, surface and interface defects. Regarding the point defects can be either intrinsic which means the same atoms of the semiconductor have occupy wrong positions or extrinsic which means that different type of atoms has been hosted in the semiconductor. Depending on their density in the crystal structure these defects may interact with each other in case of high density (spatial proximity). Among these the most common are the intrinsic vacancies, interstitial defect and the extrinsic substitutional defects.

Figure 2.3 represents a two-dimensional crystal lattice (a geometrical representation of a crystal). The 'V' symbol corresponds to a site of a missing atom which is quite common in many crystals. Interstitials symbolled with 'I' corresponds to an extra atom which has occupy a site that does not coincide with regular crystalline sites, and they are common in crystal structures without dense packing of their atoms. In both cases, since the symmetry has been interrupted and there is a number of broken bonds (dangling bonds) the electronic states of the semiconductor may be affected. If these intrinsic defects have energies in the same range of the perfect crystal, then the impact on energy states are marginal, but if the energies are different (e.g. in the range of Eg) then new energy states may be introduced in the Eg.

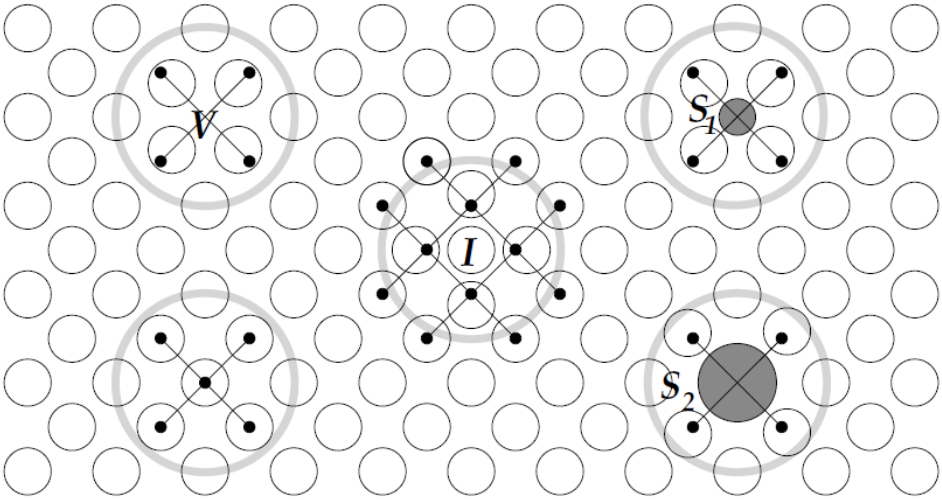

Figure 2.3 Illustration of point defects in a two-dimensional square lattice. V = vacancy, I = interstitial, S1, S2 = substitutional impurities of size smaller and larger than the host atoms, respectively.

For example, a vacancy point defect where four dangling bonds have been formed and the energies are in the range of Eg (left sketch of Figure 2.4) then the four electrons are combined in pairs to form two new bonding and two new antibonding states by distorting the neighbor atoms. Since each bond can accommodate two electrons with different spin then the four electrons occupy the lowest energies (bonding states) leaving the two antibodies states empty (right sketch of Figure 2.4) while as it was stated earlier this process does not induce a change in the Fermi level (E_F). This physical mechanism is called Jahn–Teller distortion and it is common in defect configurations when the undistorted defect structure corresponds to partially occupied, degenerate electronic states

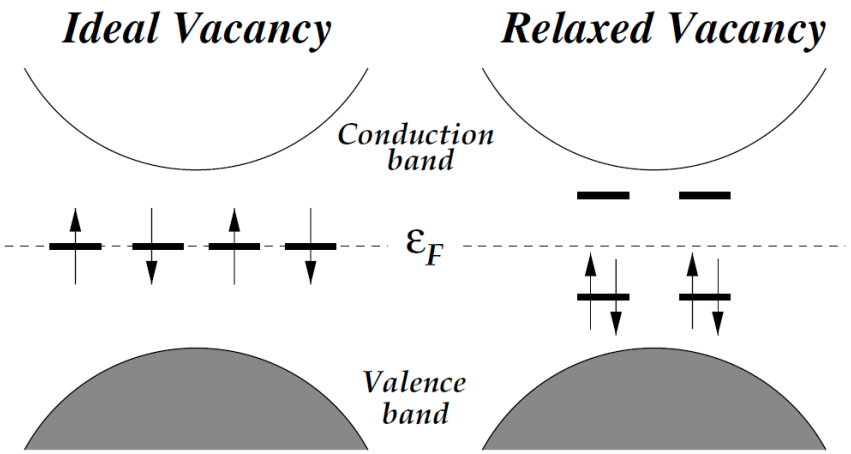

Figure 2.4 Schematic representation of new electronic states formation by vacancy point defect.

As regards the extrinsic point defect of substitution (Figure 2.3 marked as S1 and S2 for different size of substitutional atoms) show high scientific interest due to ability it offers to tune the opto-electronic properties of the semiconductors. A very important application of the substitutional defect is the controllable addition of doping (impurity) atoms in the crystal structure of the semiconductors. Usually, the substitutional energies are different than the host atoms and if the atom has the same size, then a stable structure is formed and in some cases the atom behaves like isolated atom in an external film. This field cause the split of energy levels of the atom which would be degenerated (multiple states with same measurable energy) in case of the free atom. Qualitatively, for example if a group V element (five valence electrons) is introduced in a host material that composed of group IV element then four electrons will contribute to the covalent bonding and the fifth electron will remain loosely bounded to the atom and this electron is called donor electron. Intuitively, this electron requires much less energy to excited (Figure 2.5) from its current state (donor state

(E_D)) in the Eg to conduction band compared to those contributed to covalent bonding. When the electron is excited to conduction band (ionized) it adds an electron without the creation of a hole in the valence band, leavening "behind" a charged ion which is called ionized donor impurity atom (N_D^+). This type of semiconductor is called n-type where n stands for negative, and the electrons called majority charge carrier while the holes minority charge carries. If the same consideration is done but for a group III atom in group IV host material, then an energy state (acceptor state (E_A)) in Eg close to valence band will be created which can easy generate holes in the valence band without the creation of electron in the conduction band "leaving" behind again a charge ion and this atom is called ionized acceptor impurity atom (N_A^-). This semiconductor is called p-type where p stands for positive, and the holes called majority charge carrier while the electrons minority charge carries. The number of ionized donors (N_D^+) for N_D added donor impurity atom and of ionized acceptors (N_A^-) for N_A impurity atom are given, respectively, by

$$N_D^+ = \frac{N_D}{1 + g_D e^{(E_F - E_D)/kT}} = \frac{N_D}{1 + e^{(E_F - E_D')/kT}} \quad (10)$$

and

$$N_A^- = \frac{N_A}{1 + g_A e^{(E_A - E_F)/kT}} = \frac{N_A}{1 + e^{(E_A' - E_F)/kT}} \quad (11)$$

where g_D and $g_A$are the donor and acceptor site degeneracy factors. Typically, $g_D = 2$ and $g_A = 4$. These factors are normally combined into the donor and the acceptor energies so that $E_D' = E_D - kTlng_D$ and $E_A' = E_A - kTlng_A$.

In principles, the energy states introduced by the impurities, which are relevant to doping, lies within the band gap of the semiconductor. If the energy of the impurity-related states is near the middle of the band gap they are called “deep” states; Also called trap states because the thermal excitation is very slow and the site acts as a scavenger for mobile carriers in the band. If they are identified near the CBM (or VBM) they are called “shallow” states which are more useful impurity types because they can be ionized even in room temperature giving rise to a delocalized band states (of electrons at CB and holes at VB) that can carry current. One more aspect of the added charges related to the impurities is their effective mass (m*) due to band structure effect and if the effective mass is smaller or larger than the electron mass they are described as “light” or “heavy” electrons or holes. In very rough approximation the more curved the curvature of E versus K (band structure) near the CBM and VBM the lighter the electrons and the holes in the respective bands.

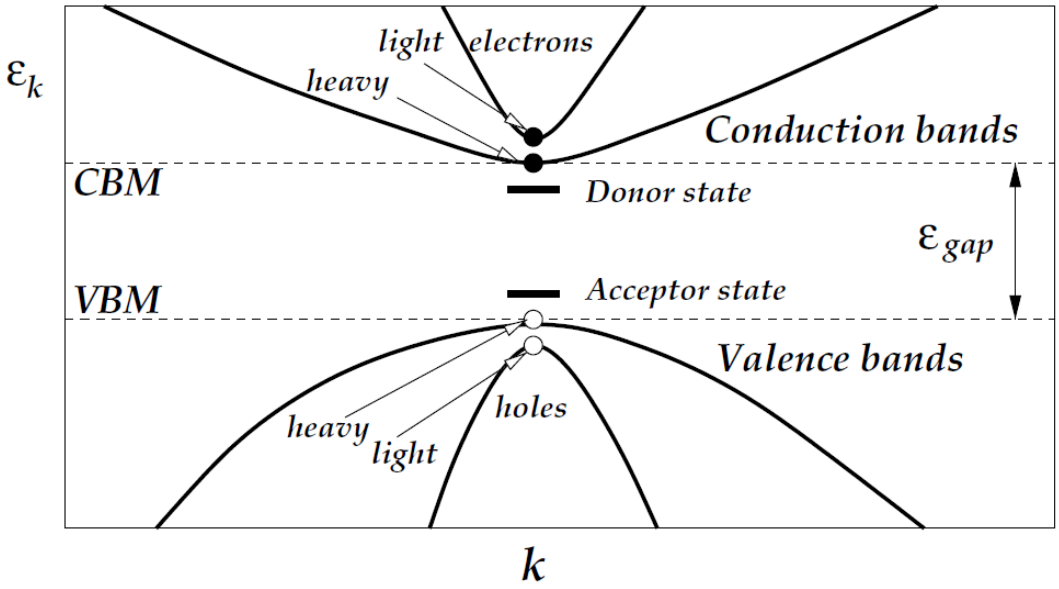

Figure 2.5 Schematic illustration of shallow donor and acceptor impurity states in a semiconductor with direct gap. The light and heavy electron and hole states are also indicated; the bands corresponding to the light and heavy masses are split in energy for clarity.

As it was shown above the extrinsic doping adds electrons (holes) without the creation of holes (electrons). Consequently, in an n-type (p-type) semiconductor the $n_o > p_o$ ($p_o > n_o$). Since equation (4) and (5) are general equations in terms of Fermi level for the semiconductors, by adding and subtracting an intrinsic Fermi energy (E_{F_i}) in the exponent of equation (4) we get

$$n_o = N_C e^{\left[-\left(E_C - E_{F_i}\right) + \left(E_F - E_{F_i}\right)\right]/kT} \quad (12)$$

or

$$n_o = N_C e^{\left[-\left(E_C - E_{F_i}\right)/kT\right]} e^{\left[\left(E_F - E_{F_i}\right)/kT\right]} \quad (13)$$

Furthermore, in the case of intrinsic semiconductor the carrier concentration (n_i) can be given in another form by equation (4) in terms of intrinsic fermi energy (in contrary to equation (7)) using $E_F = E_{F_i}$

$$n_i = N_C e^{\left(E_{F_i} - E_C\right)/kT} \quad (14)$$

thus, by substituting equations (14) to (13) we derive the formula of the electron concentration (n_o) for a n-type semiconductor

$$n_o = n_i e^{\left(E_F - E_{F_i}\right)/kT} \quad (15)$$

Making the same considerations we derive the formula of the hole concentration (p_o) for a p-type semiconductor

$$p_o = n_i e^{-\left(E_F - E_{F_i}\right)/kT} \quad (16)$$

In equation (10) and (11) the number of ionized donors and acceptors were given, but often the donor and acceptor atoms are assumed to be completely ionized so that $n_0 \cong N_D$ in n-type material and $p_0 \cong N_A$in p-type material. By making this assumption and use of equations (15) an expression for the Fermi level for n-type is derived

$$E_F - E_{F_i} = kTln\frac{N_D}{n_i} \quad (17)$$

while using equation (16) the expression for p-type is

$$E_F - E_{F_i} = -kTln\frac{N_A}{n_i} \quad (18)$$

noticing that no compensation effect was considered since it is beyond the scope of this thesis. It can be noted from equation (17) that, for a n-type semiconductor, as the number of donor atoms (N_D) in host material are increased the Fermi level (E_F) is shifted from intrinsic Fermi level (E_{F_i}) toward the conduction band (E_C).Whereas from equation (18) for a p-type semiconductor, as the number of acceptor atoms (N_A) in host material are increased the Fermi level (E_F) is shifted from intrinsic Fermi level (E_{F_i}) toward the valence band (E_V). This physical mechanism is illustrated in Figure 2.6.

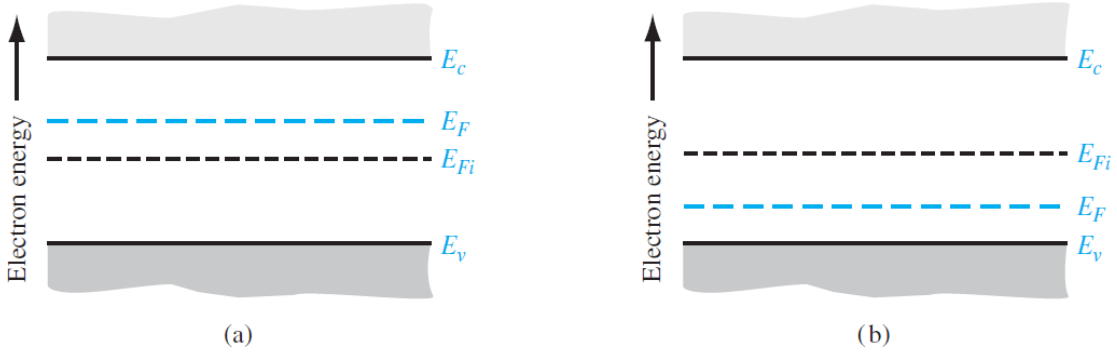

Figure 2.6 Position of Fermi level for an (a) n-type and (b) p-type semiconductor.

It should be added that the description above was made for low concentrations of dopant atoms. Otherwise, if the concentration is too high (heavily doped semiconductors) the perturbation to the host atoms system is high which may induce a narrowing of the E_g, or even the interactions of the impurities which may shift the Fermi levels (E_F) beyond E_C or E_V producing degenerated n-type or p-type semiconductors. Heavily doped regions may be identified near the regions of metal-semiconductor contacts.

2.2.2 Charge Carrier Transport

The basic charge carrier movement (called transport) in a semiconductor can be described in two terms, the movement due to an electric field which is called drift and the movement due to density gradient which is called diffusion. These processes are derived by classical approximations since the electrical charges are considered free particles with effective masses m_n^*, m_p^*. The net flow of electrons (conduction band) and holes (valence band) generates the electrical current.

Regarding the drift current density (J_{drf}) it is generally descripted by

$$J_{drf} = \rho v_d \quad (19)$$

where ρ is a positive volume charge density and v_d an average drift velocity. By replacing the ρ in (19) with the positively charged holes we get

$$J_{p|drf} = (ep)v_{dp} \quad (20)$$

which describes the drift current density due to holes, where v_{dp} the average drift velocity of the holes.

Since the electrical charges were considered free particles with effective masses of m_p^* , m_e^* the motion equations in a constant electric field can be described classically by

$$F = m_{cp}^* \alpha = eE \quad (21)$$

Where $m_{cp}^*$is the conductivity effective mass of the hole in valence band (the effective mass for carriers in motion) and α, e and E the acceleration, electrical charge and the electric field, respectively. The same consideration holds for the electrons in the conduction band. In a free particle without any impedance on their motion the charges would accelerate without any bound and the velocity would scale linearly with the time. However, collisions with thermally vibrating crystal's atoms, crystal defects, impurity atoms and even inter-collisions of the charge carrier alter their movement behavior called scattering. This movement is better described by phases of acceleration and collisions resulting in the loss of most, or even all, of the energy which is repeated over and over again. In a macroscopic scale the particles will gain a net average drift velocity which is, for low electric fields, proportional to the electric field and it can be written as

$$v_{dp} = \mu_p E \quad (22)$$

where μ_p is a proportionality factor called hole mobility. It is an important parameter of a semiconductor describing how "quickly" a hole moves in the semiconductor under a low electrical field. Combining equations (21) and (22) it may be expressed the hole drift current density as

$$J_{p|drf} = e\mu_p pE \quad (23)$$

which has the same direction as the applied electrical field. Following the same consideration, the drift current density due to electrons can be expressed as

$$J_{p|drf} = e\mu_n nE \quad (24)$$

where μ_n is the electron mobility and has the same direction with the electric field. Thus, the total drift current density can be given by combining drift current density due to holes (23) and electrons (24)

$$J_{drf} = e\big(\mu_n n + \mu_p p\big)E \quad (25)$$

It can be shown that, alternatively, the charge carrier mobility can be expressed as

$$\mu_p = \frac{e\tau_{cp}}{m^*_{cp}} \quad (26)$$

for holes and for electrons as

$$\mu_n = \frac{e\tau_{cn}}{m^*_{cn}} \quad (27)$$

where m^*_{cp} and m^*_{cn} is the conductivity effective mass of the hole and electron, respectively, which is assumed to be constant. The τ_{cp} and τ_{cn} denotes the mean time between two collisions. There are two significant scattering mechanism that affect the mobility in a semiconductor. First, the lattice (phonon) scattering due to thermal movement of atoms around their lattice position in a crystal and if we denote the mobility ascribed only to first mechanics as μ_L then we can get from scattering theory the expression

$$\mu_L \approx T^{-n} \quad (28)$$

which means that the mobility will increase by decreasing the temperature.

The second scattering mechanism is due to electrostatic (coulomb) interactions between the charged carriers and the ionized impurity atoms called the ionized impurity scattering. If we denote the mobility ascribed only to first mechanics as μ_I then we can get to first order the expression

$$\mu_I \approx \frac{T^{3/2}}{N_I} \quad (29)$$

where $N_I = N_D^+ + N_A^-$ is the total number of the ionized atoms in the semiconductor. The equation (28) suggests that by increasing the temperature the mobility will increase due to less "time" spent in the vicinity of the ionized impurities, whereas the mobility will be decreased as the number of ionized atoms increases due higher probability to encounter an impurity atom. If we denote as $\tau_L$the mean time of two scattering event ascribed only to lattice (phonon) scattering and $\tau_I$only to ionized impurity scattering and assume that the processes are independent, then the sum of the scattering events within a differential time *dt* can be given as

$$\frac{dt}{\tau} = \frac{dt}{\tau_I} + \frac{dt}{\tau_L} \quad (30)$$

Taking in account the equations (26), (27) and (30) we can express the net mobility μ as

$$\frac{1}{\mu} = \frac{1}{\mu_I} + \frac{1}{\mu_L} \quad (31)$$

which means that the net mobility for the various added scattering mechanics decreases.

Given the charge mobility description and rewriting the drift current density the conductivity (σ) in a semiconductor can be expresses as

$$J_{drf} = e(\mu_n n + \mu_p p)E = \sigma E \quad (32)$$

which is a function of the electrons and hole concentration and their respective mobilities. As it was shown the mobility and charge concentration depends on the impurities concentration, so it is derived that conductivity for a given temperature is a complicate function of impurities concentration, rather than a linear function of impurity concentration. Moreover, the resistivity can be defined as the reciprocal of the conductivity

$$\rho = \frac{1}{\sigma} = \frac{1}{e(\mu_n n + \mu_p p)} \quad (33)$$

and can be easily shown that for a bar semiconductor (Figure 2.7) under applied voltage (V) the Ohm's law

$$V = RI = \left(\frac{\rho L}{A}\right) I \quad (34)$$

states that the resistance (*R*) is a function of resistivity and semiconductors' geometry, where L and A are the length and the cross-section area of the bar.

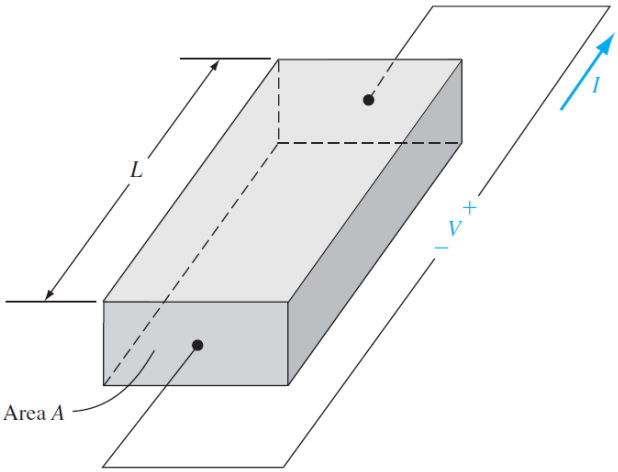

Figure 2.7 Bar of semiconductor material as a resistor

In case of p-type (a similar to following consideration is also valid for n-type) semiconductor with an acceptor impurity concentration N_A and $N_D = 0$, where $N_A \gg n_i$ and assuming that the hole and electron mobilities are at the same order of magnitude $(\mu_n \cong \mu_p)$ then the conductivity can be expressed as

$$\sigma = e(\mu_n n + \mu_p p) \cong e\mu_p p \quad (35)$$

In case of full ionization of impurities atoms ($N_A = N_A^- \cong p$) it is derived from (35) that

$$\sigma \cong e\mu_p N_A \cong \frac{1}{\rho} \quad (36)$$

stating that the conductivity (resistivity) in an extrinsic semiconductor is mainly a function of majority charge carrier properties.

As it was stated the charge carriers also tent to move from regions of high concentration toward a region of low concentration (called diffusion) due to random thermal movement inducing a tendency to distribute evenly. The net flow of the

electrical charges would result in a diffusion current, and its density can be derived for one spatial dimension (*x*) and assuming uniform temperature

$$J_{nx|dif} = eD_n \frac{dn}{dx} \quad (37)$$

for the electrons

$$J_{px|dif} = -eD_p \frac{dp}{dx} \quad (38)$$

and for the holes. The parameters D_n and D_p are called electron and hole diffusion coefficient, respectively, and indicates how well the charge carriers move due to their density gradient.

The total current density in a semiconductor is the sum of electrons' and holes' drift and diffusion currents densities and thus using equations (23), (24), (37) and (38) generalized to three dimensions it is derived for the hole current densities

$$\overrightarrow{J_p} = qp\mu_p\vec{E} - qD_p\nabla p \quad (39)$$

and for electron current densities

$$\overrightarrow{J_n} = qp\mu_n\vec{E} + qD_n\nabla n \quad (40)$$

while the total current density is

$$\vec{J} = qn\mu_n\vec{E} + qp\mu_p\vec{E} + qD_n\nabla n - qD_p\nabla p \quad (41)$$

So far, the semiconductors were assumed to be uniformly doped but there are special cases where the semiconductor is nonuniformly doped. For instance, Figure 2.8 illustrates a qualitative sketch of the energy band as a function of one-spatial dimension

(*x*) for n-type nonuniformly doped semiconductor. Given that the semiconductor is in thermal equilibrium the Fermi energy will be constant throughout the semiconductor. For this case the doping concentration decreases for increasing x and thus electrons (majority charge carriers) will diffusion from high concentration region toward low concentration region (+*x* direction) leaving behind positively charged donors.

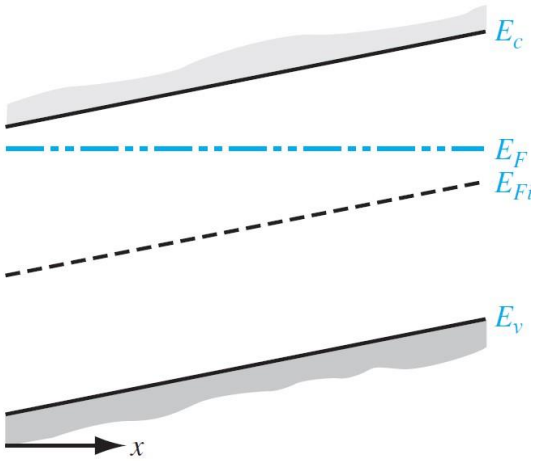

Figure 2.8 Energy-band diagram for a semiconductor in thermal equilibrium with a nonuniform donor impurity concentration.

This will induce an electric field which opposes the diffusion direction and when equilibrium is reached the remaining charged impurities is different from the charge carrier concentration. The electron potential energy of charge (-*e*) can be correlated to electric potential Φ through function

$$\Phi = \frac{1}{e}\left(E_F - E_{F_i}\right) \quad (42)$$

while the electric field (*E*) in one dimension (*x*) is defined as

$$E_x = -\frac{d\Phi}{dx} \quad (43)$$

Combining equations (42) and (43) and given that the Fermi level is constant throughout semiconductor in thermal equilibrium ($\frac{dE_F}{dx} = 0$) it is derived that

$$E_x = \frac{1}{e}\frac{dE_{F_i}}{dx} \quad (44)$$

meaning that the change of intrinsic Fermi level throughout a semiconductor under thermal equilibrium suggests the existence of an electric field in it. Thus, it can be shown that if we assume a quasi-neutrality condition ($n \cong N_D \; or \; p \cong N_A$) and a nonuniform spatial (x) doping profile in a n-type ($N_D(x)$) or p-type ($N_A(x)$) semiconductor an electric field exist in it which can be calculated by

$$E_x = -\left(\frac{kT}{e}\right)\frac{1}{N_D}\frac{dN_D(x)}{dx} \quad (45)$$

Furthermore, combining equation (41) (for one dimension (x)) and (45) and assuming that there is no electrical connection and thus is in thermal equilibrium (drift and diffusion currents are exactly balanced) it can be derived the Einstein relation for nondegenerate semiconductor

$$\frac{D_n}{\mu_n} = \frac{D_p}{\mu_p} = \frac{kT}{e} \quad (46)$$

suggesting that diffusion coefficient and mobility are related to each other.

2.2.3 Light Absorption

The electromagnetic radiation is descripted in quantum theory by a zero-mass quantum particle (wave-particle duality) called photon carrying energy (E_{ph}) and momentum (p_{ph}) that depends only on its frequency (f):

$$E_{ph} = hf \quad (47)$$

$$p_{ph} = \frac{hf}{c} \quad (48)$$

where h is plank constant and c the speed of light. The wavelength (λ) of the photon can also be related to its energy using equation (47)

$$\lambda = \frac{c}{f} = \frac{hc}{E_{ph}} = \frac{1.24}{E_{ph}}\ \mu m \quad (49)$$

While various mechanics of interaction of the photon with a semiconductor exist, in the simplest case, the photons will be absorbed by a semiconductor which may result in the generation of an electron - hole pair called fundamental absorption. This process must conserve both total energy and momentum, but since the photon momentum (48) is orders of magnitude lower than the lattice momentum practically the electron momentum is conserved. Thus, assuming that no energy states exist in the band gap (E_g), if the initial state of an electron in the valence band is E_1 while the final state is E_2 and the photon's energy is $E_{ph} = hf = E_2 - E_1$ (Figure 2.9) it is defined that the absorption coefficient (a) for a given energy is proportional to the probability (P_{12}) of this transition, the electron's density of states of the initial state $g_V(E_1)$ and the density of available final states $g_C(E_2)$ and summed over all possible transition between these states.

$$a(hf) \approx \sum P_{12} g_V(E_1)\, g_C(E_2) \quad (50)$$

It can be shown that if the initial intensity of a photon flux denoted as $I_{(0)}$ then the intensity reduction while it travels (x+dx) through a semiconductor can be expressed with the use of the absorption coefficient as

$$I_{(x)} = I_{(0)}e^{-ax} \quad (51)$$

The absorption coefficient α (units cm^{-1}) is the relative number of photons absorbed per unit distance and if α is large it means that the photons are absorbed over a relatively short distance.

For a direct band gap semiconductor (VBM and CBM are identified at the same crystal momentum (p)) where, as it was stated, the initial electron state energy is E_1 and the crystal momentum p_1 while the final electron energy state is E_2 and the crystal momentum p_2, and assuming that momentum is conserved ($p_1 \cong p_2 = p$) then for a an absorbed photon with energy $E_{ph} \geq E_g$ in order to be conserved the total energy we have

$$E_{ph} = hf = E_2 - E_1 \quad (52)$$

resulting in the generation of an electron - hole pair. If photon's energy is less than the fundamental band gap (E_g) and no interband states exist then no absorption occurs, while if photon's energy is larger than E_g an electron - hole pair is generating and the

excess energy may be given as additional kinetic energy which will be dissipated as heat in the semiconductor.

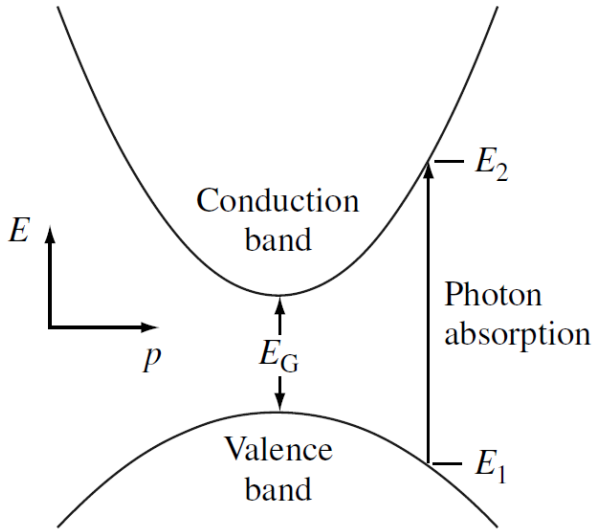

Figure 2.9 Photon absorption in a direct band gap semiconductor for an incident photon with energy E_{ph}= hf = $E_2 - E_1 > E_G$

It can also be proven that if it supposed that bands are parabolic for a direct band gap semiconductor with allowed direct transitions ($p = 0$) the absorption coefficient is proportional to

$$a(hf) \approx A\left(hf - E_g\right)^{1/2} \quad (53)$$

where A is a constant.

If the valence band maximum (VBM) and conduction band minimum (CBM) are not identified at the same p the semiconductor is called indirect. In this process to be fulfilled the conservation of the electron momentum it is necessary that the photon absorption process involve an additional particle called phonon. The phonons are quasi-particles that represent the lattice's variations of a semiconductor and are characterized by lower energy but relative high momentum. The process of electron excitation by

light in an indirect semiconductor retains energy and momentum conservation by the absorption of a photon as well as the absorption or emission of a phonon as it is depicted in Figure 2.10. In principles, indirect semiconductor exhibits low absorption coefficients α since two physical mechanisms are involved in the process of light absorption.

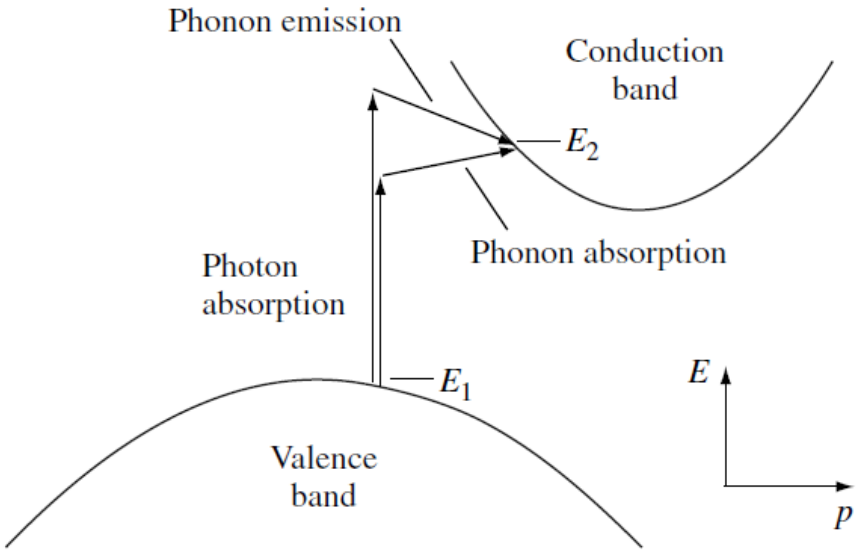

Figure 2.10 Photon absorption in an indirect band gap semiconductor for a photon with energy $E_{ph} = hf = < E_2 - E_1$ and a photon with energy $E_{ph} = hf = > E_2 - E_1$. Energy and momentum in each case are conserved by the absorption and emission of a phonon, respectively

2.2.4 Excess Carrier Generation and Recombination

As it was discussed in the previous section the absorption of a photon may result in the formation of an electron-hole pair. Except the above physical mechanism other absorption processes in a direct semiconductor may be involved such as absorption

aided by localized states in the band gap, absorption in the presence of an electric field e.t.c. The net absorption coefficient due to all possible processes (i) is summed over

$$\alpha(hf) = \sum_i a_i(hf) \quad (54)$$

The complexity of absorption processes imposes the use of measured or empirical defined absorption coefficient for analysis and modeling. The rate of electron-hole pair generation $G_{(x)}$ as a function of position (x) due to absorption over a defined wavelength (λ) spectrum of photon energies is expressed as

$$G_{(x)} = (1-s)\int_\lambda \left(1 - r_{(\lambda)}\right) f_{(\lambda)} \alpha_{(\lambda)} e^{-\alpha x} d\lambda \quad (55)$$

where s is the grid-shadowing factor, $r_{(\lambda)}$ is the reflectance, $\alpha_{(\lambda)}$ is the absorption coefficient, $f_{(\lambda)}$ is the incident photon flux (number of photons incident per unit area per second per wavelength), where the sunlight is assumed to be incident at $x = 0$.

When a semiconductor is illuminated by light is taken out of the thermal equilibrium due to photon absorption, which creates additional electron ($n = n_o + \delta n$) -hole ($p = p_o + \delta p$) pairs changing their thermal equilibrium concentrations. The semiconductor tends to relax back to thermal equilibrium through elimination of the excess charge carriers ($\delta n, \delta p$) by recombination of electron-hole pairs. Various recombination mechanisms are possible in a semiconductor which can be classified to trap assisted recombination through the involvement of an interband energy state (trap), to radiative recombination (band-to-band) and Auger recombination (Figure 2.11).

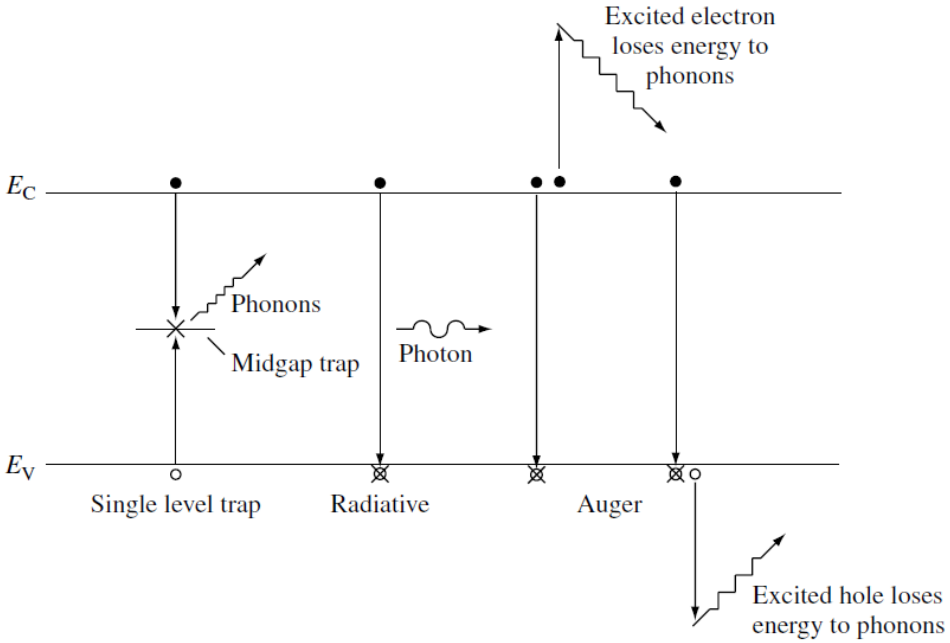

Figure 2.11 Recombination processes in semiconductors

A trap allocated at energy E_t in the band gap can assist the electron-hole recombination (referred as Shockley–Read–Hall(R_{SRH})) where the rate per unit volume per second that this process occurs it can be shown that is

$$R_{SRH} = \frac{pn - n_i^2}{\tau_{SRH,n}\left(p + n_i e^{\left(E_{F_i} - E_t\right)/kT}\right) + \tau_{SRH,p}\left(n + n_i e^{\left(E_t - E_{F_i}\right)/kT}\right)} \quad (56)$$

In (54) τ_{SRH} is the carrier lifetime which is given by

$$\tau_{SRH} = \frac{1}{\sigma v_{th} N_T} \quad (57)$$

where σ is the capture cross section, v_{th} is the thermal velocity of the charge carriers, and N_T is the trap concentration. Regarding the trap concentration it can be seen that high spatial concentration of defects reduces the lifetime of carriers inducing high recombination rate. Moreover, if the velocity of a carrier v_{th} is high then the probability to encounter a trap within a time span is increased and if the presented size of the trap

(capture cross section) is large for this velocity then again, the lifetime is reduced increasing the recombination rate. Assuming, for example, a p-type semiconductor ($p \cong p_o \gg n_o$), in low injection ($n \ll p_o$), and trap energy near the middle of the energy gap ($E_t \cong E_{F_i}$) equation (56) can be simplified to

$$R_{SRH} \cong \frac{n - n_o}{\tau_{SRH,n}} \quad (58)$$

while similar assumption can be made for a n-type semiconductor which gives

$$R_{SRH} \cong \frac{p - p_o}{\tau_{SRH,p}} \quad (59)$$

where in both cases the recombination rate depends only on minority carrier properties. It can be shown that the carrier lifetime is minimized when the trap level is at or close to the mid-gap energy ($E_T - E_{F_i} = 0$). This implies that deep level defects (close to the middle of the gap) are effective recombination centers.

Radiative (band-to-band) recombination is the inverse process of the optical generation, and when this occurs the energy difference between the two states $E_2 - E_1$ is transmitted in the form of electromagnetic radiation (photon). This recombination process is much more efficient in direct semiconductors, while in the case of indirect semiconductors part of this energy is shared with a phonon. The net recombination rate (R_λ) of the band-to-band recombination is given by

$$R_\lambda = B(pn - n_i^2) \quad (60)$$

where *B* is a constant called bimolecular recombination coefficient. Assuming again a p-type semiconductor ($p \cong p_o \gg n_o$), in low injection ($n \ll p_o$) the net radiative recombination can be expressed

$$R_\lambda \cong \frac{n - n_o}{\tau_{\lambda,n}} \quad (61)$$

In (61) $\tau_{\lambda,n}$ is the carrier lifetime which is given by

$$\tau_{\lambda,n} = \frac{1}{p_o B} \quad (62)$$

while a similar expression can be given for a n-type semiconductor.

The Auger recombination is non-radiative process where three particles are involved. First a radiative recombination produces a photon which then is absorbed by an electron in the CB (or hole in VB). This surplus of energy is given off as kinetic energy to the electron (or hole) which then relax back to CBM (or VBM) releasing this excess energy and momentum to photons (dissipated as heat). The process mostly occurs for high excitation intensities and thus at lower carrier concentrations can be neglected. The recombination rate can be expressed as

$$R_{Auger} = \left(\Lambda_n n - \Lambda_p p\right)(pn - n_i^2) \quad (63)$$

All the above-mentioned recombination processes occur in parallel and so the total rate can be expressed as the sum of each process

$$R = \left[\sum_{traps\ i} R_{SRH,i}\right] + R_\lambda + R_{Auger} \quad (64)$$

where the *i*-summation index corresponds to the distribution of the traps in the band gap. Applying again the low-level injection assumption in a doped material (p or n type semiconductor) an effective minority-carrier lifetime (τ_{eff}) can be given by

$$\frac{1}{\tau_{eff}} = \left[\sum_{traps\ i} \frac{1}{\tau_{SRH,i}}\right] + \frac{1}{\tau_{\lambda}} + \frac{1}{\tau_{Auger}} \quad (65)$$

The discussion, so far, about the recombination processes were focused on bulk materials where almost single crystals (a high periodicity of atoms) were assumed. In real semiconductors the perfect crystallinity is abruptly terminated at the surfaces (interfaces) and thus the periodic potential is disrupted inducing a high concentration of defects which in turn creates a high concentration of discrete energy states (traps) in the band gap (Figure 2.12).

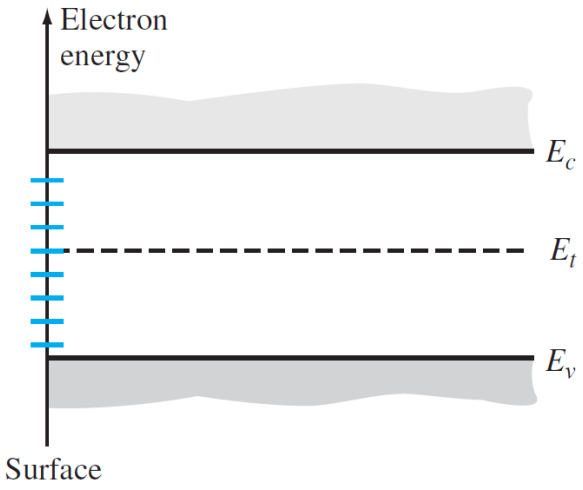

Figure 2.12 Distribution of surface states within the forbidden bandgap

A general expression for the surface recombination is

$$R_s = \int_{E_V}^{E_C} \frac{pn - n_i^2}{\left(p + n_i e^{\left(E_{F_i} - E_T\right)/kT}\right)/s_n + \left(n + n_i e^{\left(E_T - E_{F_i}\right)/kT}\right)/s_p} D_{\Pi}(E_T) dE_T \quad (66)$$

where E_T is the trap energy, $D_{\Pi}(E_T)$ is the surface state concentration as a function of the state's energy, and s_n,s_p are the surface recombination velocities. A simplification can be made if we use the Shockley–Read–Hall theory where, as it was shown in (57), the minority carrier's lifetime is inverse proportional to the trap concentration. Given that the density of the trap states at the surface are larger compared to the bulk material then the excess minority carrier's ($\delta p = p - p_o$, $\delta n = n - n_o$) lifetime at the surface will be smaller than in the bulk. Considering an n-type semiconductor then a similar expression to (59) for the recombination rate of excess carriers at the surface can be given

$$R_s \cong \frac{p - p_o}{\tau_{s,p}} = \frac{\delta p_s}{\tau_{s,p}} \quad (67)$$

where δp_s is the excess minority carrier hole concentration at the surface and $\tau_{s,p}$ is the excess minority carrier hole lifetime at the surface. Additionally, we define the excess minority carrier hole concentration in the bulk from the expression (59) as $\delta p_B = p - p_o$ with carrier lifetime $\tau_{SRH,p}$. Further, we assume a semiconductor where the excess carriers are generating at a constant rate (steady-state conditions) throughout the material (x) and that the recombination rate are equal for the excess carries at the surface (R_s) and in the bulk material (R_{SRH}). Since the excess minority carrier lifetime at the surface is smaller than in the bulk ($\tau_{s,p} < \tau_{SRH,p}$) then it deduced that the excess minority carrier concentration at the surface is smaller than the excess minority carrier concentration in the bulk ($\delta p_s < \delta p_B$). In Figure 2.13 is illustrated the carrier

concentration as function of distance (surface set at $x = 0$) in a semiconductor under steady-state generation and recombination conditions, where it is highlighted that the excess minority carrier concentration is lower at a surface (interface) (δp_s) compared to bulk region (δp_B).

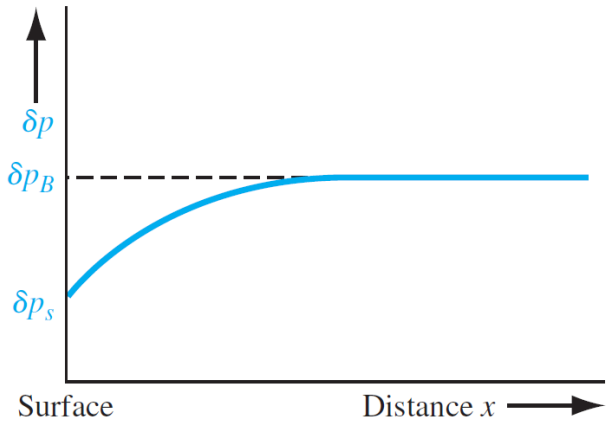

Figure 2.13 Steady-state excess hole concentration versus distance from a semiconductor surface

After defining the generation (G) and recombination (R) rate of the excess carriers in semiconductor, it can be shown that the hole and electron continuity equations generalized in three dimensions for hole and electrons are

$$\nabla \cdot \overrightarrow{J_p} = q\left(G - R_p - \frac{\partial p}{\partial t}\right) \quad (68)$$

$$\nabla \cdot \overrightarrow{J_n} = q\left(R_n - G - \frac{\partial n}{\partial t}\right) \quad (69)$$

where thermal generation is included in R_p and R_n. Assuming a uniformly doped semiconductor under steady state operation and using the derived equations for the

current densities of holes (39) and electrons (40) we get the time-independent diffusion equations

$$q\mu_p \frac{d}{dx}\left(p\vec{E}\right) - qD_p \frac{d^2p}{dx^2} = q(G - R) \quad (70)$$

And

$$q\mu_n \frac{d}{dx}\left(n\vec{E}\right) - qD_n \frac{d^2n}{dx^2} = q(R - G) \quad (71)$$

Moreover, we assume a region in a p-type semiconductor ($p \cong p_o \gg n_o$) under low injection ($n \ll p_o$) with very small electric field $\vec{E}$ (for example away from a pn junction (quasi-neutral region)), where drift current can be neglected, then equation (70) can be simplified to

$$D_n \frac{d^2\delta n}{dx^2} - \frac{\delta n}{\tau_{SRH,n}} = -G_{(x)} \quad (72)$$

while making the same assumption for an n-type semiconductor we get for equation (71)

$$D_p \frac{d^2\delta p}{dx^2} - \frac{\delta p}{\tau_{SRH,p}} = -G_{(x)} \quad (73)$$

where $\tau_{SRH,n}$ and $\tau_{SRH,p}$ are the carrier's lifetime as they were defined in (58) and (59) and δn and δp the excess carrier concentrations. Note that diffusion equations (72) and (73) are dependent on minority carries properties and thus are commonly referred as minority-carrier diffusion equations.

2.2.5 pn Junctions

As it was discussed in section 2.2.1 the Fermi energy level is a function of doping concentration and temperature which can be argued that is constant throughout a system in thermal equilibrium. Thus, when two materials are brought in intimate contact the Fermi level will be equalized throughout these materials. Qualitatively, this process can be described as follows: Suppose that initially the two materials (A, B) are not in contact, then for each material under thermal equilibrium the electron will be distributed in the energy states of an allowed band (let be $E_{F_A} > E_{F_B}$) with electrons in both cases occupying most of the states below these energies, whereas most of the states above these energies been empty (Figure 2.14(a),(b)). At the moment that the two materials come in intimate contact the electrons will seek to occupy first the states with the lowest energy. Thus, electrons will be transferred from higher energy states of material A to the lower energy states of material B (Figure 2.14(c)). This process will continue until the distribution of electrons, as a function of energy, is the same throughout the two materials and thus the system will have reached a state of thermal equilibrium. This state occurs when the Fermi energy is the same in the two materials (Figure 2.14(d)). This pictorial representation is the basic concept of a pn junction that will be detailed below where the more convenient description of electrons and holes for the charge carriers will be adopted.

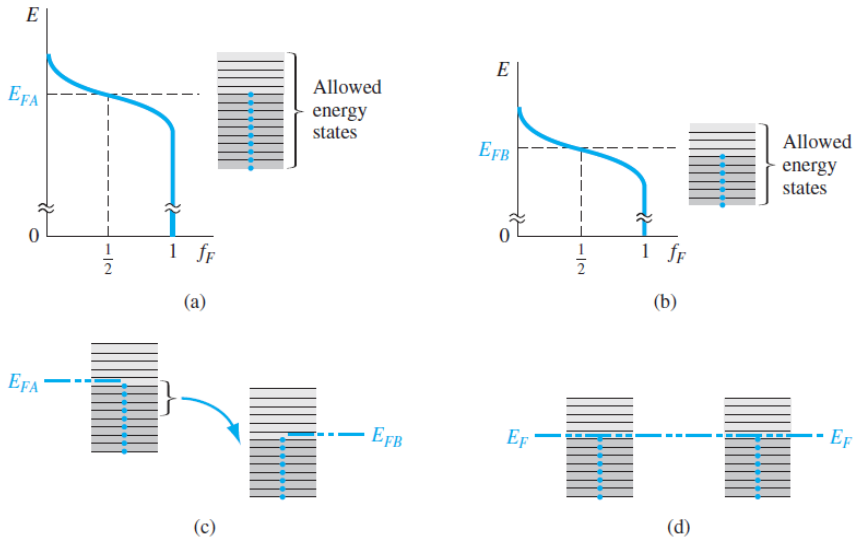

Figure 2.14 The Fermi energy of (a) material A in thermal equilibrium, (b) material B in thermal equilibrium, (c) materials A and B at the instant they are placed in contact, and (d) materials A and B in contact at thermal equilibrium.

When a p-type and an n-type material come into contact a pn junctions is formed and as it was described above the Fermi level will be constant across the system of the two materials without net current flow. More precisely, since the electron and hole concentration differ in the two types of materials, holes will diffuse from the p-type toward n-type and electrons form n-type toward p-type. While majority carriers diffuse from one type of material to the opposite type of material the ionized impurities (N_A^-, N_D^+) are left "behind" which no longer been screened by the majority carriers. As a result, an electric field (or electrostatic potential (Φ) difference) is produced limiting the diffusion process of electrons and holes until thermal equilibrium reached (diffusion and drift currents for each carrier type is balanced), where the produces electrostatic potential difference under thermal equilibrium is called built-in voltage (V_{bi}). The regions x_N, x_P in Figure 2.15 where the majority carriers of one type of material have diffused to the opposite type of material is called space charge region or commonly depletion region since is practically depleted of both types of charge carriers. If the two

materials are thick enough then the regions of both type of materials away from the contact where no diffusions of charge carriers occurred, they are essentially charge neutral ($n \cong N_D \; or \; p \cong N_A$) called quasi-neutral regions.

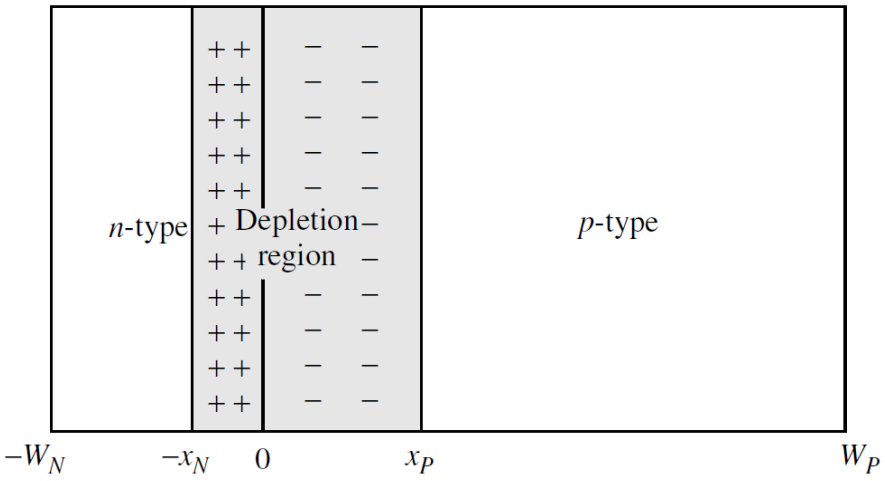

Figure 2.15 pn junction where free carriers have diffused across the junction (x = 0) leaving a space-charge or depletion region practically devoid of any free or mobile charges. The fixed charges in the depletion region are due to ionized donors N_D^+ on the n-side and ionized acceptors N_A^-on the p-side

Suppose a one dimension pn-junction (Figure 2.15) with the metallurgical junction at $x = 0$ where the n-type and p-type materials are non-degenerate, uniformly doped (N_D and N_A, respectively) and fully ionized while also it is assumed within depletion zone ($-x_N < x < x_P$) the $n_o, p_o \ll |N_A - N_D|$ and outside ($x \leq -x_N, x_P \leq x$) the charge neutrality ($n \cong N_D \; or \; p \cong N_A$) it can be argued that the built-in voltage (V_{bi}) can be expressed as

$$V_{bi} = \frac{qN_D}{2\varepsilon} x_N^2 + \frac{qN_A}{2\varepsilon} x_P^2 \quad (74)$$

where ε the dielectric permittivity of the material. Further if we assume that the electric field is a continuous function at the metallurgical junction (no interface charges) then in the depletion region the number of negative charges per unit area in the p region is equal to the number of positive charges per unit area in the n region and mathematical expressed

$$x_N^2 N_D = x_P^2 N_A \quad (75)$$

Practically, (75) states total charge in either side of the depletion region exactly balance each other and therefore the depletion region extends furthest into the more lightly doped side. For example, in Figure 2.15 the p-type semiconductor is lighter doped compared to n-type semiconductor and thus the depletion region (0, x_P) at the p region is larger compared to n-type region. Using equations (74) and (75) we can calculate the full depletion width (W_D)

$$W_D = x_N + x_P = \sqrt{\frac{2\varepsilon}{q}\left(\frac{N_A + N_D}{N_A N_D}\right) V_{bi}} \quad (76)$$

As it was stated earlier under thermal equilibrium condition no current flow, so the hole current density from equation (39) (the same holds also for equation (40) gives

$$\overrightarrow{J_p} = qp\mu_p \vec{E} - qD_p \nabla p = 0 \ (77)$$

and using Einstein relationship (46) we get for the electric field

$$\vec{E} = \frac{kT}{q}\frac{1}{p_o}\frac{dp_o}{dx} \quad (78)$$

Writing the built-in potential V_{bi}

$$V_{bi} = \int_{-x_N}^{x_P} \vec{E}\, dx \quad (79)$$

and using (78) we get an alternative expression for the V_{bi}

$$V_{bi} = \frac{kT}{q} ln\left(\frac{N_A N_D}{n_i^2}\right) \quad (80)$$

In terms of fermi level where as it is illustrated in Figure 2.16 the $e\Phi_{F_P} = E_{F_i} - E_F$, and $e\Phi_{F_n} = E_{F_i} - E_F$ then the built-in potential can be given by $V_{bi} = |\Phi_{F_n}| + |\Phi_{F_P}|$. It should be noted that this potential difference cannot be measured with a voltmeter since a new potential difference will be formed between probes and the semiconductors that will cancel the V_{bi} .

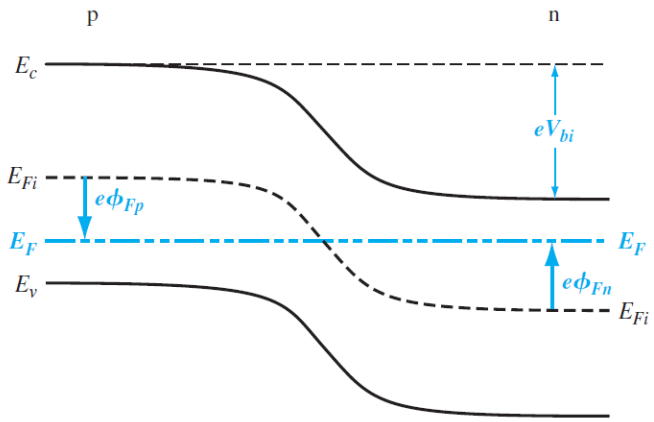

Figure 2.16 Energy-band diagram of a pn junction in thermal equilibrium

Figure 2.17 illustrates the schematic representation of the a) energy band diagram, b) electric field and c) charge density in the vicinity of an abrupt pn junction diode under thermal equilibrium.

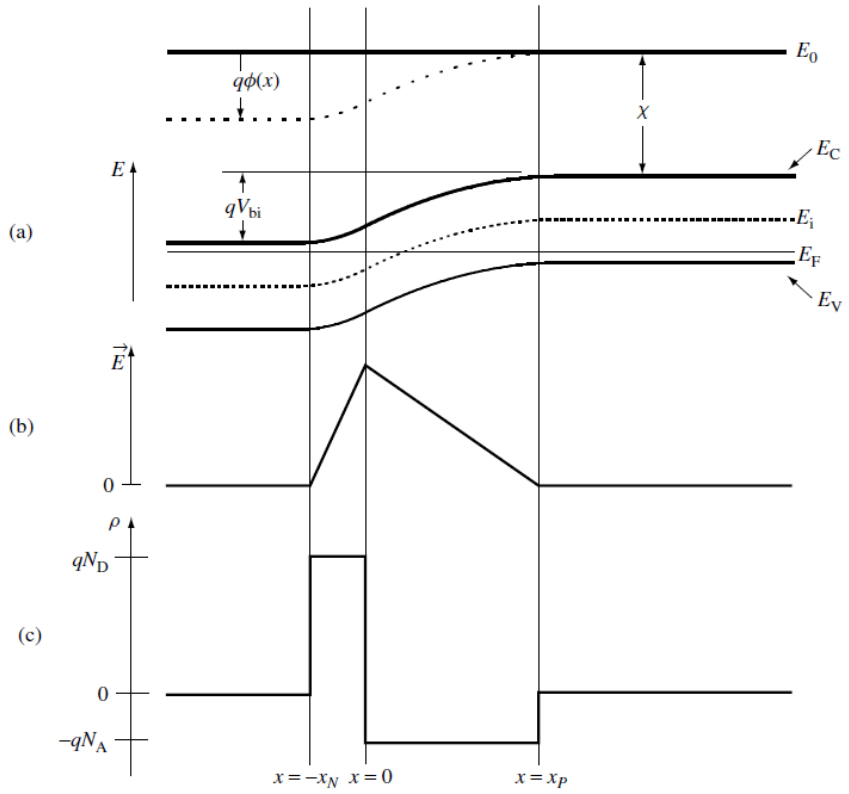

Figure 2.17 Equilibrium conditions in a solar cell: (a) energy bands; (b) electric field; and (c) charge density

As x denoted the electron affinity which is the minimum energy needed to free an electron from the bottom of the conduction band and take it to the vacuum level. The E_0 defines the energy of a free stationary electron outside of any material which serves as a convenient universal reference point called vacuum level. An electron at the vacuum energy is, by definition, completely free of influence from all external forces. The conduction band minimum is given by

$$E_C(x) = E_0 - q\Phi(x) - \chi \quad (81)$$

and the valence band maximum by

$$E_V(x) = E_C(x) - E_G \quad (82)$$

and the intrinsic fermi level from equation (8). Figure 2.17 (b) illustrates the electric field, produces by the unscreened ionized impurities, and Figure 2.17 (c) the charge distribution between the two sides of the depletion region.

Under an external voltage (V) (non-thermal equilibrium condition) the electrostatic potential difference is modified, and the depletion width is dependent on the applied voltage.

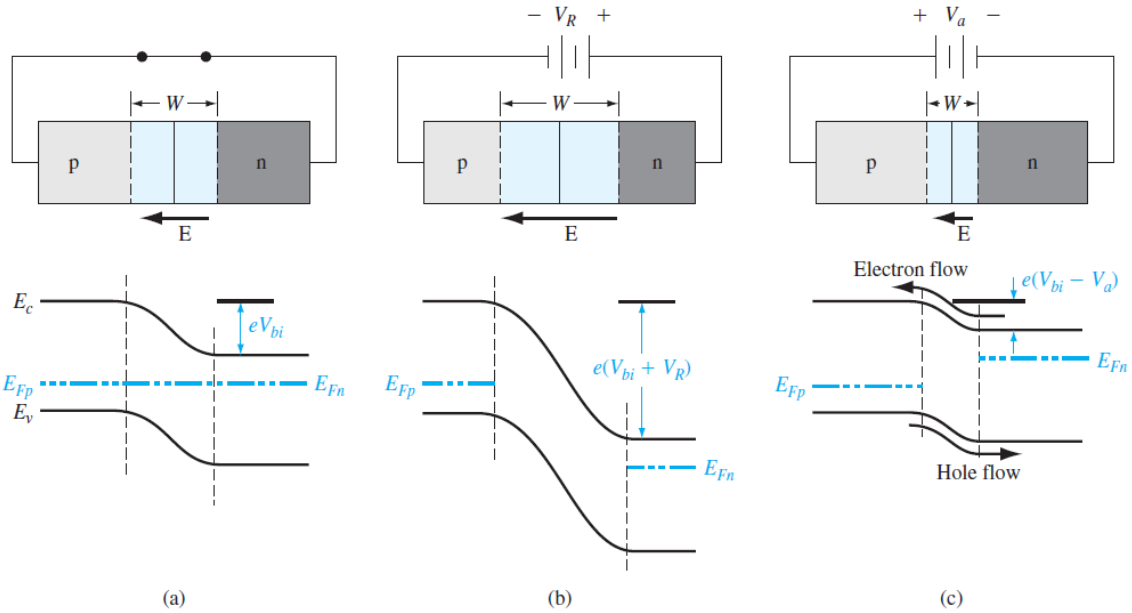

Figure 2.18 A pn junction and its associated energy-band diagram for (a) zero bias, (b) reverse bias, and (c) forward bias

If the applied potential of the n region is positive with respect to the p region (Figure 2.18 (b)) so the fermi level in the n region is lower than that in the p region, the total potential barrier, which holds back the charge carriers to flow (injected) (no current density), is now larger than that for the zero-bias. In this case the pn diode is reversed biased and the depletion width increases calculated by

$$W_D = x_N + x_P = \sqrt{\frac{2\varepsilon}{q}\left(\frac{N_A + N_D}{N_A N_D}\right)(V_{bi} + V_R)} \quad (83)$$

Generation of carriers may occur in the depletion region under reversed bias, thus a current density arises, and as we will see later induce a deviation from the ideal pn junction current. Also, carrier generation due to light will increase the current under reversed bias.

If the applied potential of the n region is negative with respect to the n region (Figure 2.18 (c)) so the fermi level in the p region is lower than that in the n region, the total potential barrier will be reduced. In this case the pn diode is forward biased and the depletion width decreases as external voltage (V_a) increases and is calculated by

$$W_D = x_N + x_P = \sqrt{\frac{2\varepsilon}{q}\left(\frac{N_A + N_D}{N_A N_D}\right)(V_{bi} - V_a)} \quad (84)$$

As a result of the reduced potential barrier the hole and electrons in the p and n region, respectively, are no longer hold back. Therefore, holes will diffuse from the p region across the space charge region, and they will flow (injected) into the n region and inversely for the electrons in the n region. The injected electrons in the p region are minority carriers which will cause recombination and diffusion of the excess carriers in this region while the same applies for the holes in n region. The diffusion of charge carriers generates a diffusion current through the pn junction.

To calculate the forwarded biased current-density it is assumed that the semiconductors a) neutral outside depletion regions , b) low injection levels and complete ionization, c) the lengths of pn junction (W_N, W_P) are very long (the excess

minority carrier concentrations must approach zero at distances far from the depletion region) and d) the total current in the junction is the sum of the individual electron and hole currents that are constant through the depletion region. Further, the minority carriers concentration, where excess carriers $\delta n, \delta p$ exist, is given with the use of quasi-Fermi levels (E_{F_P}, E_{F_n}) definitions

$$p = p_o + \delta p = n_i \left(\frac{E_{F_i} - E_{F_P}}{kT} \right) \quad (85)$$

and

$$n = n_o + \delta n = n_i \left(\frac{E_{F_n} - E_{F_i}}{kT} \right) \quad (86)$$

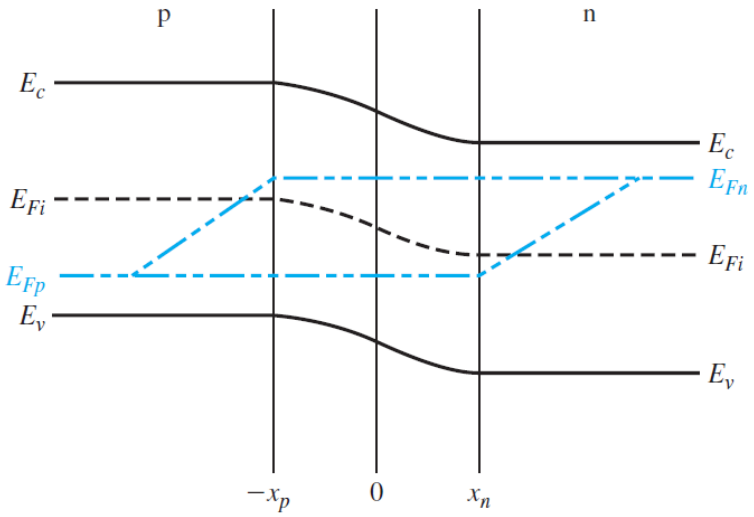

Figure 2.19 Quasi-Fermi levels through a forward biased pn junction.

Where it can show that the difference between quasi-fermi levels is related to applied bias ($E_{F_n} - E_{F_P} = V_\alpha$) representing the deviation from thermal equilibrium. It is noted

that the $E_{F_n} - E_{F_P}$ is nearly constant through the depletion region. Applying the above assumption, it can be derived that the total current density due to hole $J_p(x_N)$ and electron $J_n(-x_P)$ minority carriers in the pn junction, called ideal current–voltage relationship, can be expressed from the function

$$J = J_p(x_N) + J_n(-x_P) = \left[\frac{eD_p p_{n0}}{L_p} + \frac{eD_n n_{p0}}{L_n}\right]\left[exp\left(\frac{eV_\alpha}{kT}\right) - 1\right] \quad (87)$$

where p_{n0}, n_{p0} is the thermal-equilibrium concentration of minority carrier electrons in n and p regions, and $L_p(= \sqrt{D_p \tau_p})$, $L_n(= \sqrt{D_n \tau_n})$ is the average distance a minority carrier can move before recombining with a majority carrier, called "diffusion length", (τ_p, τ_n is the carriers life time) and as assumed above (long pn junction) are much smaller than depletion's regions length ($L_p \ll W_n, L_n \ll W_P$) . Further, the first factor of the product (85) is defined as the parameter

$$J_s = \left[\frac{eD_p p_{n0}}{L_p} + \frac{eD_n n_{p0}}{L_n}\right] \quad (88)$$

referred to as the reverse-saturation current density. Replacing (88) to (87) we get

$$J = J_s\left[exp\left(\frac{eV_\alpha}{kT}\right) - 1\right] \quad (89)$$

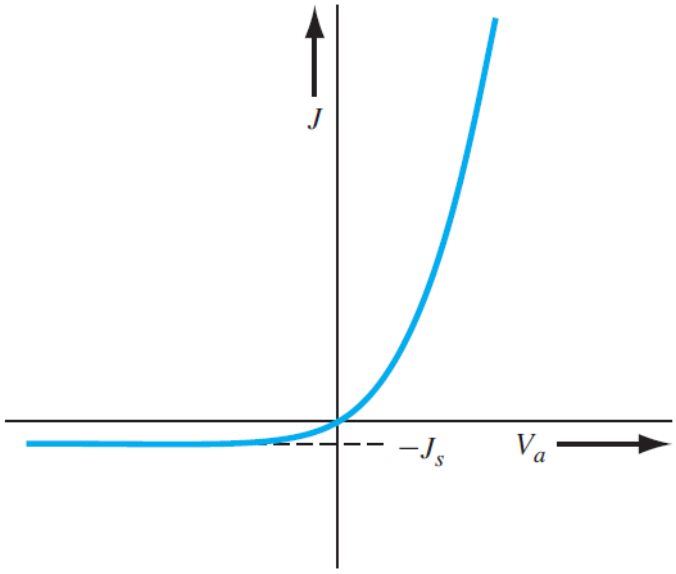

Figure 2.20 Ideal I–V characteristic of an ideal pn junction diode

Although (86) was derived using forward biased pn junction, it is still valid for reversed biased pn junctions. If the applied voltage become a few e/kT negative, then the current density is independent of the applied voltage and equals the reverse-saturation current. Figure 2.20 illustrates a characteristic current–voltage curve of an ideal pn junction diode where obviously is not bilateral.

In a more rigorous handling of the current density at the pn junction additional processes must be considered like the generation of charge carriers in the depletion region rendering the reverse-saturation current voltage depended. Moreover, as is depicted in Figure 2.18(c) under forward bias majority charge carriers are injected across depletion region, in contrast to reversed bias where they are all swept out ($n \cong p \cong 0$), and thus recombination of excess carriers in the depletion may occur. Another process that must be considered is the high-level injection as the forward bias increased. In particular, so far it was assumed that the excess minority carriers concentration is

much lower than majority carrier concentration (low-level injection), but under high forward biases their concentration may become comparable or higher than the majority carrier concentration and thus the current density will be proportional to the excess carrier concentration (high-level injection). Taking in to account the aforementioned processes, a generalization of the current-voltage dependence in a pn junction can be written as

$$I = I_s \left[\exp\left(\frac{eV_\alpha}{A_0 kT}\right) - 1 \right] \quad (90)$$

where the parameters I_s is the reversed saturation current and A_0 the ideality factor. The latter is an indication of how much the diode deviates from the ideal pn junction. In principles, under large forward-bias and $A_0 \cong 1$ diffusion dominates and for low forward bias and $A_0 \cong 2$ recombination dominates, while a transition region exists where A_0 ranges between 1 and 2. Additional, electrical resistance and trap charges at the interface also alter the current-voltage relation of a pn junction.

The descriptions above assumed a pn homojunction. In the case of heterojunctions (two different semiconductor materials are used to form a junction) the basic principles are similar to pn homojunction but the dependence of both the band gap and the electron affinity to the position makes the calculations of energy band diagram and electrostatics more involved. For example, as shown in Figure 2.21(a) the different band gaps of the two materials may create a discontinuity at the junction interface (Figure 2.21(b)) inducing accumulation layer of electrons in localized states at the interface, or the mismatch of the lattice constants may introduce dislocations resulting in additional interface states.

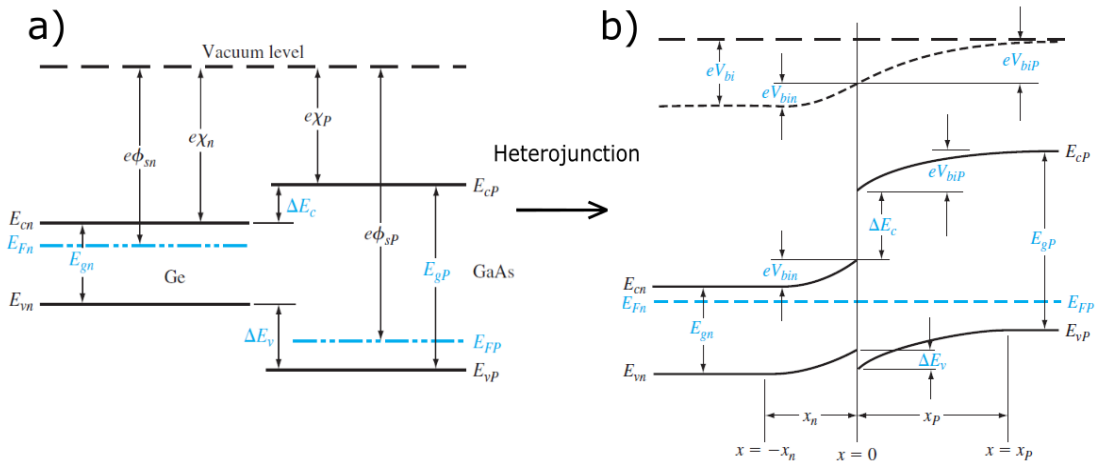

Figure 2.21 Energy-band diagrams of a) narrow-bandgap and a wide-bandgap material before contact, b) ideal nP heterojunction in thermal equilibrium

2.2.6 Solar Cell Devices

Solar cells are semiconductors that absorb light (photons) transforming part of the photons' energy to charge carriers (electrons and holes). In simplest case it consists of a pn diode between two metal electrodes (contacts). After photons absorption the pn diode separates and collect the carries conducting the electrical charges, and thus produce electrical current, to a specific direction (contacts).

The suns' radiation spectrum can be approximated by a black body radiation at 5762 K. The portion of this spectral radiation that reach the earth's atmosphere is about 1353 kW/m^2 and part of this is absorbed by the atmosphere before incident the earth surface. The measurement of how the absorption affects the spectral distribution and intensity called Air Mass (AM) and it is defined as:

$$Air\ Mass = \frac{1}{cos\theta} \quad (91)$$

where θ is the angle of sun incident. As AM0 is defined the spectral distribution and intensity that reach the earths' atmosphere. A common standard that is implied for comparison of solar cells performance is the A.M1.5 spectrum with normalized intensity of 1 KW/m^2. If the diffusion of the sun light on earth's surface is included to the model the letter g (global) is added to its name and if not the letter d (direct). Figure 2.22 shows the solar radiation spectra of the sun (5762 K black body), the one that reach the earth's surface (AM0) and the one that is commonly used for comparison of solar cells' performance (AM1.5g).

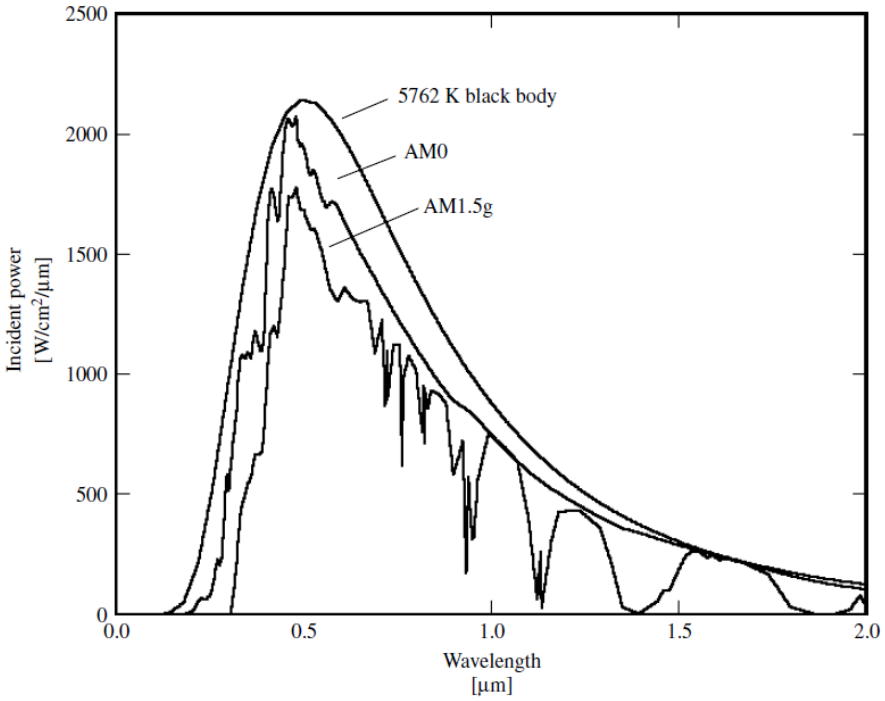

Figure 2.22 The radiation spectrum for a black body at 5762 K, an AM0 spectrum, and an AM1.5 global spectrum [20]

Since only photons with $h\nu > E_G$ can create electron – hole pairs and contribute to the output of the solar cell, then the materials that should be implemented as absorption layers must possess appropriate band gap. Applying a simple analysis (no recombination, perfect light trapping) we can predict the maximum solar cell efficiency (PCE_{max}), often called Shockley-Queisser limit, in respect to absorbers band gap is given by

$$PCE_{max}(E_G) = \frac{\frac{1}{q}E_G I_{inc}}{P_{in}} = \frac{E_G}{(P_{in}/A)}\int_{\lambda<\lambda_G} f(\lambda)d\lambda \quad (92)$$

where $I_{inc}$is the light intensity, $P_{in}$the incident power of light and A the cross section of the solar cell. Figure 2.23 presents the graph for the maximum theoretical efficiency in respect to absorbers band gap for an AM1.5 global spectrum. This simplified approach only serves to demonstrate that for high efficiency solar cells an energy gap ranging between 1.0 and 1.6 eV is a necessity. A lot of physical mechanics affect the efficiency of a solar cell such as spectrum losses, the impedance and recombination of charge carriers, the imbalanced mobility of electrons and holes etc. More sophisticated calculations give a maximum efficiency of 33.7% for a band gap absorber at 1.34 eV.

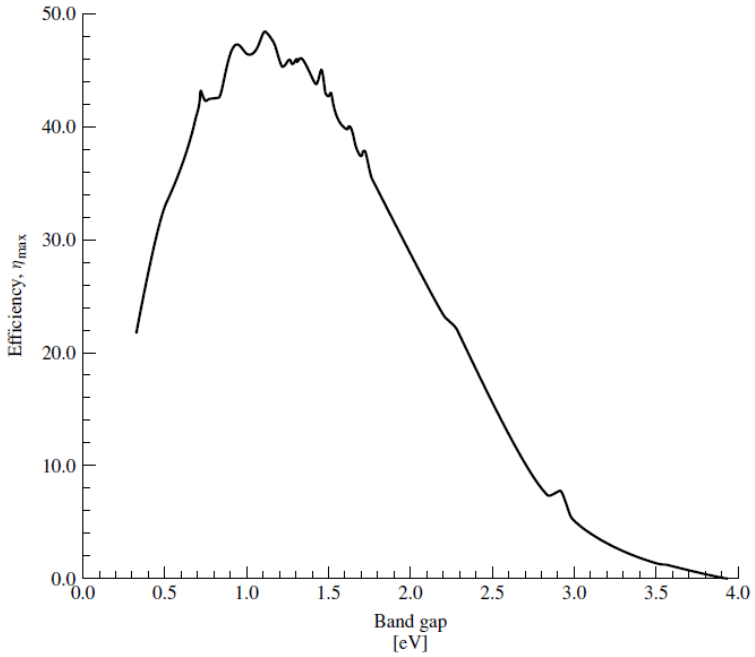

Figure 2.23 Simplified theoretical maximum efficiency as a function of semiconductor band gap for an AM1.5g spectrum

As it was referred a solar cell is a pn junction (Figure 2.15) between to contacts that absorbs photons creating excess carriers which are conducted towards contacts producing current density. As it was shown in chapter 2.2.5 under no illumination and zero external voltage then the system is under thermal equilibrium and thus the Fermi level in constant throughout the semiconductors (Figure 2.18) whereas under non equilibrium conditions (e.g. external bias) the carrier concentration can be expresses in relation to quasi-Fermi levels (equations (85),(86)). Assuming that the majority carriers remain constant at the contacts $x = -W_N, W_P$ (Figure 2.15) the external applied voltage at the contacts can be expresses in relation quasi-Fermi levels

$$qV_\alpha = F_N(-W_N) - F_P(W_P) \quad (93)$$

Under the same assumption as in chapter 2.2.5 for the non-thermal equilibrium pn junction the quasi-Fermi level remains constant inside depletion region (Figure 2.19) and can be written

$$qV_\alpha = F_N(x) - F_P(x) \quad (94)$$

Combining equation (85), (86) and (94) we can get the minority carrier concentration at the edges of depletion region $(-x_N, x_P)$ which deviated from thermal equilibrium due forward-bias voltage V_α

$$p_n(-x_N) = \frac{n_i^2}{N_D} e^{qV_\alpha/kT} \quad (95)$$

and

$$n_p(x_P) = \frac{n_i^2}{N_A} e^{qV_\alpha/kT} \quad (96)$$

where p_n, n_p indicate the hole concentration in n region and electron concentration in p region, respectively. The set of equations (95) and (96) called law of the junction.

Further, we assume that charges recombination occurs at the interface of the pn junction with the contacts ($x = -W_N, W_P$). We get for the excess minority carrier concentration at $x = -W_N$

$$\frac{d\delta p}{dx} = \frac{S_{F,eff}}{D_p} \delta p(-W_N) \quad (97)$$

and for the excess minority carrier concentration at the $x = W_P$

$$\frac{d\delta n}{dx} = \frac{S_B}{D_n}\delta n(W_P) \quad (98)$$

where $S_{F,eff}$, S_B are the effective recombination velocity of the front and back contact interfaces.

The generation rate of electron-hole due to photon absorption was given by equation (55) and assuming that the light incidents at the front side of solar cell, $x = -W_N$, then equation (55) is rewritten as

$$G_{(x)} = (1-s)\int_{\lambda \le hc/E_G} \big(1 - r_{(\lambda)}\big) f_{(\lambda)} \alpha_{(\lambda)} e^{-\alpha(x+W_N)} d\lambda \quad (99)$$

Where the integration is performed for photon with energy (hc/E_G) equal or larger that the band gap (E_G) of the material.

Using the above assumptions, it can be proved that the current produced by a solar cell can be expressed

$$I = I_{SC} - I_{o1}\big(e^{qV/kT} - 1\big) - I_{o2}\big(e^{qV/2kT} - 1\big) \quad (100)$$

where I_{SC} is the short circuit current (includes the photon generated current), I_{o1} is the dark saturation current due to recombination in the quasi-neutral regions, and I_{o2} is the dark saturation current due to recombination in the depletion regions. The I_{SC}, I_{o1}, I_{o2} depend on solar cell structure, materials properties and the operation conditions which renter them rather complex expressions but their examination will could give a full understanding of the solar cell operation. However, the electrical equivalent circuit of equation (100) presented in Figure 2.24 can been very useful to model the device performance.

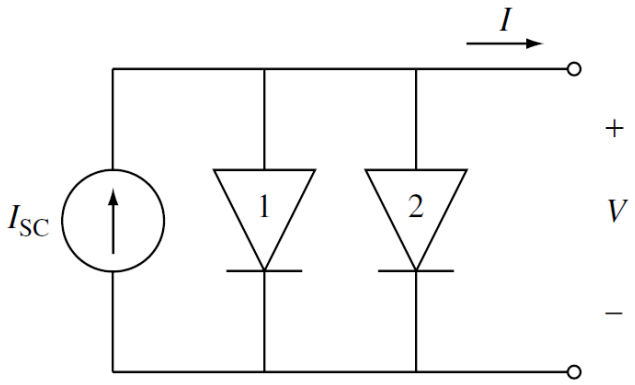

Figure 2.24 Simple solar cell circuit model. Diode 1 represents the recombination current in the quasi-neutral regions ($\approx e^{qV/kT}$), while diode 2 represents recombination in the depletion region ($\approx e^{qV/2kT}$)

The solar cell is modeled by an ideal current source I_{SC} in parallel with two diodes. Taking in to account the generalized expression (90) for the pn diode current voltage it clear that diode (1) has ideality factor $A_0 = 1$, while for diode (2) $A_0 = 2$. In principles, diode (1) represents recombination processes at the surface and in the bulk regions (quasi neutral regions) which are dominant at high voltage and diode (2) recombination at the depletion region which are dominant at low voltages. In reality the ideality factor is a complex function of the carrier concentration (as discussed in section 2.2.5) and thus depends on voltage across the solar cell, nevertheless the aforementioned assumption holds for the low and high region of applied voltage. A characteristic current-voltage (I-V) curve is illustrated in Figure 2.25.

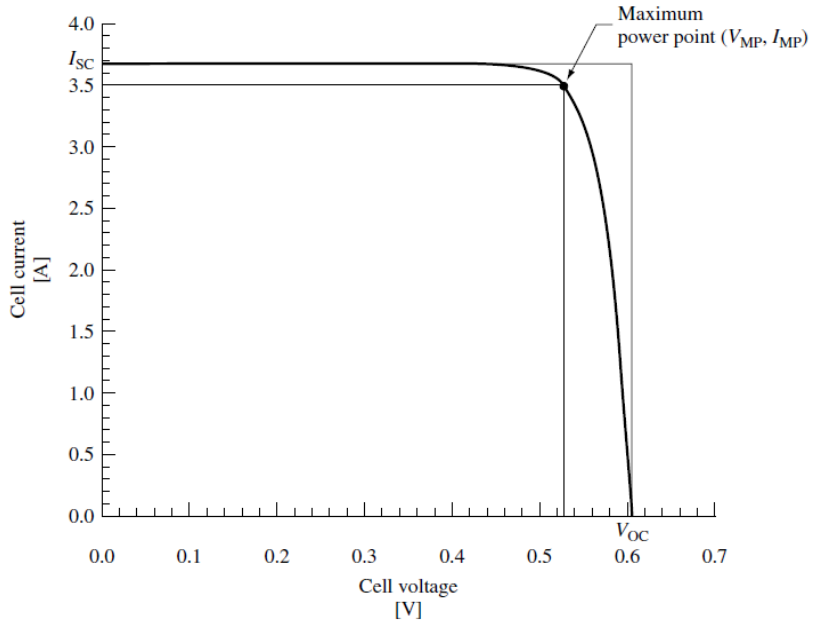

Figure 2.25 Current–voltage characteristic of a solar cell

The main parameters in an I-V curves are the short-circuit current (I_{sc}) at $V = 0$, the open circuit voltage (V_{oc}) at $I = 0$, the fill factor (*FF*) and the maximum power point (V_{MP}, I_{MP}).

A common assumption is that the recombination at the depletion region is very small, which in principles holds for large forwarded-biases, and as a result the dark saturation current (I_{o2}) due to diode 2 can be ignored. Thus, at low voltages, since diode current I_{o1} is very small, it can be assumed that the total current generated by the solar cells is (I_{sc}) at $V = 0$. Increasing the forward-biased voltage, and thus the term $\left(e^{qV/kT} - 1\right)$ becomes significant, the current through diode 1 increases quickly which result in reduction in the delivered current.

At $I = 0$, where all the photon generated current flow through diode 1, the open circuit voltage (V_{oc}) using equation (100) can be written as

$$V_{oc} = \frac{kT}{q} ln \frac{I_{sc} + I_{o1}}{I_{o1}} \quad (101)$$

while making the assumption that the diode current is much lower than the photon generated current $I_{o1} \ll I_{sc}$ we get

$$V_{oc} = \frac{kT}{q} ln \frac{I_{sc}}{I_{o1}} \quad (102)$$

The maximum power point (V_{MP}, I_{MP}) defines the point on the I-V curve where the solar cell produces the highest possible power ($P_{MP} = V_{MP} \cdot I_{MP}$). It can be calculated by solving

$$\left.\frac{\partial P}{\partial V}\right|_{V=V_{MP}} = \left.\frac{\partial (V \cdot I)}{\partial V}\right|_{V=V_{MP}} = \left.\left[I + V \frac{\partial I}{\partial V}\right]\right|_{V=V_{MP}} = 0 \quad (103)$$

for $V = V_{MP}$. Applying the value to equation (100) it gives the I_{MP}. Geometrically, maximum power point represents the point at which the formed rectangle for the various combinations of (I, V) on the I-V curve become maximum; Further, if we define the rectangle corresponding to V_{oc}, I_{sc} then the ration between these two areas is a measure of the squareness of the I-V curves, called fill factor (*FF*). Thus, *FF* is calculated from

$$FF = \frac{P_{MP}}{V_{oc} \cdot I_{sc}} = \frac{V_{MP} \cdot I_{MP}}{V_{oc} \cdot I_{sc}} \quad (104)$$

FF give an indication of how much the diode deviates from an ideal diode and thus the maximum value that it can get is 1.

The most important figure of merit in solar cells is the power conversion efficiency (PCE) and is calculated from

$$PCE = \frac{P_{MP}}{P_{in}} = \frac{FF \cdot V_{oc} \cdot I_{sc}}{P_{in}} \quad (105)$$

where P_{in} is the power of incident light. As it was shown above a common reference light spectrum is the AM1.5g with corresponding P_{in} = 1 KW/m^2 (100 W/cm^2). In principles, for high PCE solar cells it must

1. Minimized the recombination throughout the device
2. Maximized the absorption of photons with energy larger than the E_G

For a more realist modeling of the solar cells the parasitic series (R_s) and shunt (R_{sh}) resistance must be included in the electric equivalent circuit (Figure 2.26). Thus equation (100) is written

$$I = I'_{SC} - I_{o1}\left(e^{qV/kT} - 1\right) - I_{o2}\left(e^{qV/2kT} - 1\right) - \frac{(V + IR_s)}{R_{sh}} \quad (106)$$

where $I'_{SC}$is the sort circuit current without parasitic resistances.

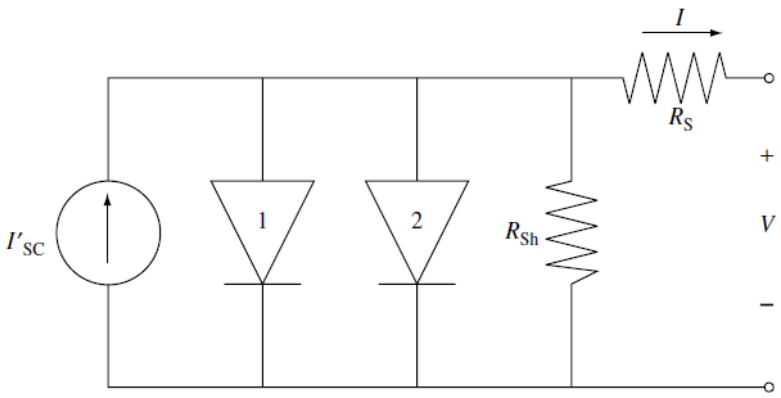

Figure 2.26 Solar cell circuit model including the parasitic series and shunt resistances

The source of the R_s is the quasi-neutral regions as well as the metal contacts, while of R_{sh}, even though there is debate on this topic, any shunting path between contact points outside space charge region and points that induce a high recombination such as structural defects, diffused atoms etc. It should be noted that recombination loses are also reflected in the $I_{o1}$and thus even though the modeling can properly fit the I-V curves the underlying physical mechanism needs deeper investigation. It is more convenient to rewrite equation (106) as

$$I = I'_{SC} - I_o\left(e^{q(V+IR_s)/A_0kT} - 1\right) - \frac{(V + IR_s)}{R_{sh}} \quad (107)$$

where A_0 the diode ideality factor typically ranging between 1 and 2 where for values close to 1 the recombination is dominant in the quasi-neutral region and as it closes to 2 the recombinations are dominant in the depletion region. A typical behavior of I-V under the effect of gradually increased R_s and decreased R_{sh} is presented in Figure 2.27 and Figure 2.28, where it is assumed $R_{sh}(\rightarrow \infty)$ very high and $R_s = 0$, respectively. It can be seen in Figure 2.27 that high R_s reduces the short circuit current (I_{SC}) while it does not affect V_{oc}, whereas in Figure 2.28 low R_{sh} reduces V_{oc}without affecting I_{SC}, it is noteworthy that in both cases *FF* strongly declines for high R_s or low R_{sh}, respectively.

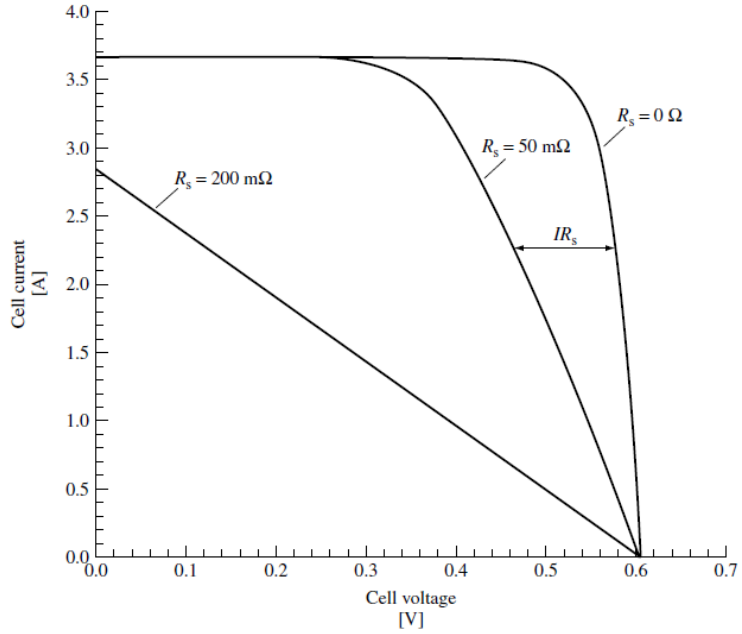

Figure 2.27 Effect of series resistance on the current–voltage characteristic of a solar cell where $R_{sh} \rightarrow \infty$

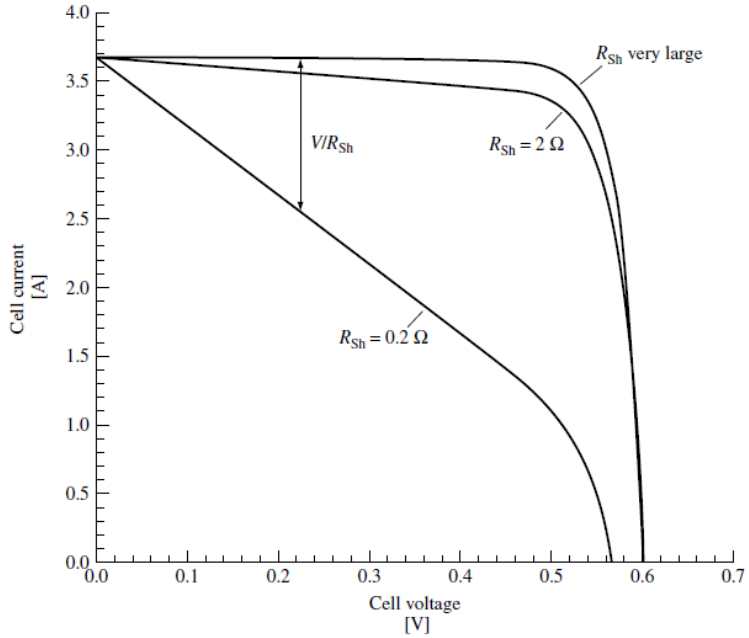

Figure 2.28 Effect of shunt resistance on the current–voltage characteristic of a solar cell where $R_s = 0$

At short circuit conditions ($V = 0$) (107) becomes

$$I_{SC} = I'_{SC} - I_o\left(e^{qI_{SC}R_s/A_0kT} - 1\right) - \frac{I_{SC}R_s}{R_{sh}} \quad (108)$$

while at open circuit ($I = 0$)

$$0 = I'_{SC} - I_o\left(e^{V_{oc}/A_0kT} - 1\right) - \frac{V_{oc}}{R_{sh}} \quad (109)$$

A method to extract the ideality factor A_0 is by illuminating the solar cell with different intensities obtaining the sets of I_{SC}, V_{oc} and plotting $log(V_{oc})$ against I_{SC} (or light intensity). A typical graph is illustrated in Figure 2.29 where it can be seen a region that neither R_s nor R_{sh} are significant (linear region) and thus from the slope (α) of the curve ($\alpha = {A_0kT}/{q}$) can be calculated the A_0, while the y-intercept gives the I_o.

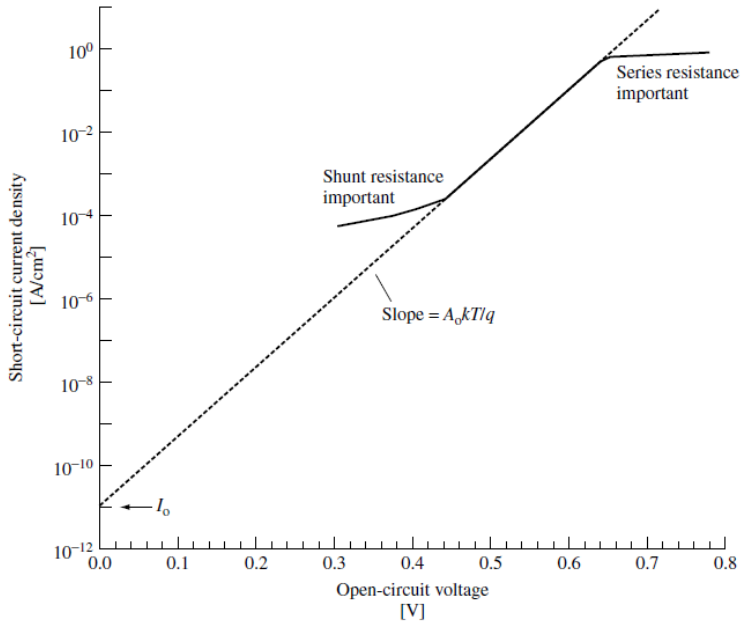

Figure 2.29 Short-circuit current versus open-circuit voltage plot illustrating parameter extraction

Furthermore, it can be utilized the region of low voltage where only R_{sh} are important and at high voltages region where only R_s are important to extract the corresponding values. Concretely, by combining equations (108) and (109) and assuming that only R_{sh} important at the low voltage regime we get

$$\frac{V_{oc}}{R_{sh}} = I_{SC} - I_o e^{qV_{oc}/A_0 kT} \quad (110)$$

and thus plotting V_{oc} against ($I_{SC} - I_o e^{qV_{oc}/A_0 kT}$) we can get R_{sh} from the slope of the line. Similarly, combining equations (108) and (109) and assuming that only R_s important at the high voltage regime we get

$$I_{SC} R_s = \frac{A_o kT}{q} ln\left[\frac{I_o e^{qV_{oc}/A_o kT} - I_{SC}}{I_o}\right] \quad (111)$$

and thus plotting I_{SC} against $\log\left[I_o e^{qV_{oc}/A_o kT} - I_{SC}\right]$ we can get R_s from the slope of the line.

Of great interest in a photovoltaic solar is the spectral response $SR_{(\lambda),}$defining a correlation between generated short-circuit current (I_{SC}) and phtoton's energy. Particularly, the solar cell is illuminated by a narrow spectrum of specified wavelength, and it is measured the generated short-circuit current, while repeating this process for full width of the desired spectra it results in a graph that describes the $I_{SC\,(\lambda)}$of the solar cell for the different wavelengths (λ) normalized by the maximum possible current. It can be measured as the external spectra response (or external quantum efficiency (EQE)) $SR_{ext,(\lambda)}$ and internal spectra response (of internal quantum efficiency (IQE)) $SR_{int,(\lambda)}$. Experimentally, the measurements are performed for EQE and given by

$$SR_{ext,(\lambda)} = \frac{I_{SC_{(\lambda)}}}{qAf_{(\lambda)}} \quad (112)$$

where A is the area of the solar and $f_{(\lambda)}$ is the incident photon flux (number of photons incident per unit area per second per wavelength), then IQE is calculated from optical losses (shadowing, reflectance), and optical thickness. The total I_{SC} is calculated as

$$I_{SC} = \int_{\lambda} SR_{ext,(\lambda)} f_{(\lambda)} d\lambda \quad (113)$$

Another point that must highlighted is the impact of carrier's lifetime and surface recombination on the I-V characteristics of the solar cells. As it is shown in the section 2.2.4 the various recombination process and thus the lifetime of carriers allows to estimate their impact on V_{oc}, I_{SC} and *FF*. Further it will be examined, specifically, the case of carrier lifetime, and thus carrier diffusion length, in the depletion region of the p-type semiconductor. Assuming that carriers' diffusion length (L_n) is much less than the length (thickness) of the p-type semiconductor then the carriers that are generated deeper than one diffusion length are very unlikely to be collected. Using equation (88) accounting only the reverse (dark) saturation current (second term) from the minority carriers ($J_{s,n} = \frac{qD_n n_{p0}}{L_n}$) in the p region and assuming complete ionization ($N_A \cong N_A^-$) so the thermal equilibrium concentration of minority carrier in the p region can be expressed as $n_{p0} \cong \frac{n_i^2}{N_a}$ we get for the contribution in the dark saturation current for an *A* cross-section size

$$I_{o1,n} = qA\frac{n_i^2}{N_A}\frac{D_n}{L_n} \quad (114)$$

while the impact of back contact surface is marginal on the reverse saturation current. On the other hand, if $L_n \gg W_P$ the carriers can reach the back contact surface and the dark saturation current is a strong function of back contact recombination velocity ($S_{B,eff}$). If $S_{B,eff}$ is very large, then we get the short – base approximation

$$I_{o1,n} = qA\frac{n_i^2}{N_A}\frac{D_n}{(W_P - x_P)} \quad (115)$$

Regarding the front contact recombination is a combination of low surface recombination velocity of non-covered area with the high recombination velocity of the ohmic contact at the contacted areas. This effective front contact recombination velocity ($S_{F,eff}$) depends on the solar cell operation point.

A structure of solar cells that is commonly utilized for thin film absorbers are the p-i-n structure. In such structure a thin film of undoped (intrinsic) material which serves as the photon absorber is sandwiched in between doped n and p region (Figure 2.30). The structure utilizes the high absorption coefficient of the intrinsic region, meaning that most of the hole-electrons pairs are generated near the surface, and recalling equation (75), it is clear that most of the solar will consist of depletion region aiding the charge collections and thus compensating the typical low lifetime of material's charge carriers.

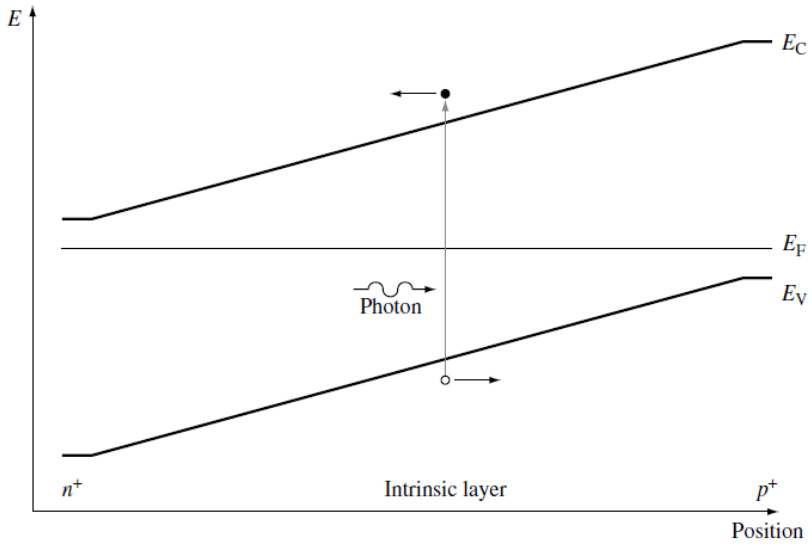

Figure 2.30 Band diagram of a p-i-n solar

The I-V characteristics of p-i-n structures are similar with those presented in the above chapters. One important modification that must be applied in this case is the depletion region (W_D) consisting of the doped n and p regions x_N, x_P and the intrinsic layer W_I

$$W_D = x_N + W_I + x_P \quad (116)$$

Given that the doped layers are very thin the short base approximation holds for this model. Furthermore, there is no back surface recombination ($S_B \to \infty$). The V_{bi} (potential difference across the intrinsic layer) is calculated by the difference on the values of the Fermi levels in the doped regions similar to equation (94). In the case of heterojunctions more complex physical mechanisms may be involved in the operation of the solar cells as it was briefly presented in Chapter 2.2.5.

2.3 Organic-Inorganic Perovskites

2.3.1 Material Properties

Perovskites are a class of materials, named after the Russian mineralogist L.A. Perovski, which crystalize in the same structure as the first discovered mineral of this type $CaTiO_3$. The structure has the general formula ABX_3, where A and B are cations and X is an anion (Figure 2.31). Inorganic perovskites are well investigated materials exhibiting interesting properties (e.g. ferroelectricity, antiferromagnetism, piezoelectricity) which found application in solar renewable technologies (e.g solar-to-fuel) but not in photovoltaic application due to inappropriate optical band gap.[21,22]

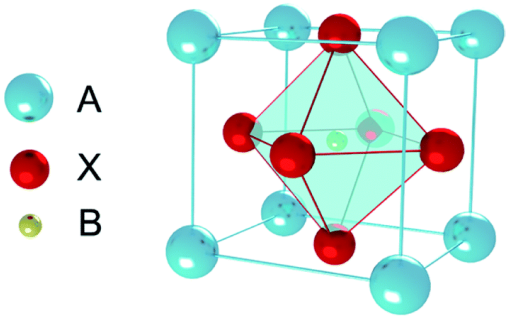

Figure 2.31 ABX_3 perovskite structure.[23]

A new type of organic-inorganic halide perovskite materials where the A is an organic cation, such as methyl ammonium ($CH_3NH_3^+$) (MA) and formamidinium ($NH_2CH{=}NH_2^+$) (FA), B is metal cation (i.e. Pb^{2+}, Sn^{2+}) and X is halogen anion (i.e. Cl^-, Br^-, I^-) exhibit ideal optical band gap for PV applications ranging from 1.25 to 1.75 eV.[24] As it is shown in Figure 2.31 the metal (B) and the halogens (X) form an octahedron which is surrounded by the organic ammonium counter ions (A). Perovskite structure's arrangement were first investigated by Goldschmidt in 1926 who defined an approximate geometrical tolerance factor (t)

$$t = \frac{r_A + r_X}{\sqrt{2}(r_B + r_X)} \qquad (116)$$

where r_A, r_B and r_X are the effective ionic radius for A, B and X ions, respectively.[25] For t = 1.0 the structure is perfectly cubic, while an octahedral distortion (lower symmetry) occurs for t ranging between 0.9 – 1 even though it is compatible for cubic structure influencing its electronic properties.[26] For t ranging between 0.7 – 0.9, which means that A cation is too small, or the B cation is too large, the structure is transformed to orthorhombic, rhombohedral, or tetragonal structure and is unsuitable for photovoltaic application.[24] For large A anions (t > 1) (e.g. Ruddlesden-Popper, Aurivillius, Alkylammonium) a layered perovskite structure is formed.[27,28]

The structure of the various type of perovskite layers are subjected to transformations depending on the temperature. Figure 2.32 presents the temperature related stable states of common perovskites along with the parameters for the different structures, where *α, β, γ* are the corresponding state for high, intermediate and low temperature, respectively, while δ phase is a non-perovskite structure. It should be noted that $MAPbI_3$ exhibit a tetragonal to pseudo-cubic transition at about ~55 ^oC (~325 K) with lattice parameter a= 6.3130 Å.[24] In principles, it can be deduced that by increasing the temperature the crystal symmetry of perovskite's also increases. Interestingly, perovskites that incorporate formamidinium cations ($NH_2CH{=}NH_2^+$) do not experience phase transformation even at high temperatures.

Perovskite	State	Temperature (K)	Architecture	Space group	Lattice Parameters (Å)	Volume (Å^3)
$MAPbI_3$	α	400	Tetragonal	P4 mm	a = 6.3115 b = 6.3115 c = 6.3161	251.6
	β	293	Tetragonal	I4cm	a = 8.849 b = 8.849 c = 12.642	990
	γ	162–172	Orthorhombic	$Pna2_1$	a = 5.673 b = 5.628 c = 11.182	959.6
$MAPbCl_3$	α	>178.8	Cubic	Pm3m	a = 5.675	182.2
	β	172.9–178.9	Tetragonal	P4/mmm	a = 5.655 c = 5.630	180.1
	γ	<172.9	Orthorhombic	$P222_1$	a = 5.673 b = 5.628 c = 11.182	375
$MAPbBr_3$	α	>236.9	Cubic	Pm3m	a = 5.901	206.3
	β	155.1–236.9	Tetragonal	I4/mcm	a = 8.322 c = 11.833	819.4
	γ	149.5–155.1	Tetragonal	P4/mmm	a = 5.8942 c = 5.8612	
	δ	<144.5	Orthorhombic	$Pna2_1$	a = 7.979 b = 8.580 c = 11.849	811.1
$MASnI_3$	α	293	Tetragonal	P4 mm	a = 6.2302 b = 6.2302 c = 6.2316	241.88
	β	200	Tetragonal	I4 cm	a = 8.7577 b = 8.7577 c = 12.429	953.2
$FAPbI_3$	α	293	Trigonal	P3m1	a = 8.9817 b = 8.9817 c = 11.006	768.9
	β	150	Trigonal	P3	a = 17.791 b = 17.791 c = 10.091	2988.4
$FASnI_3$	α	340	Orthorhombic	Amm2	a = 6.3286 b = 8.9554 c = 8.9463	507.03
	β	180	Orthorhombic	Imm2	a = 12.512 b = 12.512 c = 12.509	1959.2

Figure 2.32 State transformations of some common hybrid perovskite materials[15]

Since optoelectronic properties depend on the crystal structure, thus it needs very careful consideration of the working temperature range for the various optoelectronic devices that incorporate perovskite. As it was mentioned $MAPbI_3$ distorts from tetragonal to pseudo-cubic at ~ 55 ^oC which is within the working temperature range of a solar cell. It was measured that both tetragonal and pseudo-cubic phases exhibit a volumetric expansion coefficient of 1.57×10^{-4} K^{-1} which is about 6 times than soda lime, a common used substrate, and much larger than most of the other thin film absorbers.[29] Given that this transition will occur multiple time in a solar cell's lifetime it is of great importance to be considered as regards the structural stability of perovskite solar cell device (PVSC).

The conduction bands edge of the most common perovskite $CH_3NH_3PbI_3$ are mostly composed by the Pb (6p) orbitals while the valence band is a mix of Pb (6p) – I (5p) orbitals.[30] As it is inferred the organic molecules orbitals do not participate directly in the formation of the band edges but contribute to phase structure and crystal polarization. Structural distortions and phase transformations affect the distance between the Pb – I atoms and thus the electronic properties. For the α and β phase of

$MAPbI_3$, which are the most interesting for solar cell applications, first principles calculations (Figure 2.33) have revealed direct band gap semiconductors. Figure 2.33 (a),(b) and (c) show the energy band diagram of α phase for the 001-, 110- and 111-directions of $MAPbI_3$ reciprocal lattice and (d),(e) and (f) the energy band diagram of β phase for the 001-, 110- and 111- directions of $MAPbI_3$ reciprocal lattice.[29] The letters at the x-axis represent special symmetry points of the corresponding crystal structures.

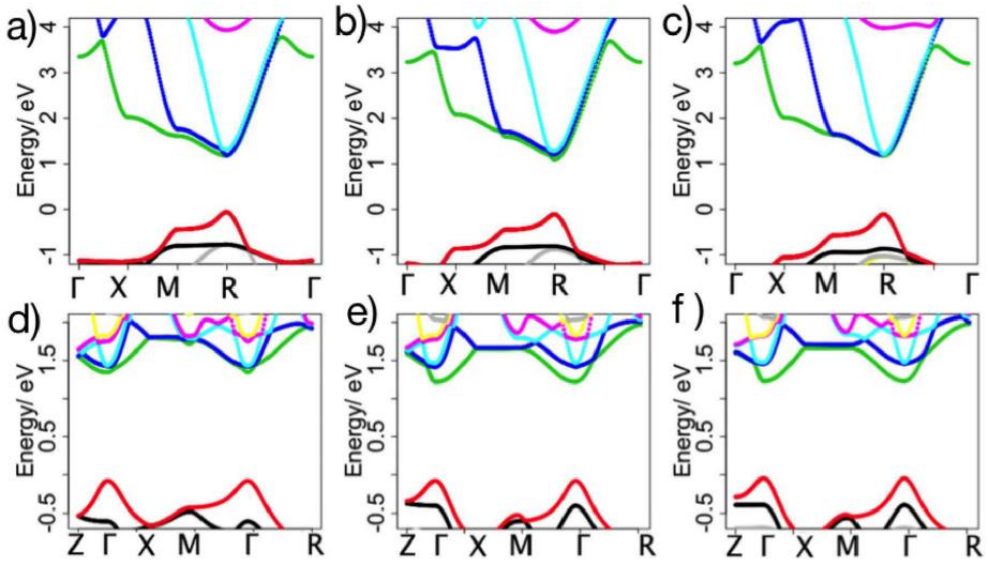

Figure 2.33 The band structure of α phase and β phase optimized with lead relaxed. The (a), (b) and (c) are the band diagrams of α phase, corresponding to 001-, 110- and 111-$MAPbI_3$, respectively. The band diagrams of β phase are shown at (d), (e) and (f) corresponding to 001-, 110- and 111-$MAPbI_3$, respectively.[29]

The maximum effective masses of the photo-generated carriers i.e., without concerning phonon and structural defects or impurities, for the pseudo-cubic phase has been calculated for the electrons in the CB to be $m_e^* = 0.23m_0$ and the holes in the VB to be $m_h^* = 0.29m_0$, which is comparable with these of Silicon. Experimental results have calculated effective hole masses in respect to free hole mass for the pseudo-cubic phase along Γ-X and Γ-M of 0.35 ± 0.15 and 0.24 ± 0.10, which is in good agreement with theoretical calculate values.[31] As a result, perovskite exhibit long-range ambipolar

transport properties and high electron and hole mobilities with the former been slightly higher.[32] An additional indirect band gap formation has be proposed for the pseudo-cubic structure due to rotation of the organic molecules leading to its interaction with the PbI_6 octahedral. As a result, it is suggested, that the different orientation of organic molecules induce an average band gap due to two step absorption profile (Figure 2.34), where it was calculated a direct band gap (E_G) at 1.423 eV (871 nm) and one at 1.611 eV (769 nm) and an indirect band gap at 1.629 eV (761 nm).[33] Single crystal steady-state absorption and photo luminance measurements (Figure 2.35) have given a direct band gap (E_G) of 1.51 eV (820 nm).[34]

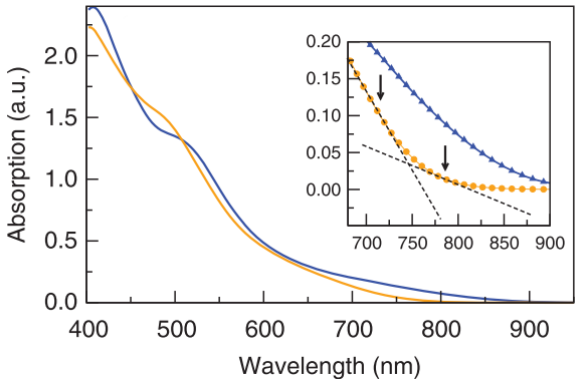

Figure 2.34 The calculated absorption spectra are plotted for the different orientation of CH_3NH_3 showing the impact the organic cation rotation. The inset is a magnification of the same quantity around the low-energy region[33]

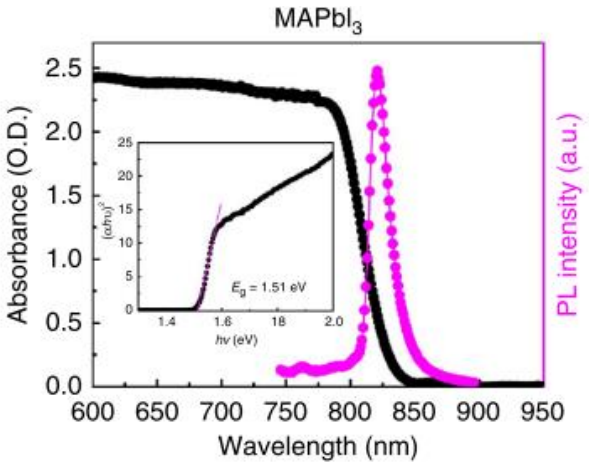

Figure 2.35 Steady-state absorption and photoluminescence of $MAPbI_3$ single crystal. Insets: corresponding Tauc plots displaying the extrapolated optical band gaps.[34]

Except the appropriate optical band gap another important parameter of the $MAPbI_3$ for solar cell applications is the high absorption coefficient, which is comparable to the other emerging thin films (Figure 2.36) enabling the fabrication of thin film perovskite solar cells structures.[35]

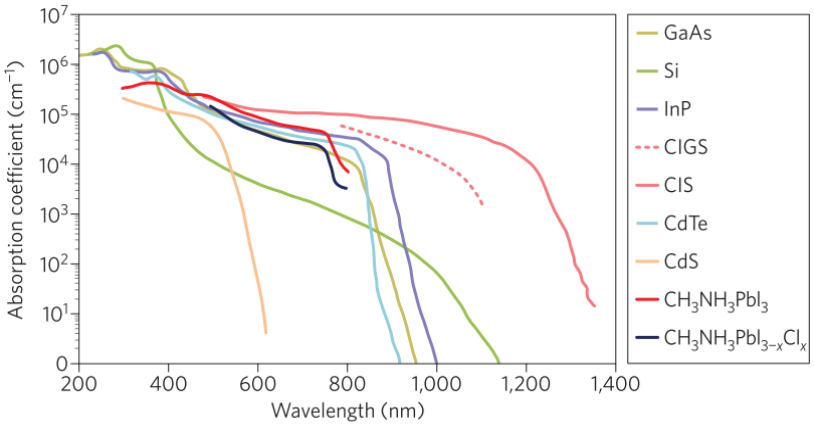

Figure 2.36 Absorption coefficient of $CH_3NH_3PbI_3$ and $CH_3NH_3PbI_{3-x}Cl_x$ compared to other solar cell materials.[35]

The most significant advantages of $CH_3NH_3PbI_3$ compared to the other thin film absorbers is the high "defect tolerance" (Figure 2.37). Meaning that even though there is a high density of structural defects, its low energy formation defects (easier to be

created) such as the vacancies or surface-related sites introduce energy states close or inside the band edges. The creation of deep defected (traps) are ascribed to antisites (substitutional) defects which have high formation energy.[36]

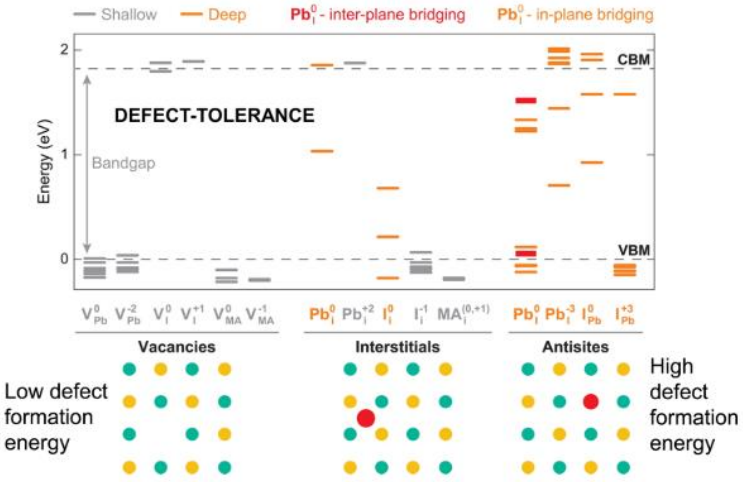

Figure 2.37 Energy levels associated with the defect states corresponding to neutral and charged vacancies (V_{Pb},V_I,V_{MA}), neutral and charged interstitials (Pb_i,I_i,MA_i), and neutral and charged states associated with antisites (Pb_I and I_{Pb}) in $MAPbI_3$[36]

It has also been shown that structural defects change the doping type of $CH_3NH_3PbI_3$. Specifically, PbI_2 deficient $CH_3NH_3PbI_3$ attributed to Pb rather than I vacancies due to lower energy formation induce a p-type characteristics. On the other hand, PbI_2-rich/MAI-deficiency film $CH_3NH_3PbI_3$ attributed to I vacancies rather than Pb interstitials and MA vacancies due to higher energy formation induce an n-type characteristics. The measured energy levels for the ratio PbI_2/MAI illustrated in Figure 2.38 show the shift of the Fermi level, and thus the doping type of $CH_3NH_3PbI_3$, by controlling the stoichiometry of the film.[37]

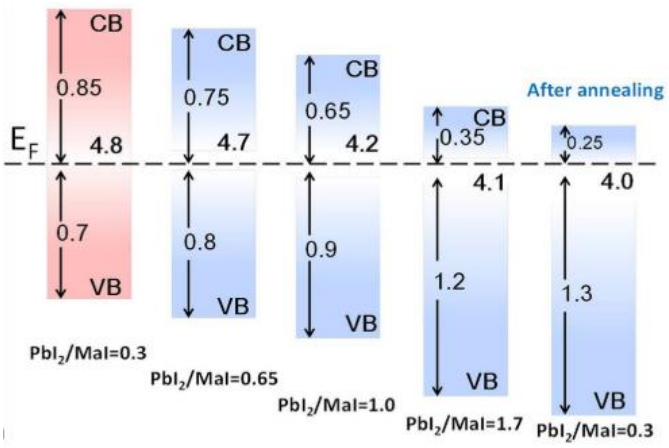

Figure 2.38 Energetic levels of perovskite films formed by one-step method with different precursor ratios of 0.3, 0.65, 1.0, 1.7 (left four columns), and 0.3 precursor-ratio film after annealing at 150 °C for 45 min (right column).[37]

As a consequence of the low effective masses of excited charge carriers and the high "defect tolerance" it is expected that $CH_3NH_3PbI_3$ would exhibit high charge carriers diffusion lengths and thus high mobility and low recombination rate even for polycrystalline films. Henry J. Snaith *et. al.*, applying a combination of quasi steady-state photo-conductivity measurements with photo-induced transmission and reflection, managed to extract accurate values for the aforementioned properties for polycrystalline films in lateral direction and long distances (4 mm) in respect to charge carrier concentration. For the analysis they assumed equal effective charge carrier masses and equal number densities for free electrons and hole.

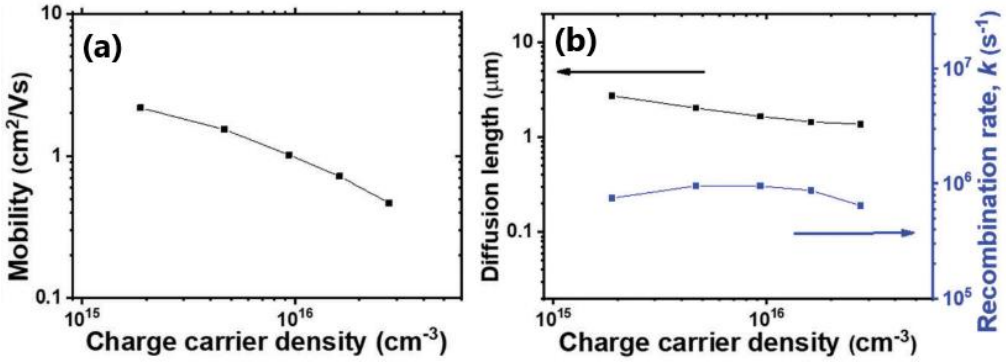

Figure 2.39 Evaluation of photo-induced optoelectronic properties of $MAPbI_3$. (a) Charge carrier mobility (average between electron and hole) (b) charge carrier diffusion length and pseudo-first order recombination (k) rate.[38]

As a result, the charge carrier mobilities (Figure 2.39 (a)) were determined 0.47 to 2.2 $cm^2V^{-1}s^{-1}$ in respect to carrier densities, with the latter being within working photovoltaics' regime (10^{14}–10^{16} cm^{-3}). The authors argued that despite the lower calculated values compare to Terahertz measurements, which have given higher mobilities (20 to 40 $cm^2V^{-1}s^{-1}$), their results are more realistic for applications since their measuring method includes longer range scattering and trapping effect at grain boundaries and defects. Despite the lower values, the diffusion length was calculated to range between 2.73 to 1.37 μm which is still much longer compare to common $CH_3NH_3PbI_3$ thickness range (350 – 550 nm) used in PVSC.[38]

Beyond the standard formulation of perovskite $CH_3NH_3PbI_3$ more advanced formulas have been produced enabling the tailoring of the electronic properties of perovskites. Applied substitutes of methylammonium cations are the formamidinium (FA), Cesium (Cs), Potassium (K) while for halide anions have been used I, Br and Cl. For example, by adding different amounts of Bromide (Br) substituting Iodide (I) atoms in $MAPbI_3$ films, Sang Il Seok *et. al.* have managed to tune the optical band gap and

thus the color of the films (Figure 2.40). As a result, doping $MAPbI_3$ with 6% Br (at. %) (x=0.06) leads to PVSC with higher PCE and extended life time.[39]

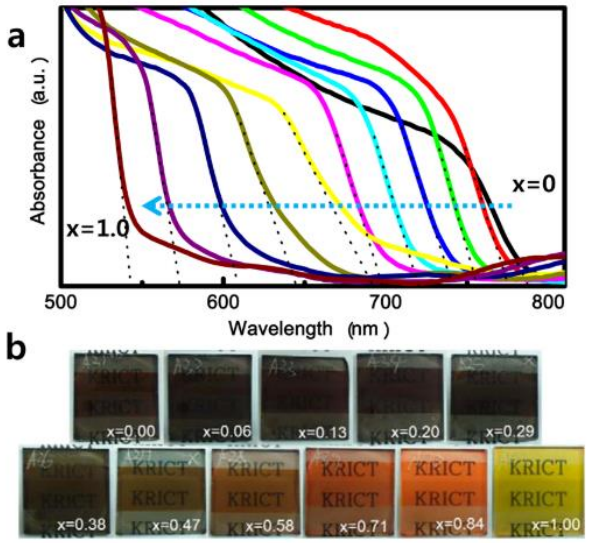

Figure 2.40 Photographs and UV−vis absorption spectra of $MAPb(I_{1-x}Br_x)_3$. (a) UV−vis absorption spectra of FTO/bl-TiO_2/mp-TiO_2/$MAPb(I_{1-x}Br_x)_3$/Au cells measured using an integral sphere. (b) Photographs of 3D TiO_2/ $MAPb(I_{1-x}Br_x)_3$ bilayer nanocomposites on FTO glass.[39]

Moreover, in combination with the above-mentioned anions and cations substitutes a great plethora of organic and inorganic molecular additives have been reported to improve both the power conversion efficiency and the stability of the perovskite solar cells.[40–44] In one of the first reports regarding additive use, Po-Wei Liang et .al. added 1 % wt % 1,8-diiodooctane (DIO) in the perovskite solution to control the crystal growth kinetics. The fabricated perovskite films exhibited a much smoother and denser morphology (Figure 2.41) resulting to higher PCE (~12 %) perovskite solar cells compared to pristine perovskite solar cells which delivered a PCE of 9.0 %.[45] In another report, Chao Shen et al applied a methyl ammonium-free perovskite which was engineered by the addition of sulfonyl fluoride-functionalized

phenethylammonium to stabilize $FAPbI_3$ structure. It was demonstrated that the interaction of sulfonyl group can enhance the crystallinity and simultaneously passivate the surface defects. With this strategy, the perovskite films exhibited better moisture resistance resulting in air stable perovskite solar cells for more than 1000 h, with the unmodified perovskite solar cells showing a significant reduction of PCE within 100 h after fabrication.[46]

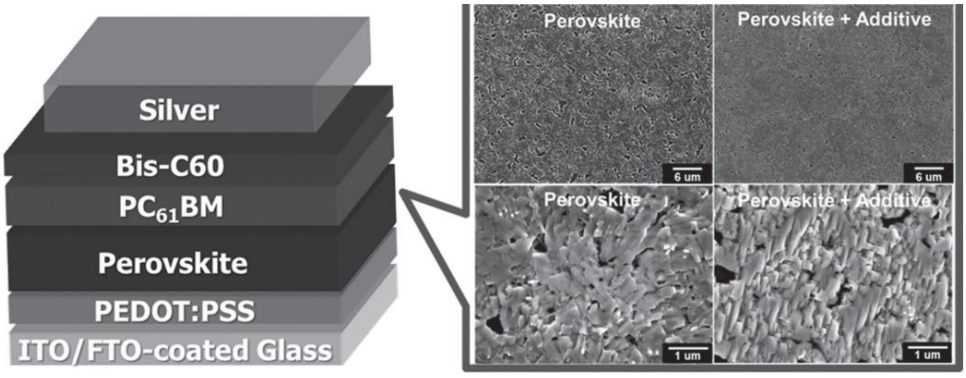

Figure 2.41 Device configuration of the planar-heterojunction solar cell, the cross-section SEM of the planar-heterojunction, and the surface SEM images of the $CH_3NH_3PbI_3$ layer.[45]

2.3.2 Perovskite Solar Cells Structures

Perovskite solar cells have shown an incredibly fast power conversion efficiency (PCE) improvement as it was stated in the introduction. Throughout these years a lot of parameters have been investigated such as the element composition[47–52] and preparation method of perovskite[53–62], device configuration[63–67], materials and preparation conditions of hole/electron transporting layers[68–74].

Regarding the established configurations of perovskite solar cells it can be classified to mesoscopic or planar, in both cases an n-i-p or p-i-n heterojunction

layering has been implemented (**Error! Reference source not found.**).[75] In brief, m esoscopic structure layering begins with the deposition of compact electron transporting layer (ETL) or hole blocking layer on top of a transparent conductive oxide (TCO) (e.g. FTO or ITO), which prevents the contact of perovskite with the TCO suppressing recombination of charge carriers. Then, a highly porous n-type material (typically a metal oxide) is deposited enabling the next deposited perovskite to infiltrate into the matrix and "sensitize" the n-type material. The role of mesoporous layers is to accept the photo-generated electrons from the perovskite and transfer it to the contact. The advantage of this structure is the extended interface area formed between perovskite and the mesoporous structure aiding the electron extraction. After perovskite a p-type material is deposited, serving as hole transporting layer (HTL) or electron blocking layer, followed by a metal conduct fabricating a n-i-p mesoscopic perovskite solar cell. By replacing the p-type materials with n-type and inversely the structure is called p-i-n mesoscopic perovskite solar cell. The disadvantaged of these structures is the high temperature needed for the formation of mesoporous layers as well as the complexity of the porous formation along with the efficient filling with active layer.

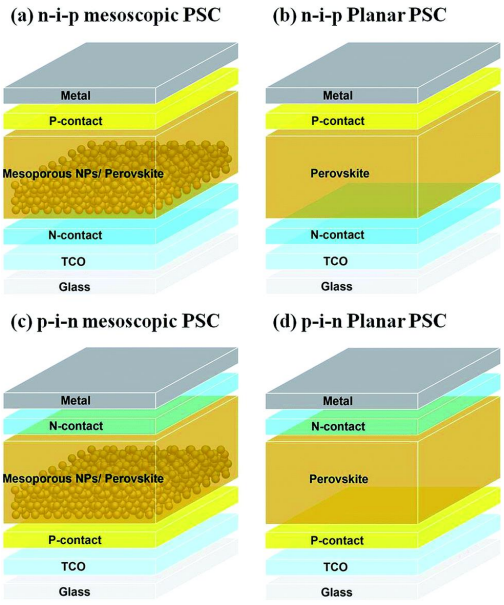

Figure 2.42 Device structures of (a) n-i-p mesoscopic, (b) n-i-p planar, (c) p-i-n mesoscopic and (d) p-i-n planar perovskite solar cells.[75]

Based on the high diffusion length of perovskite's charge carrier a more facile structure was proposed, where all the layers consist of thin films, called planar perovskite solar cells. In this configuration a film of p-type material (HTL) is deposited on a TCO followed by a perovskite film and then a film of n-type material (ETL) is deposited prior to metal contact. This is called p-i-n planar perovskite solar cell, while replacing the p-type materials with n-type and inversely the structure is called p-i-n planar perovskite solar cell. The advantage of this structure is the simpler structure and the lower fabrication temperatures since no mesoporous layers is needed enabling also the easy production of perovskite solar cells on flexible plastic substrates.

Focusing on the charge transport layers (p or n type materials), as it was referred, their function is to form a space charge region through the (hetero-) junction in each side of the intrinsic layer (perovskite) so to effectively collect and transfer the appropriate charge carriers while also block the opposite charges to flow toward the

metal contacts. Moreover, they prevent the direct contact of the perovskite with the metal contacts, which may form a Schottky or ohmic junction (inappropriate for p-i-n or n-i-p structures). Even though both charge transport layers have the same role in PVSC, the formed interfaces as well as the structural properties of the perovskite are fundamentally different due to the layer-by-layer structuring of solar cell devices.

Taking for example a planar p-i-n structure, the upper n-type layer is deposited on solidified perovskite layer and thus the upper perovskite surface is thermodynamically stable prior to deposition. This enables the experimental determinations of their physicochemical properties for better choice of n-type materials, yet modification may occur depending on the deposition conditions of the upper layer such as the reaction with the solvent of p-type's precursor in case of solution processed layer. On the other hand, perovskite is formed on top of the p-type materials (underlayer) and thus HTL's morphology and surface physicochemical properties affects the nucleation dynamics and the chemistry of the reaction; Therefore, the final bulk and interface properties of the perovskite film is a rather complicate process which ultimately defines the PVSC performance.[76–83] As a result, the effect of underlayer's intrinsic properties in a PVSC performance must be examined in regard to the changes it has induce to perovskite's properties

2.3.3 Hole Transporting Layers in Perovskite Solar Cells

A variety of materials that have been used as HTL that can be classified according to their chemical structure in organic, inorganic and those based in carbon (carbonaceous). The classification along with some representative materials are presented in Figure 2.43.[84]

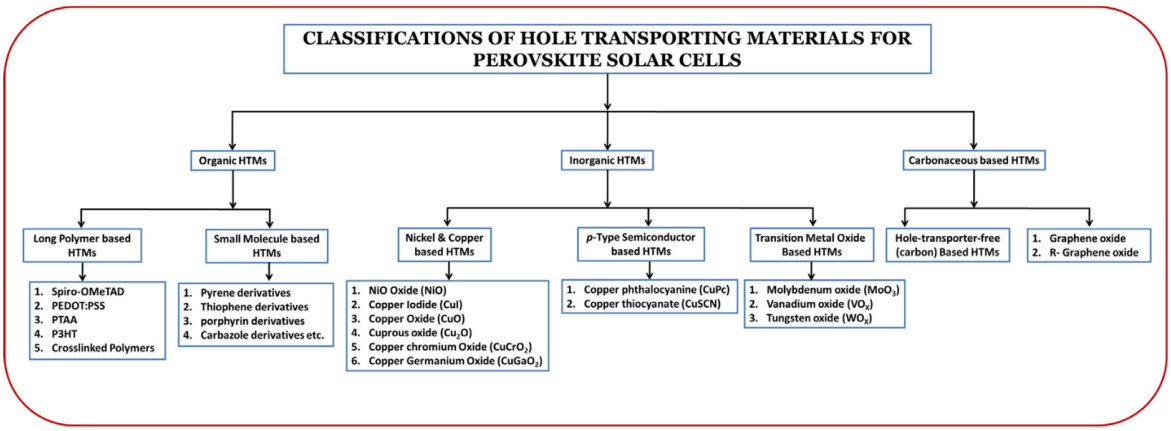

Figure 2.43 classification of hole transporting materials (HTMs)[84]

The requirements a material must fulfill in order to be implemented as underlayer HTL in perovskite solar cells are:[85]

A. Compactness without pinholes, to prevent leakage currents between perovskite layer and the TCO.
B. Good optical transmittance, i.e., wide band gap and minimal reflectivity over the solar spectrum range, to minimize optical losses of incoming light.
C. High electrical conductivity to minimize electrical losses for charge carrier transport in the layer.

D. Energy level alignment with vacuum level and valance band maximum i.e., good electronic coupling to perovskite, for an efficient charge transfer to the adjacent perovskite film and thus minimal energy losses. Moreover, a high lying conduction band to block the charge transfer of electrons from perovskite to HTL.
E. Chemical inertness and electronic properties that enable trap passivation for efficient charge transfer.

Figure 2.44 illustrates valence band maximum and conduction band minimum of commonly used ETL and HTL along with the different types of organic-inorganic perovskites.[86] The advantaged of organic HTM are the solution-process ability, infinite variety, easy fabrication and mechanical flexibility. Nonetheless, the low hole mobilities make necessary the use of "sophisticated" dopants and additives which generally are expensive and suffers from poor stability.[87–90] To overcome these drawbacks inorganic p-materials have been implemented as alternative HTL such as NiOx, CuOx , CuI, CuSCN, $CuCrO_2$.[91–95] The Inorganic materials that are used have wide optical band gap (thus high transparency in the visible range), superior hole mobility compare to inorganic and they can be solution processed, yet their sensitivity towards oxygen and moisture arise some issues. Carbon-based HTL seems to be one viable solutions to instability but the corresponding devices are still delivering lower efficiencies compare to devices using the previous mentioned materials.[96,97]

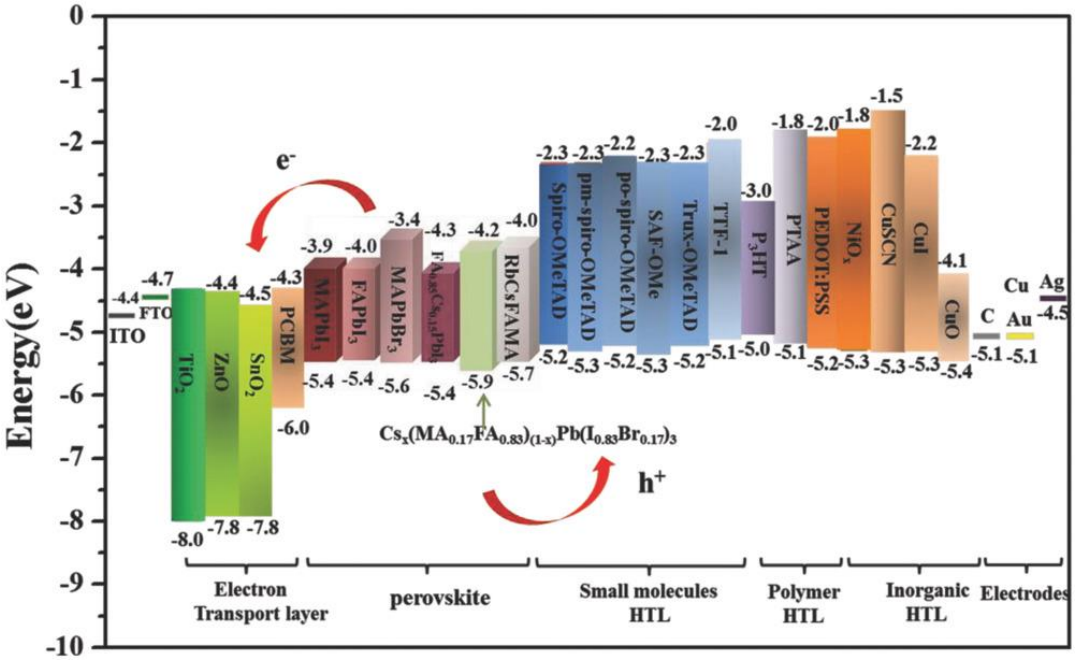

Figure 2.44 Scheme of the energy levels for perovskite materials and commonly used ETLs, HTLs, along with the electrodes for high performance perovskite solar cells.[86]

A common method to tailor inorganic HTL properties so to better match its energy levels with the perovskite and induce a higher electrical conductivity is through extrinsic doping. In a representative work, Wei Chen *et. al.* doped NiOx nanoparticles with an optimized 5% Cu (Cu:NiOx) achieving a higher p-doping resulting in higher electrical conductivity and a better energy level alignment.[98] The increased conductivity was assigned to the Cu dopant rather than the formation of nickel vacancies (V_{Ni}^{+2}) as it was proposed earlier.[99] The Cu:NiOx were spin coated as HTL in p-i-n perovskite structure as it is schematically illustrated in Figure 2.45 (a) forming a compact layer (Figure 2.45 (c)). Additionally, to increased conductivity the authors suggested a better VBM energy alignment with the perovskite reducing energy losses (Figure 2.45 (b)). As a result the PVSC incorporating Cu:NiOx delivered an increased

performance (Figure 2.46) for device area 0.08 cm^2 compare to undoped NiOx with negligible hysteresis in the forward and backward measurements (a usual issue in PVSC) and increased photo response as it was inferred from external quantum efficiency measurements Figure 2.45 (f). For larger area PVSC (1 cm^2) using Cu:NiOx also high performing PVSC were achieved. The reported average PCE was 16.57±0.97 % and with highest performing device showing a PCE of 18.07 % with increased photo response compared to undoped NiOx (Figure 2.45 (g,i)). Other successful doping leading to enhanced performing PVSC compered to undoped material are for example of NiOx with Li, Cs, Ag , Co,Mg or of CrO_x with Cu e.t.c.[100–105]

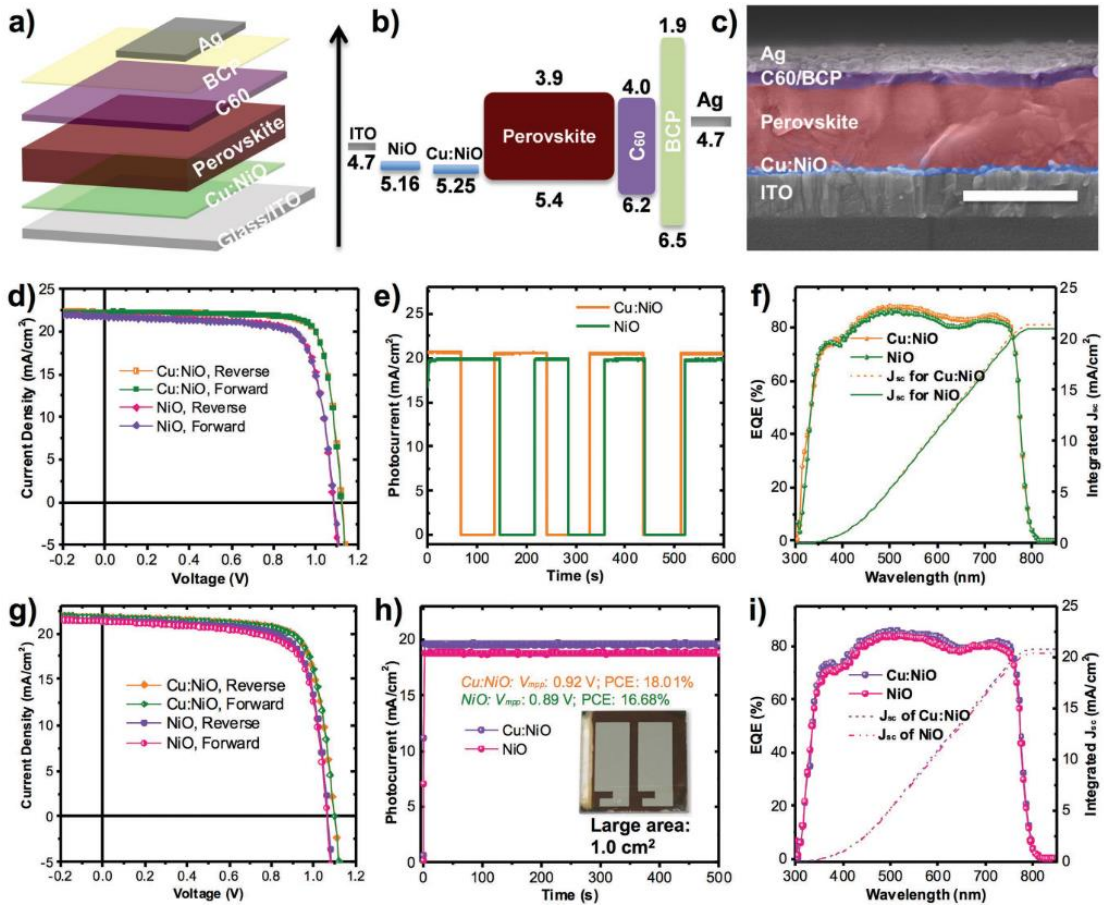

Figure 2.45 a) Structural illustration of the inverted planar perovskite solar cells (PSCs), b) schematic diagram of energy levels at the inverted PSCs, c) cross-section scanning electron microscopy (SEM) image of an inverted PSC with Cu:NiO HTL (scale bar: 500 nm). d) current–voltage characteristics of the optimal NiO and Cu:NiO-based inverted PSCs at reverse and forward scan condition, e) photocurrent density as function of time at fixed applied voltage (Vmmp); f) EQE spectra and integrated Jsc curves of the corresponding optimal NiO and Cu:NiO devices. g) Current–voltage curves of the optimal large-area NiO and Cu:NiO-based inverted PSCs under reverse and forward scan, h) steady photocurrent output at fixed applied voltage (Vmmp) over 500 s, inset shows a photograph of large-area device, i) EQE spectra and integrated Jsc curves of the corresponding optimal large-area devices.[98]

Small devices	Scan direction	J_{sc} [mA cm^{-2}]	J_{sc} by EQE [mA cm^2]	V_{oc} [V]	FF [%]	PCE [%]
NiO	Reverse	21.48 ± 0.16[a)] (21.74)	20.95	1.049 ± 0.02 (1.09)	74.3 ± 1.6 (76.7)	16.67 ± 0.97 (18.18)
	Forward	21.71		1.09	76.1	18.02
Cu:NiO	Reverse	21.96 ± 0.16 (22.28)	21.39	1.097 ± 0.017 (1.12)	78.1 ± 1.5 (81.2)	18.76 ± 0.75 (20.26)
	Forward	22.23		1.12	80.9	20.15

Figure 2.46 Summary of photovoltaic parameters of rigid inverted PSCs with NiO and Cu:NiO HTLs. Device area is 0.08 cm^2.[98]

The solution combustion synthesis of Cu:NiOx and NiOx has been reported as a facile and low temperature method for fabrication of HTL for perovskite applications. Jae Woong Jung et. al. have shown the solution combustion synthesis of Cu:NiOx films at 150 ^oC (Figure 2.47) which were used as HTL for $MAPbI_3$ solar cell. The Cu:NiOx solution combustion synthesis based devises delivered higher power conversion efficiency (PCE) perovskite solar cells compared to devices where Cu:NiOx was formed by a conventional sol-gel synthesis.[106]

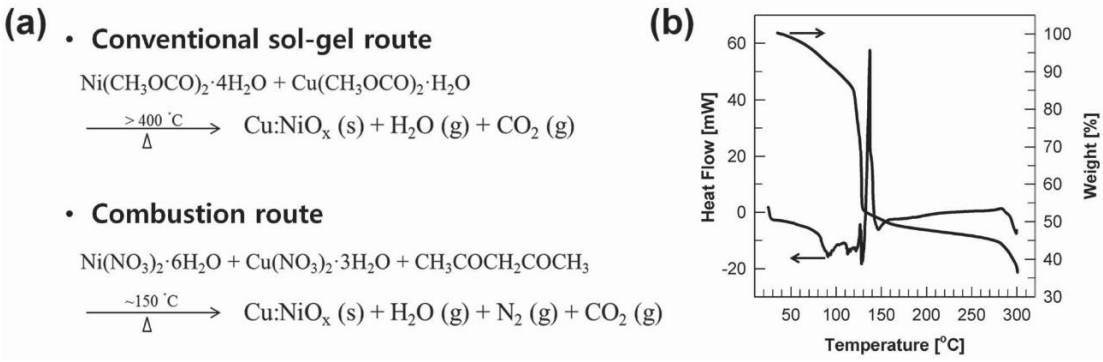

Figure 2.47 a) Depiction of the synthetic routes for Cu:NiOx and b) DSC and TGA curves of the prepared Cu:NiOx via the combustion process[106]

Process for Cu:NiO_x	V_{OC} [V]	J_{SC} [mA cm^{-2}]	FF	PCE[a)] [%]
Combustion	1.05	22.23	0.76	17.74 (17.30)
Conventional sol–gel	1.05	20.53	0.72	15.52 (15.14)

[a)]Average PCE in bracket (over 12 devices).

Figure 2.48 Device parameters of the PVSCs with Cu:NiOx HTL prepared through combustion and conventional sol–gel methods.[106]

In other solution combustion synthesis reports of pristine and doped NiO_x, which were implemented as HTL in Perovskite solar cells, a range of annealing temperature was used for the film formation.[107–112] Ziye Liu et. al. fabricated $MA_{1-y}FA_yPbI_{3-x}Cl_x$ based perovskite solar cells applying the solution combustion synthesis for the formation of NiO_x resulting in devices with PCE higher than 20 %. The annealing temperature used for the NiOx formation was 250 ^oC whereas a 150 ^oC annealing temperature induced a rapid deterioration of the devices.[110] Thus, solution combustion synthesis of metal oxide films is an easy process for production of functional HTL. Despite that, detailed investigations on solution combustion synthesis process studies concluded that synthesis of thin films are different from the corresponding bulk analogues and their low temperature combustion synthesis behavior should be not deduced by the analogue bulk materials, while suggesting that during the processing of thin film precursors it is unlikely to occur combustion synthesis.[113–118]

Regarding NiOx HTLs co-doping strategies with Cu/Li, Mg/Li, Ag/Li have also been successfully implemented resulting in increased efficiencies for the corresponding PVSCs.[119–121] For example, the Mg/Li doped NiOx was used as HTL in 1 cm^2 active area p-i-n perovskite. The undoped and codoped NiOx layers was deposited by means

of spray pyrolysis forming 20 nm of compact layer. Hall Effect measurements revealed a ~12 fold increment ($2.32x10^{-3}$ S cm^{-1}) with a rise in carrier concentration from 2.66 x 10^{17} cm^{-3} to 6.46 x 10^{18} cm^{-3} for the undoped and Mg/Li codoped NiOx, respectively. Moreover, the codoped NiOx enables the better much of the HTLs valance band with the perovskite compared to unwanted energy shifts as it is illustrated in Figure 2.49. As a result, the PVSC exhibited an increased efficiency for the codoped NiOx of 18.3 % compared to undoped NiOx (14.7%). Additional measurements attributed the increased efficiency to rapid extraction of charge carriers (charge transport) which induced a slower interfacial recombination.[120]

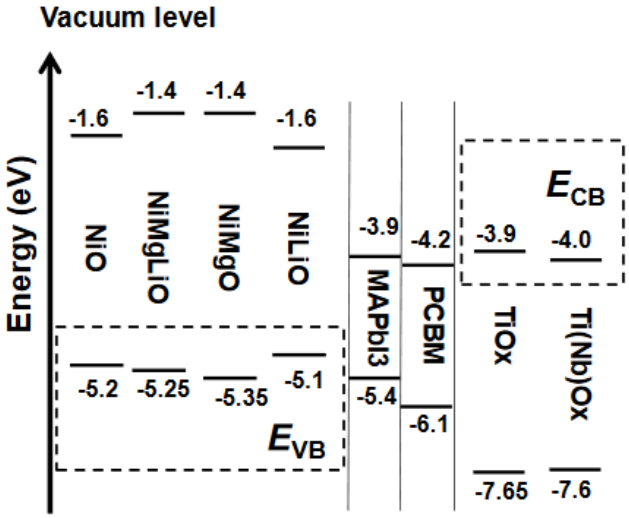

Figure 2.49 Calculated band edge positions of the charge extraction layers with respect to $MAPbI_3$ and PCBM.[120]

Interfacial Conditions	J_{sc}(mA cm^{-2})	V_{oc} (V)	*FF*	*PCE* (%)	R_{sh} (Ohm cm^2)	R_s(Ohm cm^2)
NiO/TiO_x	18.7	1.036	0.640	12.4	1978	7.38
NiO/Ti(Nb)O_x	19.2	1.047	0.731	14.7	3597	5.43
NiMgLiO/TiO_x	20.0	1.074	0.768	16.5	2237	3.59
NiMgLiO/Ti(Nb)O_x	20.4	1.083	0.827	18.3	5605	2.45

Figure 2.50 Photovoltaic performance metrics of the typical devices employing various combinations of charge transporting layers.[120]

3 Materials and Methods

3.1 Materials

A. Indium Tin oxide (ITO) (Anode)

Soda lime glass 14.8 x 14.8 x 1.1 mm substrates with patterned ITO-coated were purchased from Psiotec Ltd. The sheet resistance, thickness and transmittance of the ITO films is 4-5Ω/sq., 200-300nm and >85%, respectively. The specific pattern is shown in Figure 3.1. After the deposition of the stacking layers a device active area of 9 mm^2 is formed as it is illustrated with yellow at the pattern enabling the fabrication of four different devices.

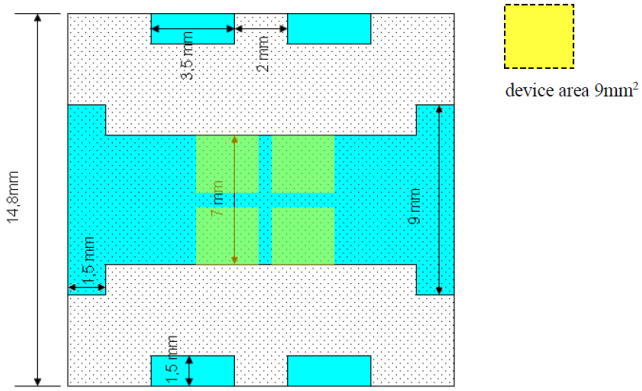

Figure 3.1 Scheme of the patterned ITO (cyan) on-top of soda lime glass substrate. Yellow squares show the 9mm^2 active area of the devices.

B. Precursors for HTL synthesis

For the fabrication of HTL the precursor materials

- Nickel Nitrate Hexahydrate ($Ni(NO_3)_2.6H_2O$) > 98.5 %
- Copper (II) nitrate trihydrate ($Cu(NO_3)_2 \cdot 3\ H_2O$)> 99 %
- Cobalte Nitrate Hexahydrate ($Co(NO_3)_2.6H_2O$) > 99 %
- tartaric acid ($C_4H_6O_6$) 99.5%
- 2-methoxy ethanol ($C_3H_8O_2$) 99.8%
- Copper Nitrate trihydrate ($Cu(NO_3)_2.3H_2O$) > 99%
- Lithium acetate dihydrate ($Li(CH_3CO_2).2H_2O$) 99.999%
- Nitric acid (69 wt% HNO_3)

were purchased from Sigma-Aldrich (now MERCK) and were used with no further purification.

- PEDOT/PSS (Al 4083)

were purchased from Heraeus Clevios™ and were used with no further purification.

C. Precursors for Perovskite synthesis

For the fabrication of organic-inorganic perovskite

the precursor materials

- Lead acetate trihydrate ($Pb(CH_3CO_2)_2.3H_2O$) 99.995%
- Lead (II) iodide (PbI_2) 99.999% trace metals basis

was purchased from Alfa Aesar

- methyl ammonium Iodide (CH6IN) 99%
- methyl ammonium Bromide (CH6BrN) 99%

were purchased from Dyenamo Ltd.

- N,N-Dimethylformamide, anhydrous ($HCON(CH_3)_2$) 99.8%
- Cesium iodide (CsI) 99.999% trace metals basis
- Formamidinium iodide (FAI) ≥99%, anhydrous
- Nitrobenzene ($C_6H_5NO_2$), ≥99.0%

were purchased from Sigma-Aldrich (now MERCK).

All the materials were used with no further purification.

D. Precursors for ETL synthesis and Cathode

For the fabrication of ETL the precursor materials

- [6,6]-Phenyl-C71-butyric acid methyl ester ($PC_{70}BM$) > 99 %

was purchased from Solenne BV

- Chlorobenzene, anhydrous (C_6H_5Cl) 99.8 %
- Bathocuproine (BCP), sublimed grade, 99.99% trace metals basis

was purchased from Sigma-Aldrich (now MERCK).

- Aluminum (Al) cylindrical pellets 99.999%
- Copper (Cu) cylindrical pellets 99.999%

were purchased from GoodFellow company

All the materials were used with no further purification.

E. Encapsulation

For the encapsulation an ultra-violet curing epoxy resin purchased from Ossila Company, under the product name E131. After the application of the resin the devices were covered by 11 x 11 x 0.55mm glass slides and left for 2 minute in UV curing.

3.2 Processing Techniques

3.2.1 Doctor Blade

The deposition of thin films on various substrates can be achieved using doctor blade. In this process (Figure 3.2), a specific amount of ink (solution) is applied in the gap between the substrate and the blade which then moving forward coats the substrate forming a film as the ink dries due to solvent evaporation. The coating parameters are the moving speed and distance of the blade from substrate, the substrate's temperature and together with the properties of the ink such as the concentration and the viscosity define the finals film's characteristics. Doctor blading is a material saving technique and in combination with its large-scale compatibility render it ideal for high throughout production.

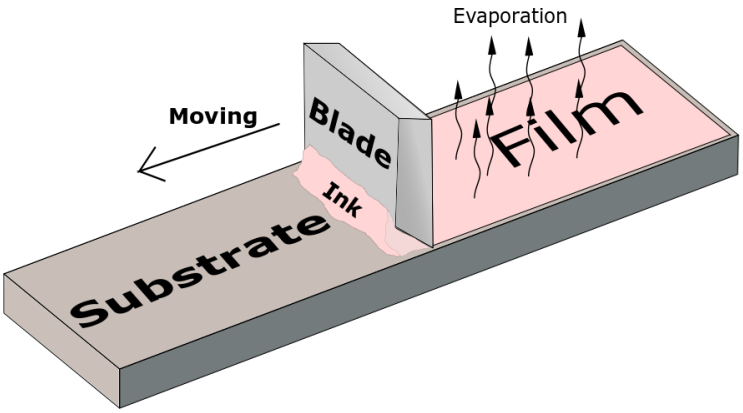

Figure 3.2 Schematic representation of blade coating technique

3.2.2 Spin Coating

In spin coating a substrate is fixed on a substrate holder, then a specific amount of solution is disposed on the substrate and then holder is start rotating rotation of the holder (static coating) or the solution is dripped while the holder is rotating (dynamic coating). The rotation causes radial liquid flow, while air flow promotes solvent evaporation forming a homogeneous thin film (Figure 3-8).

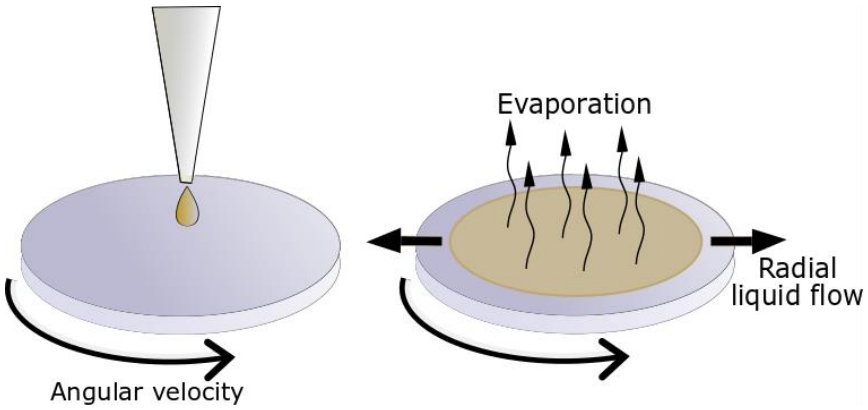

Figure 3.3 Schematic representation of the spin coating technique

Besides solution concentration and viscosity, and ink-substrate interaction, the parameters that determine the final thickness and homogeneity of the layer are angular velocity, spinning time and solvent drying kinetics. In general, the faster is the angular velocity, the thinner films will be deposited.

3.2.3 Thermal Evaporation

In thermal evaporation (or physical vapor deposition (PVD)) the source material, usually in form of powder, is placed in boat which is heated to its boiling or sublimation point in base pressure ~10^{-6} mbar. This process creates a vapor pressure (or vapor stream) of material's atoms or molecules which fills the chamber and condensate on the exposed substrates' surface. To achieve a better thickness homogeneity the substrates are fixed on a rotating holder. The rate of deposition as well as the final thickness of the film is controlled by an oscillating quartz crystal with a precision of ~1Å. The thermal evaporator used in this thesis is the Covap II 200/400 from Angstrom Engineering Company, which is attached to a glovebox system (Figure 3.4).

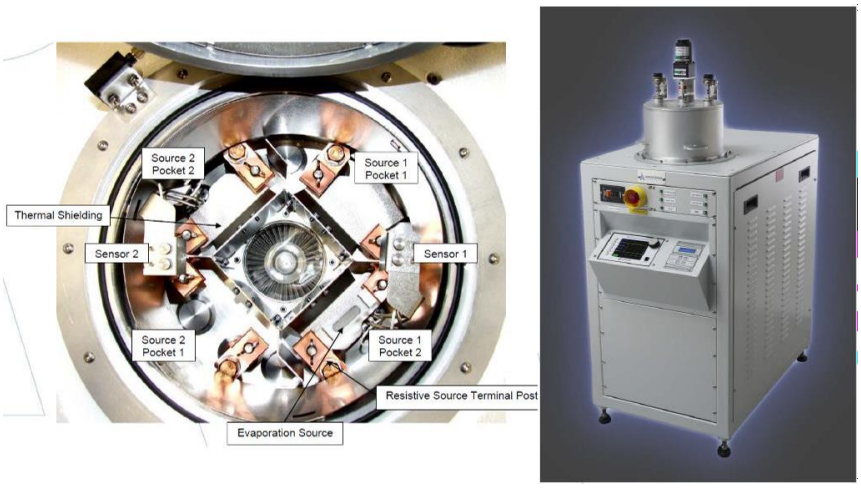

Figure 3.4 Angstrom Engineering Company thermal evaporator

3.3 Thin Films and Solar Cells Fabrication

3.3.1 Substrates Cleaning

Before use the ITO patterned substrates were sequentially ultra-sonicated in acetone and isopropanol for 10 min. Then, the samples were blown with dry air and placed on a hotplate for a few minutes at 120 ^{o}C. Finally, a UV-O_3 treatment for 5 min was applied to remove any remaining organic impurities from the surface.

3.3.2 Hole Transporting Layers

For the solution combustion synthesis of $NiCo_2O_4$ NPs, 0.5 mmol $Ni(NO_3)_2.6H_2O$, 1 mmol $Co(NO_3)_2.6H_2O$, and tartaric acid were mixed in the 15 mL 2-methoxy ethanol solution For the preparation of the doped $NiCo_2O_4$ appropriate amounts of $Cu(NO_3)_2.3H_2O$ and $Li(CH_3CO_2).2H_2O$ where added to the previous solution for 5 mol% Cu and 3 mol% Cu – 2 mol% Li respectively. Then, 150 uL HNO_3 (69 wt% HNO_3) were added slowly into the mixture, and the solution stirred up to almost complete homogeneity. The ratio of the total metal nitrates and tartaric acid was 1. Thereafter, the violet-colored solution was used for the combustion synthesis of the $NiCo_2O_4$ NPs on the various substrates. Doctor blade technique was applied for the fabrication of the precursor films on the various (ITO, glass,quartz) substrates. The resulting light violet-colored films were dried at 100 °C for 30 min and used as a precursor for the combustion synthesis of $NiCo_2O_4$ NPs. Subsequently, the obtained

films were heated at 250 °C and 300 °C in ambient atmosphere for 1 h in a preheated oven to complete the combustion process.

For the solution combustion synthesis of Cu: NiOx or NiOx HTLs, a solution combustion process similar to that of Jae Woong Jung et al. was followed.[106] In details, 0.95 mmol $Ni(NO_3)_2 \cdot 6H_2O$ and $Cu(NO_3)_2 \cdot 3H_2O$ 0.05 mmol (or 1 mmol $Ni(NO_3)_2 \cdot 6H_2O$ for NiOx) were dissolved in 1 mL 2-methoxy ethanol by stirring for about 15 min. Then, 30.65 μL acetylacetonate was added to the solution and stirred for 1 h in room temperature. The doctor blade technique was applied for the fabrication of the precursor films and the resulting films were dried at 100 °C for 5 min. Subsequently, the obtained films were heated at 300 °C in air for 1 h on a preheated hot plate to complete the combustion process.

For PEDOT:PSS films the PEDOT:PSS (AI 4083) solution was used without any treatment. The fabrication of PEDOT:PSS was performed in air, where 50 μL was spin-coated on ITO using the static method at 4000 rpm for 30 s and then annealed at 150 °C for 15 min.

After the annealing all films were left to cool down at room temperature for at least 5 min and then transferred into the glovebox.

3.3.3 Perovskite Layers

The perovskite solution was prepared 30 min prior spin coating by mixing $Pb(CH_3CO_2)_2.3H_2O$:methylamonium iodide (1:3) at 40 wt% in dimethylformamide (DMF) with the addition of 1.5% mole of MABr. The precursor was filtered with 0.1

μm polytetrafluoroethylene (PTFE) filters. The precursor solution was deposited on the various HTLs by static spin coating at 4000 rpm for 60 s and annealed for 5 min at 85 °C, resulting in a film with a thickness of ~350 nm

For the preparations of the triple cation $Cs_{0.04}(MA_{0.17}FA_{0.83})_{0.96}\ Pb(I_{0.83}Br_{0.17})_3$ perovskite solutions a previous reported method was used.[106] The perovskite films were fabricated on the CU:NiOx by spin-coating the solution at 5000 rpm for 35 s and after 10 sec 300 mL of ethyl acetate were dropped onto the spinning substrate as the anti-solvent to achieve the rapid crystallization of the films. The resulting perovskite films were annealed at 100 ^{o}C for 60 min.

The methylammonium free (CsFA) perovskite active layers were fabricated applying deposition parameters, similar to Kelly Schutt et al..[122] Specifically, the perovskite precursor solution was deposited (45 μL on 1.5 × 1.5 cm substrate) on the NiOx (PEDOT/PSS) and spin-coated for 10 s at 1000 rpm and then for 35 s at 6000 rpm. During the second step and 10 s before the end, 100 μL of chlorobenzene was drop casted on the substrate and the film changed color from bright yellow to brown within the next few seconds. Then, the films were annealed at 80 °C for 1 min on a hot plate followed by 100 °C annealing for 10 min

3.3.4 Electron Transporting Layers

The $PC_{70}BM$ precursor solution was prepared with a concentration of 20 mg mL^{-1} in chlorobenzene and left under stirring and heat (65^{o}C) over night. Then, 35 μL of solution was dynamically spin coated on the perovskite layer at 1000 rpm for 30 s.

Before Cu evaporation 7 nm BCP were thermally evaporated at rate ~0.2Å through a shadow mask under base pressure ~10^{-6} mbar

3.3.5 Metallization and Encapsulation

To complete the perovskite devices 100 nm Al or Cu layers were thermally evaporated at rate ~2Å through a shadow mask under base pressure ~10^{-6} mbar forming an active area of 0.9 mm^2. Encapsulation was applied directly after evaporation in the glove box using a glass coverslip applying Ossila E131 encapsulation epoxy resin activated by 365 nm UV irradiation for 2 min.

3.4 Thin Film Characterization Techniques

3.4.1 Atomic Force Microscopy (AFM)

Atomic force microscopy (AFM) belongs to a general characterization technique called surface probe microscopy (SPM), with the first developed SPM being the surface tunneling microscopy (STM), and it is used to image the surface topography of various layers. The advantage of this technique compared to other imaging techniques is the high-resolution images that can be achieved especially along the z-axis where the resolution can be below 1 nm.

AFM, in common to STM, uses a sharped tip (tip curvature radius ~10 nm) to raster-scan the surface while a feedback loop controls the position of the tip for proper imaging of the surface. As shown in picture the feedback loop identifies and adjust the position

of tip using a laser beam which is deflected on the upper side of the cantilever and incidents on photodetector. Unlike STM it does not need a conductive surface since the tip and the surface come in very close contact (1 -10 nm) and measures interaction forces such as the coulomb and van der walls. Since no conductivity is needed AFM can be used to image the surface of insulating materials. Two main modes can be used to image the surface, the contact mode where the tip is on "direct" contact with the surface, or the tapping mode where an external oscillating electrical signal force the cantilever to vibrate in preset frequency. The tapping mode is in principles less destructive and is used to image soft materials. In the case of tapping mode additional information can be extracted such as the surface composition homogeneity by identifying changes in vibration frequency.

In this study, a Nanosurf easyScan 2 AFM (Figure 3.5) was used and the measurements were performed in tapping mode under ambient conditions, using a Tap 190Al-G silicon tips with aluminum reflex coating, resonance frequency of 190 kHz, force constant 48N/m and an average tip radius ≤ 10 nm. The tips were purchased form Budget Sensors Company.

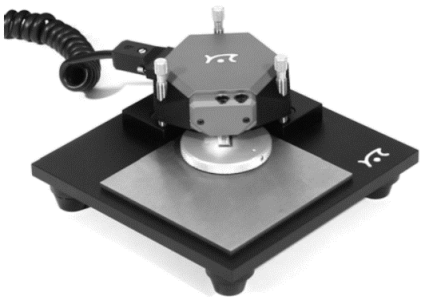

Figure 3.5 Picture of easyScan 2 AFM scan head on its sample stage

3.4.2 Profilometer

The thickness of the different films was measured using a DEKTAK 150 stylus profilometer from Veeco Company (Figure 3.6). The profilometer has a tip with tip curvature radius much larger than the AFM which attaches and scans mechanically the surface of the film. For this measurement the films were mechanically scratch, and the thickness was determined by the extracted profile at this region.

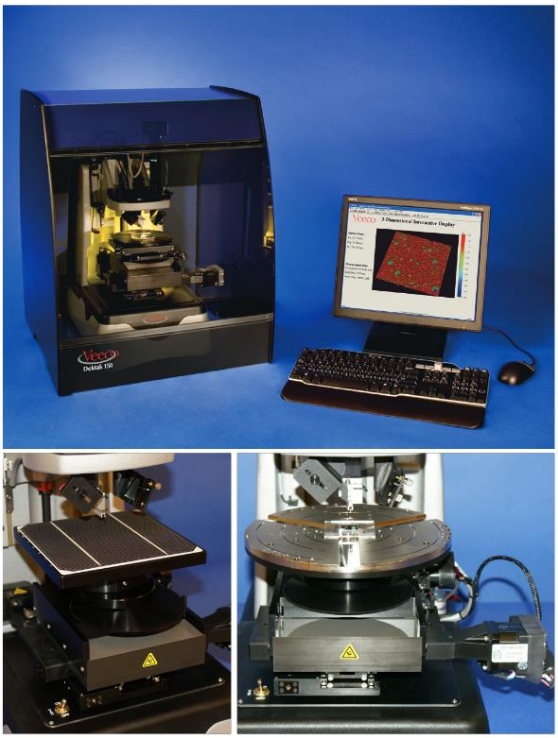

Figure 3.6 Pictures of DEKTAK 150 stylus profilometer (upper images), and of its moving sample stage (down images).

3.4.3 Ultraviolet - Visible Spectrophotometry (UV-Vis)

With UV-Vis is measured the absorption, transmittance and reflectance of various films. In this study, a Shimadzu UV-Visible Spectrophotometer UV-2600/2700

was used to record the transmittance and absorption spectrums of the different layers, where a Xe lamb were the excitation wavelength ranged from 800 – 350 nm using an integrated sphere. In this measurement the intensity of the light ($I_{(x)}$) in each wavelength is determined by a detector after the light interaction with the sample and compares it to the intensity of light before it passes through the sample ($I_{(0)}$). The interaction of the light with the sample as well as the determination of absorption coefficient was detailed descripted in chapter 2.2.3. Furthermore, the calculation of the optical band gap can be extracted from the Tauc plot which is extracted using equation (53).

Figure 3.7 Pictures of a Shimadzu UV-Visible Spectrophotometer UV-2600/2700

3.4.4 Photoluminance Spectroscopy (PL)

Photoluminance is the inverse process of the absorption which result in the emission of a photon with an energy defined by the difference of the conduction band edge and the valence band edge. The Radiative (band-to-band) recombination process was detailed descripted in chapter 2.2.4 while it is stressed that the trap assisted

recombination do not emit a photon. During the measurement the film is irradiated by a high intensity light with defined energy (higher than the energy band gap) inducing an excitation of electrons (photoexcitation) from the valance to conduction band. Then, during the band-to-band recombination of the excited carriers the intensity and the wavelength of the emitted light is recorder by a detector result in the PL spectra. In this thesis the PL measurement were performed with a Jasco FP-8300 Spectrofluorometer (Figure 3.8) in static mode, meaning that the recorded intensity for each wavelength is the integral of intensity for a defined time period.

Figure 3.8 Pictures of a Jasco FP-8300 Spectrofluorometer

3.4.5 Four Point Probe

The electrical resistivity (ρ) of the various films were measured using in-line four-point probe setup, which enables the evaluation of the sheet resistance ($R_{\square}$). The measurement is performed by two pairs of tip electrodes where the two outer electrons inject a current flow, and the two inner tips measure the resulted voltage across them (Figure 3.9).

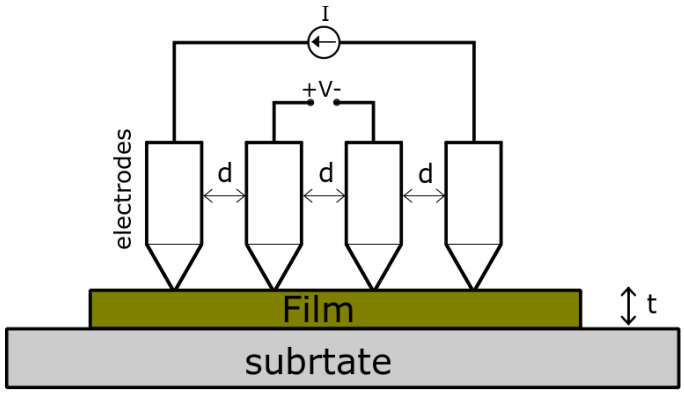

Figure 3.9 Schematic representation of four-point probe arrangement

Given that the distance between the electrodes is constant (*d*) and by knowing the thickness of the film (t) it can be calculated the electrical resistivity (ρ) by

$$\rho = R_{\square} t \quad (117)$$

The parameters that determine the electrical resistivity of a material was detailed descripted in chapter 2.2.2. In this Thesis four-point probe measurements were performed in Jandel RM3000 apparatus (Figure 3.10).

Figure 3.10 Pictures of a Jandel RM3000

3.4.6 Ultraviolet – X-ray Photoelectron Spectroscopy (UPS – XPS)

X-ray photoelectron spectra (XPS) and Ultraviolet Photoelectron Spectra (UPS) were recorded by using a Leybold EA-11 electron analyzer operating in constant energy mode at a pass energy of 100 eV and at a constant retard ratio of 4 eV for XPS and UPS, respectively. The spectrometer energy scale was calibrated by the Au $4f_{7/2}$ core level binding energy, BE, (84.0 ± 0.1 eV) and the energy scale of the UPS measurements was referenced to the Fermi level position of Au at a binding energy of 0 eV. All binding energies were referred to the C 1s peak at 284.8 eV of surface adventitious carbon. The X-ray source for all measurements was a non-monochromatized Al Kα line at 1486.6 eV (12 keV with 20 mA anode current). For UPS measurements, the He I (21.22 eV) excitation line was used. A negative bias of 12.22 V was applied to the samples during UPS measurements in order to separate secondary electrons originating from the sample and the spectrometer. The sample work function was determined by subtracting the high binding energy cut-off from the He I excitation energy (21.22 eV). The position of the high-energy cut-off was determined by the intersection of a linear fit of the high binding portion of the spectrum with the background. Similarly, the valence band maximum is determined with respect to the Fermi level, from the linear extrapolation of the valence band edge to the background.

3.4.7 Electro Impedance Spectroscopy (EIS)

Electro impedance spectroscopy (EIS) and Mott-Schottky (MS) measurements were performed using a Metrohm Autolab PGSTAT 302N, where for the EIS a red light-emitting diode (at 625 nm) was used as the light source calibrated to 100 mW cm^{-2}. For EIS a small AC perturbation of 20 mV was applied to the devices, and the different current output was measured throughout a frequency range of 1 MHz to 1 Hz. The steady state DC bias was kept at 0 V throughout the EIS experiments

3.5 Solar Cells Characterization Techniques

3.5.1 Current Density Vs Voltage (J-V)

The current density - voltage (J-V) and Voc – light intensity curves were obtained using a Botest LIV Functionality Test System measured with 10 mV voltage steps and 40 ms of delay time. For illuminated J-V curves, a calibrated Newport Solar simulator equipped with a Xe lamp was used, providing an AM1.5G spectrum at 100 mW cm^{-2} as measured by a certified oriel 91150 V calibration cell. A shadow mask (9 mm^2) was attached to each device prior to measurements to accurately define the corresponding device area. The modeling of the J-V and Voc – light intensity as well as the parameters that determine the shape of each curve were detailed descripted in chapter 2.2.6.

3.5.2 External Quantum Efficiency (EQE)

The current External Quantum Efficiency (EQE) spectra was obtained using a Newport System, Model 70356_70316NS. For illumination a calibrated Newport Solar simulator equipped with a Xe lamp attached to spectrometer was used. A shadow mask (9 mm^2) was attached to each device prior to measurements to accurately define the corresponding device area. The EQE analysis was detailed descripted in chapter 2.2.6.

4 Perovskite Solar Cells Using Undoped and 3% Cu – 2% Li Doped Spinel Nickel Cobaltite ($NiCo_2O_4$) HTL

4.1 Abstract

$NiCo_2O_4$ is a p-type semiconductor consisting of environmentally friendly, abundant elements with at least two orders of magnitude higher conductivity than NiO. It is demonstrated the use of combustion synthesized $NiCo_2O_4$ NP processed with blade coating as hole transport layer (HTL) in perovskite solar cells. Study of perovskite layers on different $NiCo_2O_4$ thickness as HTL reveals a difference hole extraction efficiency and for 15 nm optimized thickness enhanced hole extraction is achieved. As a result, p-i-n PVSCs with 15 nm $NiCo_2O_4$ HTLs and ~230 nm perovskite thickness showed a power conversion efficiency value in the range of 15.5 % with negligible hysteresis. Then, thicker layers of perovskite (~350) were applied to increase the photogeneration current but a reduction on the PCE of PVSC was observed. To overcome this issue a strategy of doping $NiCo_2O_4$ was applied. Specifically, solution combustion synthesized hole transport layer (HTL) of $NiCo_2O_4$ incorporating 3% Cu – 2% Li were fabricated using doctor-blading technique. PVSCs incorporating 3% Cu - 2% Li-doped $NiCo_2O_4$ (co-doped) shown an increase in Jsc (= 21.05 mA/cm^2) and Voc (=1.05 V) with delivered PCE of 16.5% compared to undoped $NiCo_2O_4$ (Jsc = 18.25 mA/cm^2, Voc = 0.88 V, PCE = 11.61 %). X-ray photoelectron spectroscopy

measurements revealed the tendency of Cu cations to replace preferably the surface Ni atoms changing the surface stoichiometry of $NiCo_2O_4$ inducing a cathodic polarization. Ultraviolet photoelectron spectroscopy measurements unveiled the increase of the ionization potential by 0.1 eV for co-doped $NiCo_2O_4$ film compared to unmodified $NiCo_2O_4$-based HTL. The enhanced PCE of inverted co-doped $NiCo_2O_4$ HTL based PVSCs is attributed to the improved hole extraction properties.

4.2 $NiCo_2O_4$ as HTL

4.2.1 Thin Film Fabrication and Characterization

The solution combustion synthesis of Spinel Nickel cobaltite $NiCo_2O_4$ was performed as it is described in section 3.3.2. XRD measurements (Figure 4.1 (a)) showed single face $NiCo_2O_4$ with the angular position of the diffraction peaks matching well with standard XRD pattern of cubic spinel $NiCo_2O_4$ with JCPDS card no 20–0781. The pattern of the material obtained after 200 °C heat treatment showed no diffraction peaks, indicating the formation of an amorphous structure. TEM images (Figure 4.1 (b)) of $NiCo_2O_4$ prepared at 250 ^oC material revealed that the material is composed of individual nanoparticles (NPs) with an average diameter of 4 ± 1.3 nm. High-resolution (HRTEM) image and selected area electron diffraction (SAED) (Figure 4.1 (c), (d)) also confirmed that $NiCo_2O_4$ NPs possess a single-phase spinel structure with high crystallinity since no impurity phase identified.

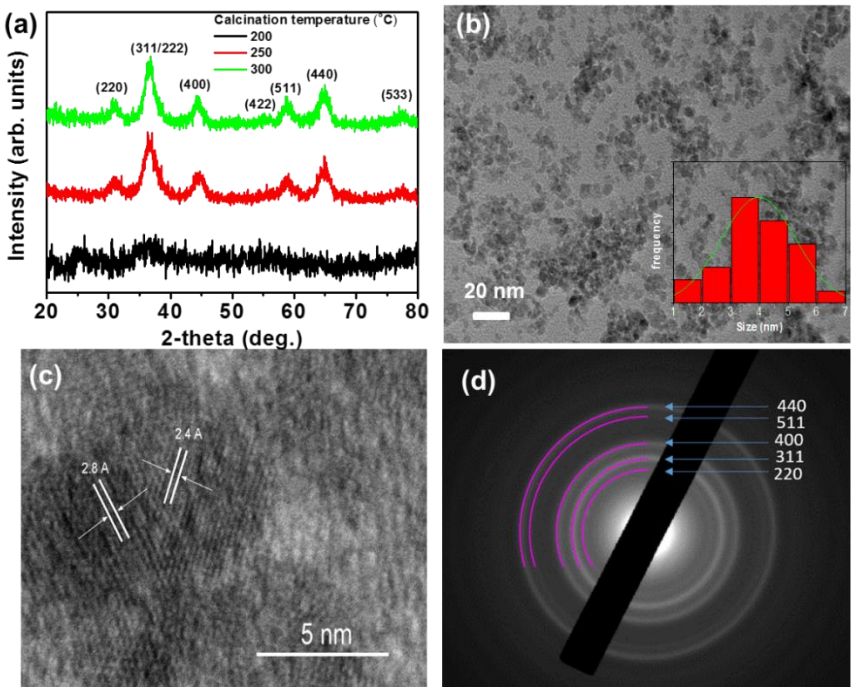

Figure 4.1 (a) XRD patterns of $NiCo_2O_4$ NPs at 200 ºC (black), 250 ºC (red), 300 ºC (green solid line) combustion temperatures. (b) Representative TEM image (inset: particle size distribution plot of the $NiCo_2O_4$ NPs at 250 ºC, showing an average diameter of 4 ± 1.3 nm), (c) high-resolution TEM and (d) SAED pattern of the as-synthesized $NiCo_2O_4$ NPs obtained at 250 ºC.

Thin films of $NiCo_2O_4$ NPs were produced on top of quartz and ITO substrates using the blade coating technique using 250 ^{O}C combustion temperature for 1 hour. Figure 4.2, demonstrates the surface topography of a 15 nm-thick film of $NiCo_2O_4$ NPs fabricated on top of glass/ITO and quartz substrates, as obtained by AFM line scans. On top of ITO substrate (Figure 4.2 (a)), the surface roughness is about 2.7 nm, while the film fabricated on quartz substrate (Figure 4.2 (b)), exhibits an impressively smooth and compact topography of only 0.56 nm roughness. The development of a low roughness layer is a beneficial feature for the photovoltaic performance since it enables us to grow perovskite top layers with low roughness and enhanced homogeneity. Moreover, the dense $NiCo_2O_4$ NPs-based thin film exhibits an increase electrical

conductivity up to 4 S/cm at room temperature, measured using four-point probe method.

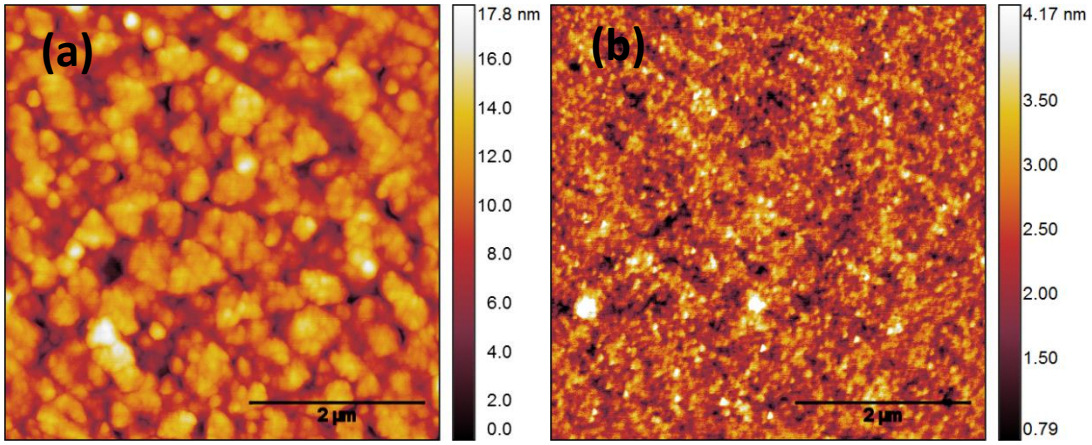

Figure 4.2 AFM images of (a) ITO/$NiCo_2O_4$ and (b) quartz/$NiCo_2O_4$ NPs thin films after combustion synthesis at 250 ºC (The scale bar is 2 µm).

Figure 4.3(a) (inset), shows the optical absorption spectrum of the $NiCo_2O_4$ NPs film fabricated on a quartz substrate and the corresponding Tauc plot (Figure 4a) for direct allowed transition [$(\alpha E)^2$ *versus* photon energy (E)], giving an optical band gap of 2.32 eV. $NiCo_2O_4$ NPs thin films of different thicknesses were also fabricated on glass/ITO substrate in order to investigate the transmittance of the front contact at UV-vis spectrum. Figure 4.3(b) displays the transparency of bare glass/ITO and $NiCo_2O_4$ NPs coated on glass/ITO substrate; it could be seen that $NiCo_2O_4$ films thinner than 20 nm reduce only slightly the transparency of the glass/ITO substrate for wavelengths longer than 450 nm, allowing intense light to reach the absorbing layer.

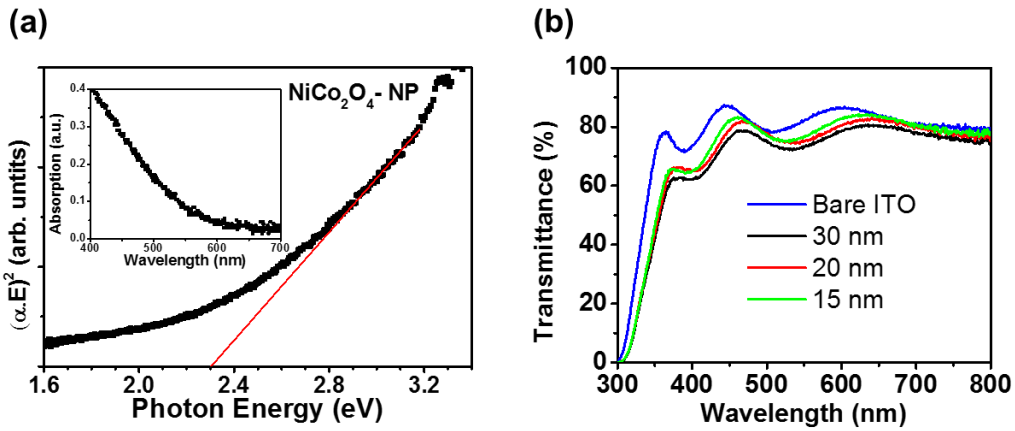

Figure 4.3 $(\alpha.E)^2$ vs. photon energy (E) plot, showing an energy band gap of 2.32 eV. Inset: UV-vis absorption spectrum of $NiCo_2O_4$ NPs film fabricated on quartz substrate. (b) Transmittance spectra of bare glass/ITO and $NiCo_2O_4$ NPs films deposited on glass/ITO substrate with thickness of 15, 20 and 30 nm.

4.2.2 Perovskite Solar Cells Fabrication and Characterization

Complete p-i-n architectures of PVSCs were fabricated employing $NiCo_2O_4$ NPs thin films with three different thicknesses, 30, 20 and 15 nm. On top of each $NiCo_2O_4$ layer, a 230 nm thick perovskite film was developed as described in Experimental section. The deposited perovskite film exhibits a low roughness of 5.4 nm (Figure 4.4(a)) and a mean grain size of 0.22 μm with a standard deviation of 0.051 μm (Figure 4.5), as calculated by AFM topography measurements.

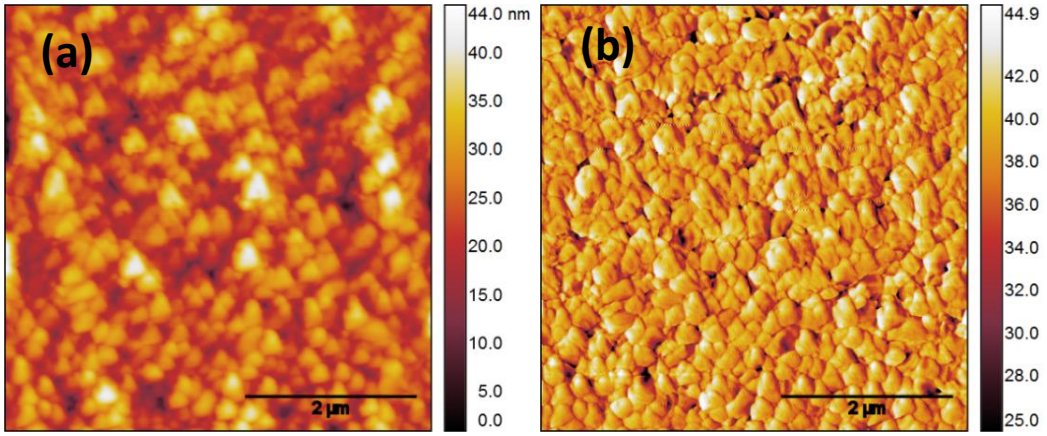

Figure 4.4 (a) Surface topography and (b) the corresponding phase image (5x5 µm) of 230 nm Perovskite film obtained by AFM.

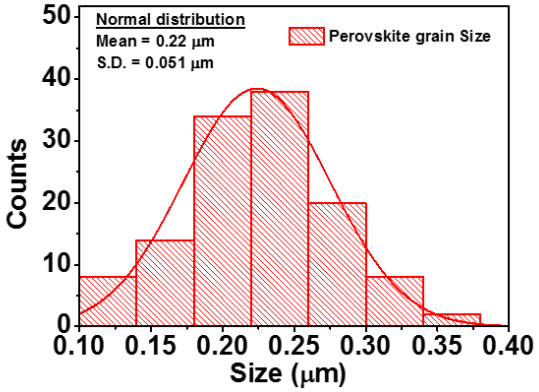

Figure 4.5 Size distribution of perovskite grains extracted from the AFM topography images. The mean size of the grains is 0.22 µm with a standard deviation of 0.051 µm.

To complete the devices, a $PC_{70}BM$ film was spun on each perovskite film serving as the electron transporting layer followed by a 100 nm thick thermally deposited Al layer (Figure 4.6(a)).

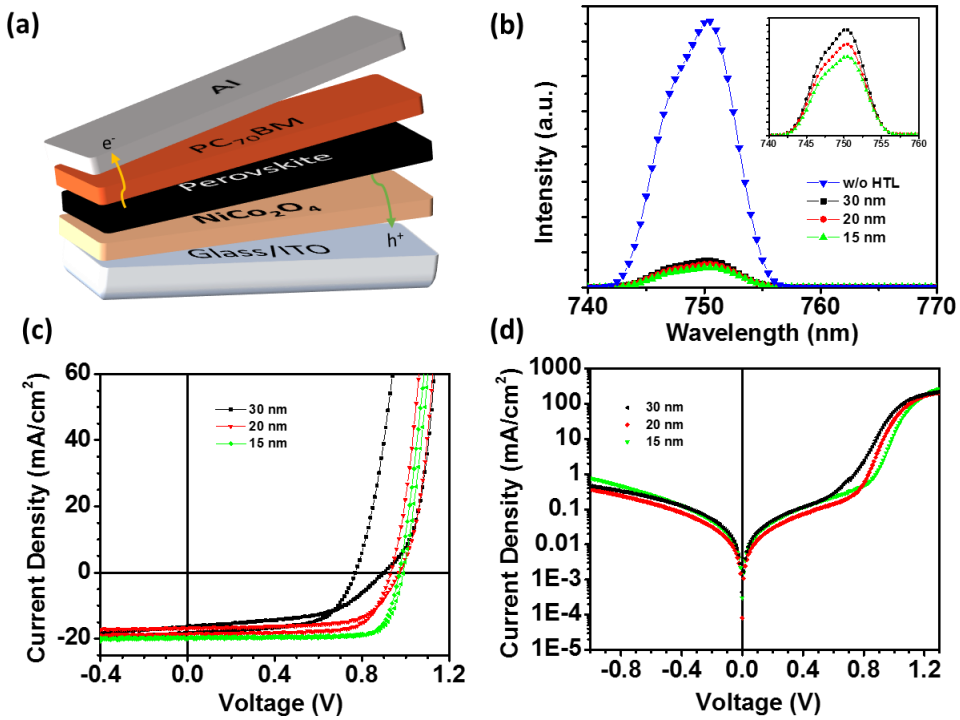

Figure 4.6 (a) The structure of the p-i-n perovskite solar cells under study (ITO/$NiCo_2O_4$-NPs/$CH_3NH_3PbI_3$/$PC_{70}BM$/Al). (b) Photoluminescence (PL) spectra (inset: magnification of the PL spectra at lower intensities), and current density versus voltage (J-V) plots (c) under 1 sun illumination and (d) under dark conditions of the ITO/$NiCo_2O_4$-NPs/$CH_3NH_3PbI_3$ devices fabricated with $NiCo_2O_4$ with different thickness (15 nm - green solid line, 20 nm - red line and 30 nm – black line).

Figure 4.6(c) depicts the characteristic current density – voltage curves (J – V under 1 sun simulated intensity) of the PVSCs fabricated with 15, 20 and 30 nm-thick $NiCo_2O_4$NPs layers, and the corresponding solar cell parameters are summarized in

Table 1, where the series resistance (Rs) were extracted from the dark J-V curves (Figure 4.6(d)).

Table 1 Extracted solar cell parameters from the J – V characterization of the ITO/$NiCo_2O_4$/$CH_3NH_3PbI_3$/$PC_{70}BM$/Al devices using $NiCo_2O_4$ NPs layers with different thickness.

$NiCo_2O_4$	Jsc [mA/cm^2]	Voc [V]	FF [%]	PCE [%]	Rs [Ωcm^2]
15 nm (forw.)	19.94	0.97	79.9	15.5	1.06
(rev.)	19.60	0.99	79.2	15.4	
20 nm (forw.)	18.47	0.93	73.2	12.6	1.34
(rev.)	16.83	0.97	67.8	11.1	
30 nm (forw.)	18.45	0.77	61.2	8.7	1.37
(rev.)	16.29	0.90	53.0	7.8	

It is observed that the J-V hysteresis on the forward and reverse sweep is reduced as the thickness of $NiCo_2O_4$ decreases from 30 to 15 nm, while both the Voc and fill factor (FF) increase. Concretely, for the reversed sweep the Voc was increased from 0.90 to 0.99 V and the FF from 53.0 to 79.9 %, while the hysteresis on the power conversion efficiency (PCE) for the 15 nm thick $NiCo_2O_4$ layer is negligible. On the other hand, the short circuit current (Jsc) showed the lowest increase (~ 8%) for a forward sweep from 18.47 to 19.94 mA/cm^2, compared to both Voc and FF. Consequently, the device consisting of a 15 nm thick $NiCo_2O_4$ film exhibits a PCE as high as 15.5 % for the forward sweep. The PCE of devices with thinner $NiCo_2O_4$ layers was declined (not shown here) exhibiting high leakage current due to not fully covered

ITO. Figure 4.7 demonstrates the external quantum efficiency (EQE) measurements of the corresponding devices. It is noticed that for 15 nm thick $NiCo_2O_4$ film the overall efficiency is increased comparing to thicker layers due to higher transmittance as well as to better charge extraction, as it will be shown below. All the devices show a declined photo response at longer wavelength (600 - 750 nm) which can be ascribed to the relatively thin perovskite layer (230 nm) and to not optimized back contact interface (Perovskite/$PC_{70}BM$/Al).

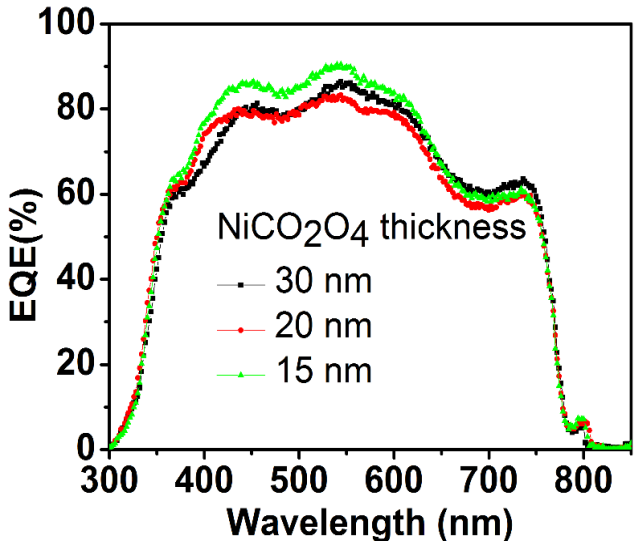

Figure 4.7 External Quantum Efficiency (EQE) of ITO/$NiCo_2O_4$-NPs/$CH_3NH_3PbI_3$ devices fabricated with $NiCo_2O_4$ with different thickness (15 nm - green solid line, 20 nm - red line and 30 nm – black line).

The impact of the $NiCo_2O_4$ layer thickness on the ITO/$NiCo_2O_4$-NPs/perovskite device performance was evaluated by photoluminescence (PL) spectroscopy (see Figure 4.6(b)). Comparing to a PVSC structure without HTL, the PL signal of the devices with $NiCo_2O_4$ HTL show a quenching of more than 90 %, indicating a great reduction in band-to-band charge recombination and, thus, a better hole selectivity of

the ITO electrode covered by $NiCo_2O_4$. Further, the PL intensity is lower in 15 nm-$NiCo_2O_4$ film than that of the thicker films, pointing to an efficient suppression of the electron-hole recombination (Figure 4.6(b), inset).

To further understand the charge recombination processes during the hole transfer from perovskite to $NiCo_2O_4$ layer, we performed electrochemical impedance spectroscopy (EIS) measurements under solar light and zero bias. Figure 4.8(a) shows the characteristic Nyquist plots of the three corresponding devices for 15, 20 and 30 nm sized $NiCo_2O_4$ films. The results showed a shape of two frequency responses for PVSCs, where the second semicircle (feature at low frequencies) is been attributed to the recombination resistance (Rrec).[123,124] As the $NiCo_2O_4$ film thickness is reduced the radius of the semicircle increases, which implies a higher resistance in the charge recombination, in agreement with the findings from PL measurements. Figure 4.8(b) presents the Mott-Schottky (M-S) plots of the devices when sweeping from higher to a lower voltage. The crossing of the curves at $1/C^2 = 0$ is attributed to the flat band potential of the device, while the lower slope of the linear region is ascribed to the charge accumulation at the interfaces, which impedes an efficient extraction of the charge carriers.[125] The M-S slope for the thicker film is lower implying that this layer cannot extract fast enough the charge carriers, inducing their accumulation at the interface. This behavior causes a higher hysteresis, which in turn increase electron-hole recombination (due to high spatial density) and leads to the drop of the flat band potential. On contrary, the thinner layer seems to extract faster the charge carriers, increasing the flat band potential, and thus the Voc, as well as the FF of the corresponding device. The direct correlation of faster charge carriers extraction at thinner HTL layers with increased FF has been previously studied by M.Stolterfoht *et.*

al.[126] We also notice that the configuration of 15 nm $NiCo_2O_4$ thin layer is depleted faster than the other devices due to enhanced charge carrier extraction, which can also affirm the increase at the FF of the corresponding PVSC. The increased Jsc for the 15 nm $NiCo_2O_4$ layer can be ascribed to the higher transparency of the film (shown above) and thus higher photogeneration of electron-hole pairs as well as to the lower series resistance as shown in Table 1.

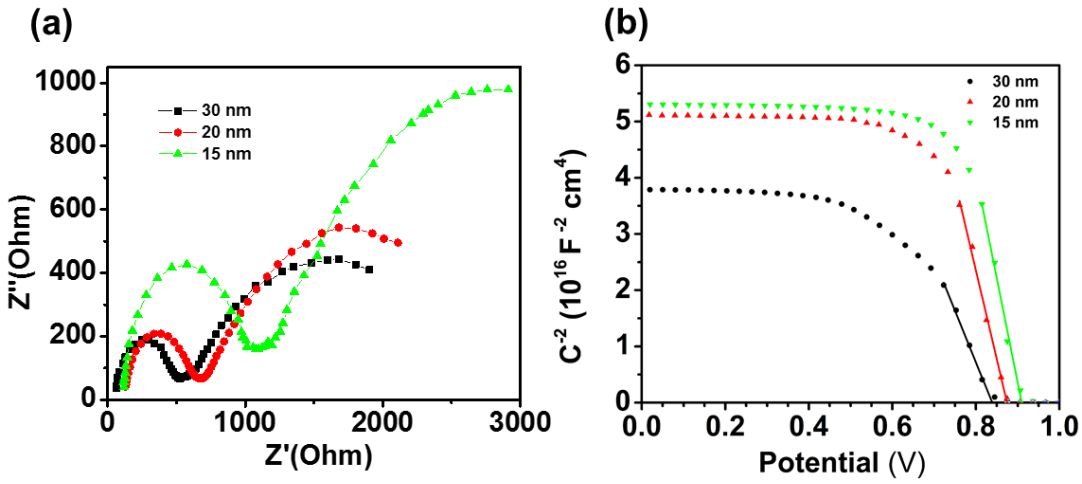

Figure 4.8 (a) Nyquist and (b) Mott-Schottky plots for the PVSK devices with 15, 20 and 30 nm thickness of the $NiCo_2O_4$ HTL.

4.3 3% Cu - 2% Li co-doped $NiCo_2O_4$ as HTL

4.3.1 Perovskite Solar Cells Fabrication and Characterization

To increase PVSC's PCE the perovskite layer was increased to ~350 nm to enhance light absorption and thus increase photogenerated carriers which accumulate at the perovskite/HTL interface (accumulation zone) and subsequently collected by the

contact.[127] Thus, solution combustion synthesized $NiCo_2O_4$ HTL prepared with different doping to enhance the collection efficient of the increased photogenerated carriers.

The PVSCs under investigation were prepared using 15 nm undoped and doped $CoNi_2O_4$ HTL as described in sections 3.3.2 applying 250 ^oC combustion temperature and for 1 hour and 350 nm thick perovskite film as described in sections 3.3.3. Figure 4.9(b) demonstrates the current density - voltage (J – V) measurements under 1 sun simulated illumination for the PVSCs using $NiCo_2O_4$ with different doping types and the extracted photovoltaic parameters are shown in Table 2.

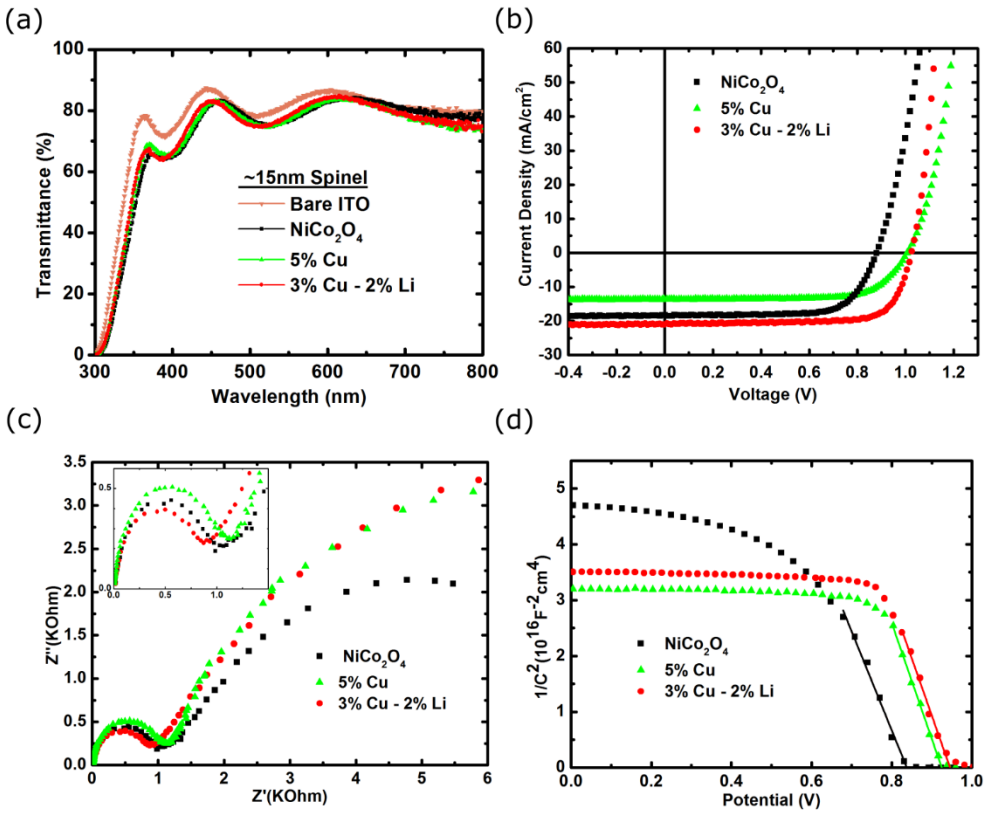

Figure 4.9 (a) Transmittance measurements of bare glass/ITO and different type of doped 15 nm $NiCo_2O_4$ fabricated on glass/ITO substrates. (b) J-V curves, (c) Nyquist (inset: zoom-in at the high frequency region) and (d) Mott-Schottky plots of PVSC using 15 nm undoped, 5% Cu and 3% Cu – 2% Li doped $NiCo_2O_4$ HTL.

Pristine $NiCo_2O_4$ HTL based PVSCs shows a considerably lower Voc (0.88 V), but higher Jsc (18.25 mA/cm^2) compared to 5% Cu-doped $NiCo_2O_4$ HTL based PVSCs (Voc = 1.03 V, Jsc = 14.89 mA/cm^2), while FF is almost similar (72.3 % and 73 %), delivering a PCE of 11.61% and 11.02%, respectively. Importantly, PVSCs incorporating 3% Cu – 2% Li $NiCo_2O_4$ HTL exhibits both higher Voc (1.05 V) and Jsc (21.05 mA/cm^2) as well as a slightly higher FF (74.8 %) compared to previous devices, delivering a PCE of 16.54 %.

Table 2 J -V extracted parameters of PVSC using 15 nm undoped, 5% Cu and 3% Cu – 2% Li $NiCo_2O_4$ as HTL

HTL	Voc (V)	Jsc (mA/cm^2)	FF (%)	PCE (%)
$NiCo_2O_4$	0.88	18.25	72.3	11.61
5% Cu	1.03	14.89	73	11.02
3 % Cu - 2 % Li	1.05	21.05	74.8	16.54

In order to investigate the reduced photocurrent of 5% Cu-doped $NiCo_2O_4$, we first excluded any possible optical losses induced by the doping. Figure 4.9(a) demonstrates the transmittance of ~15 nm thick $NiCo_2O_4$ layer on glass/ITO. It is obvious that the difference on transmittance is negligible for all films under study, where the extracted Tauc-plot (Figure 4.10) for direct transitions show similar optical band gaps (Eg).

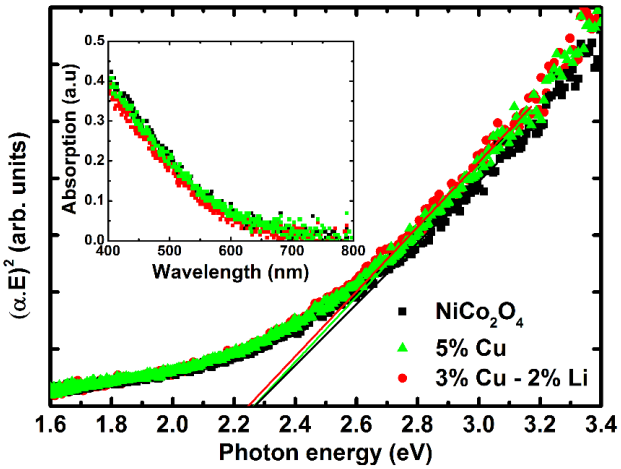

Figure 4.10 Tauc-plot of undoped (black rectangles), 5% Cu (green triangles) and 3% Cu – 2% Li (red circles) $NiCo_2O_4$ films. The inset shows the absorption measurements of the corresponding films.

Further, the similar morphology in all types of $NiCo_2O_4$ films was confirmed excluding, also, differences in electrical losses related to films quality (e.g., shunting current). Figure 4.11 and Figure 4.12 illustrates the AFM topography images of (a) 5% Cu and (b) 3% Cu -2% Li $NiCo_2O_4$ films fabricated on quartz and glass/ITO substrates, while Figure 4.12(c) illustrates the topography of the ITO. In both cases the films exhibit similar roughness between them (0.7 - 0.8 nm for quartz and 2.9 - 3.0 nm for glass/ITO substrate) comparable to the ones measured for the pristine $NiCo_2O_4$ films, affirming the similar quality of different types of $NiCo_2O_4$ films.[128]

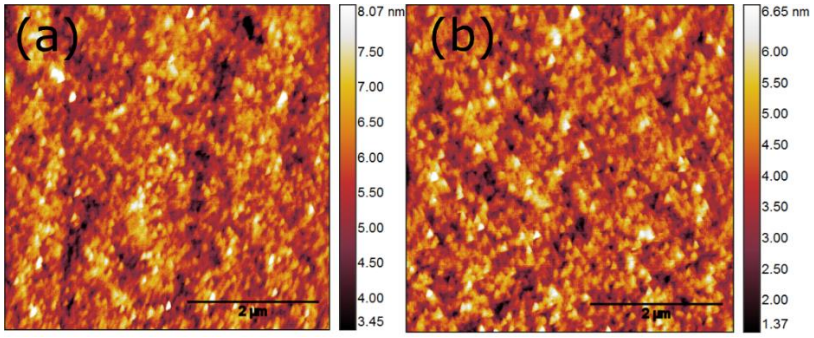

Figure 4.11 AFM topography images of (a) 5% Cu (b) 2% Li- 3% Cu doped $NiCo_2O_4$ films, respectively, fabricated on quartz substrate. The films exhibit a roughness of (a) 0.7, (b) 0.8 nm.

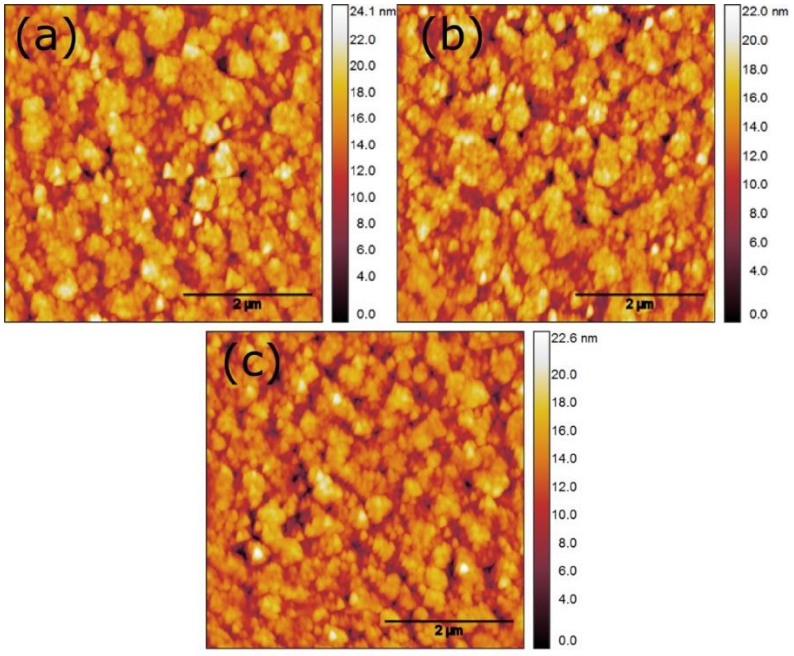

Figure 4.12 AFM topography images of (a) 5% Cu and (b) 3% Cu - 2% Li doped $NiCo_2O_4$ films, respectively, fabricated on (c) glass/ITO substrate. The films exhibit similar roughness (a) 2.9, (b) 3.0 and (c) 2.8 nm.

Thus, electrical characterization of PVSC were performed using Electro impedance spectroscopy (EIS) measurements under illumination and zero bias on the previous described PVSCs configurations. As it is observed at Figure 4.12(c) all the spectra show the characteristic two frequency response, where the first arc (higher

frequencies) is ascribed to charge transfer resistance (R_{ct}) while the second larger arc (lower frequencies) at the charge carrier recombination resistance (R_{rec}).[129,130] PVSC incorporating 3% Cu – 2% Li $NiCo_2O_4$-HTL exhibits higher R_{rec} compare to unmodified $NiCo_2O_4$-HTL based PVSCs, while shows lower R_{ct} [Figure 4.12(c), inset)] compare to both unmodified and 5% Cu-doped $NiCo_2O_4$-HTL based PVSCs due to higher electrical conductivity of the 3% Cu – 2% Li $NiCo_2O_4$ layer, as it was also confirmed by four point probe conductivity measurements summarized in Table 3. Jung-Hee Kim *et. al.* have also reported increase in the electrical conductivity of spinel nickel cobaltite by introduction of Li.[131]

Table 3 Room-temperature four-point probe extracted values of undoped $NiCo_2O_4$ and 5% Cu and 3% Cu – 2% Li doped $NiCo_2O_4$ films.

$NiCo_2O_4$	Conductivity (S/cm)
undoped	4.00
5% Cu	1.87
3% Cu - 2% Li	4.85

Additional Mott-Schottky (Figure 4.12(d)) measurements were carried out on devices sweeping from higher to lower voltage under dark conditions. The crossing of the curves at $1/C^2 = 0$ is attributed to the flat band potential of the device.[125,132] 5% Cu and 3% Cu – 2% Li $NiCo_2O_4$ -HTL based PVSCs show a higher built-in potential compare to unmodified $NiCo_2O_4$-HTL based PVSCs which is consistent with the increased Voc value achieved for the 5% Cu and 3% Cu – 2% Li NiCo2O4 -HTL based PVSCs.

Further investigation of the charge carrier recombination dynamics was conducted to elucidate the enhanced device performance of 3% Cu – 2% Li doped

compared to undoped $NiCo_2O_4$-HTL based PVSCs. We first exclude any difference on the perovskite film morphology. AFM topography images (Figure 4.13) of perovskite surface revealed similar surface roughness (12.5 ± 0.4 nm) and grain sizes (ca. 110-123 nm) as shown in picture Figure 4.14, indicating that PVSCs under study comprise similar morphology within the active layer.

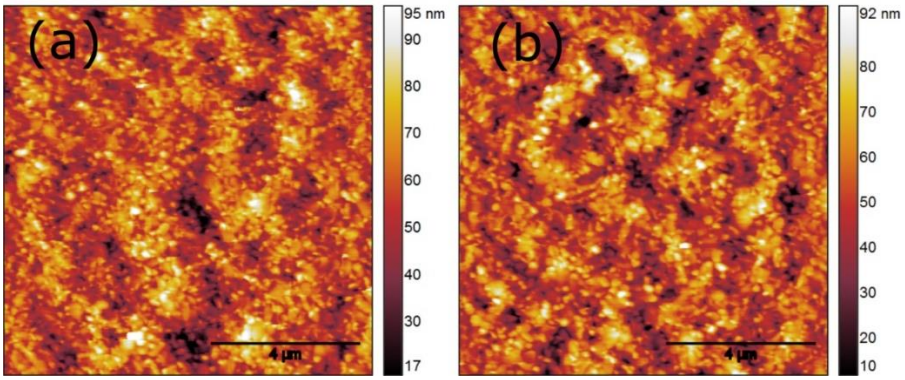

Figure 4.13 AFM topography images (10x10 µm) of perovskite active layers on (a) undoped and (b) 3% Cu – 2 % Li doped $NiCo_2O_4$ 350 nm thick perovskite.

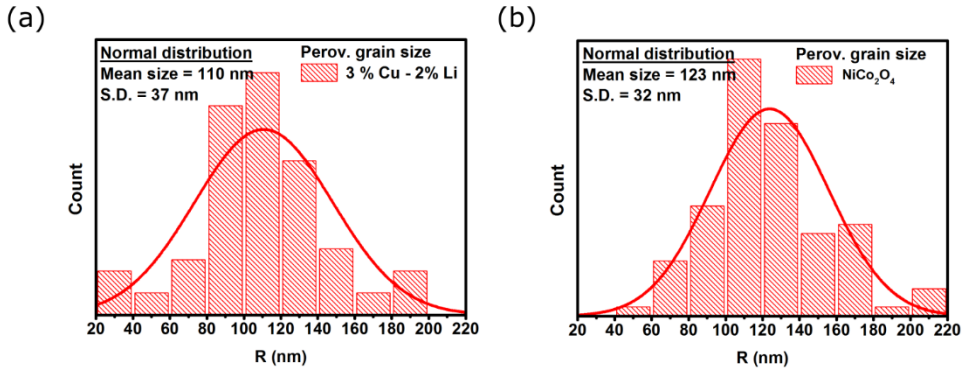

Figure 4.14 Distribution of perovskite grain size and the extracted parameters of mean value and standard deviation using normal distribution fit curves for perovskite films on undoped and 3% Cu – 2 % Li doped $NiCo_2O_4$, for 350 nm thick perovskite

Moreover, Voc - light intensity measurements were performed to investigate the recombination mechanism within PVSCs under study. According to simplified Shockley Reed Hall recombination model, the slope between logarithmic light intensity and Voc must be equal to 2kT/q for trap-assisted and kT/q for trap-free recombination.[133–137] As shown in Figure 4.15 (a), the Voc - light intensity curves scale equal to kT/q, implying that a trap-free recombination mechanism is dominant for all the PVSCs. Thus, steady state photoluminescence (PL) measurements (Figure 4.15(b)) are adequate to evaluate the degree of charge recombination at each configuration. The PL intensity for undoped $NiCo_2O_4$-HTL is much higher compared to 3% Cu – 2% Li $NiCo_2O_4$-HTL, implying that a much higher number of electron-hole pairs recombine for the case of the undoped HTL justifying the lower PCE of the corresponding undoped NiCo2O4-HTL based PVSCs. The experimental results presented indicate that 3% Cu – 2% Li $NiCo_2O_4$ HTL transfers and collects hole charges more efficient than the undoped $NiCo_2O_4$ HTL.

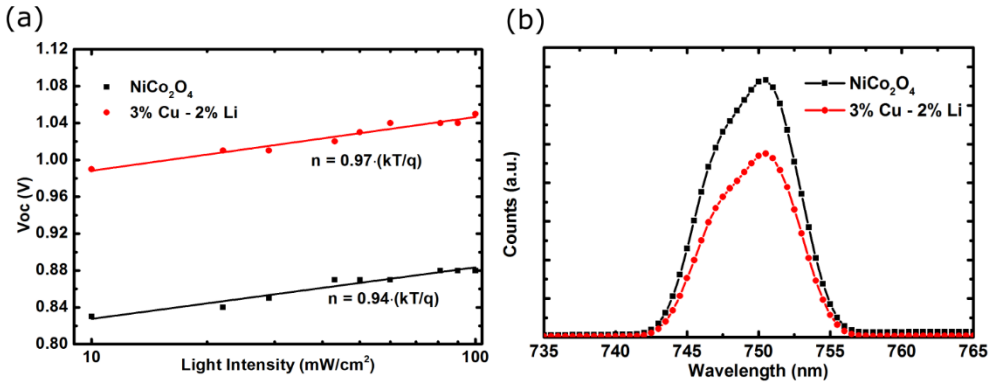

Figure 4.15 (a) Voc – light intensity measurements of PVSC using 15 nm-sized undoped and 3% Cu – 2 % Li HTL. (b) Steady-state room temperature photoluminescence (PL) spectra of 350 nm thick perovskite films fabricated on 15 nm unmodified and 3% Cu – 2 % Li co-doped $NiCo_2O_4$ on glass/ITO substrate.

4.3.2 XPS - UPS on Undoped and Doped $NiCo_2O_4$ Films

A deeper material properties investigation was performed to better understand the origin of the enhanced hole collection properties for 3% Cu – 2% Li $NiCo_2O_4$-HTLs. Structural characterization with X-ray diffraction (XRD) on the corresponding $NiCo_2O_4$ samples (Figure 4.16) matched the cubic face-centered lattice structure for all types of $NiCo_2O_4$ (PDF#20-0781), implying single-crystalline structure.

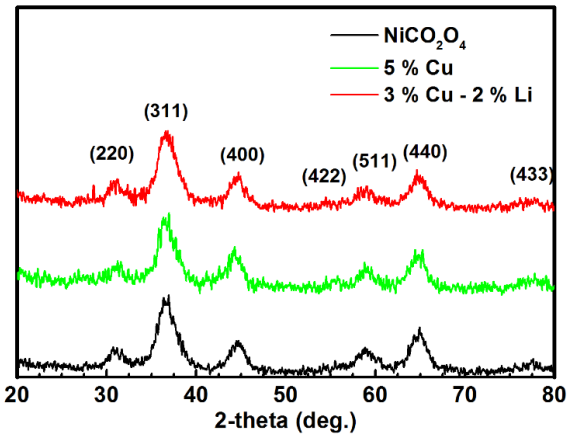

Figure 4.16 X-ray diffraction (XRD) patterns of undoped, 5% Cu doped $NiCo_2O_4$ and 3% Cu – 2% Li co-doped $NiCo_2O_4$ powder.

X-ray photoelectron spectroscopy (XPS) measurements were also performed on doped and un-doped $NiCo_2O_4$ HTLs. The Co 2p spectrum (Figure 4.17) was best fitted by using two spin-orbit doublets for the tetrahedral Co^{+2} and octahedral Co^{+3} oxidation states and with two shake-up satellites located at the higher binding energy (BE) side of the main peaks. The peak located around 779.7 eV can be attributed to the octahedral

Co^{+3} observed in Co_3O_4,[138] while the higher binging energy peak around 780.9 eV can be assigned to the tetrahedral Co^{+2} similar to CoO.[139] The spectrum of the Ni $2p_{3/2}$ region was fitted using three components (Figure 4.18). The peak at 854.3 eV corresponds to Ni^{+2} ions, while that at 856.0 eV is attributed to Ni^{+3}. [138,140] The shake-up satellite at around 861.8 eV was fitted considering one broad line.

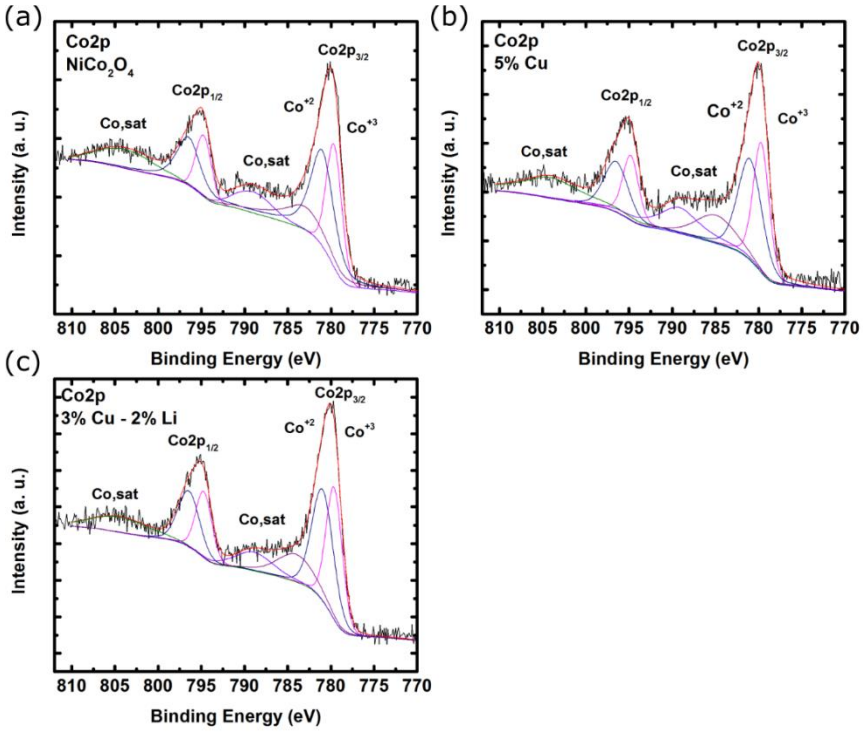

Figure 4.17 XPS spectra of the Co2p for (a) undoped, (b) 5% Cu doped $NiCo_2O_4$, (c) 3% Cu – 2 % Li co-doped $NiCo_2O_4$ films.

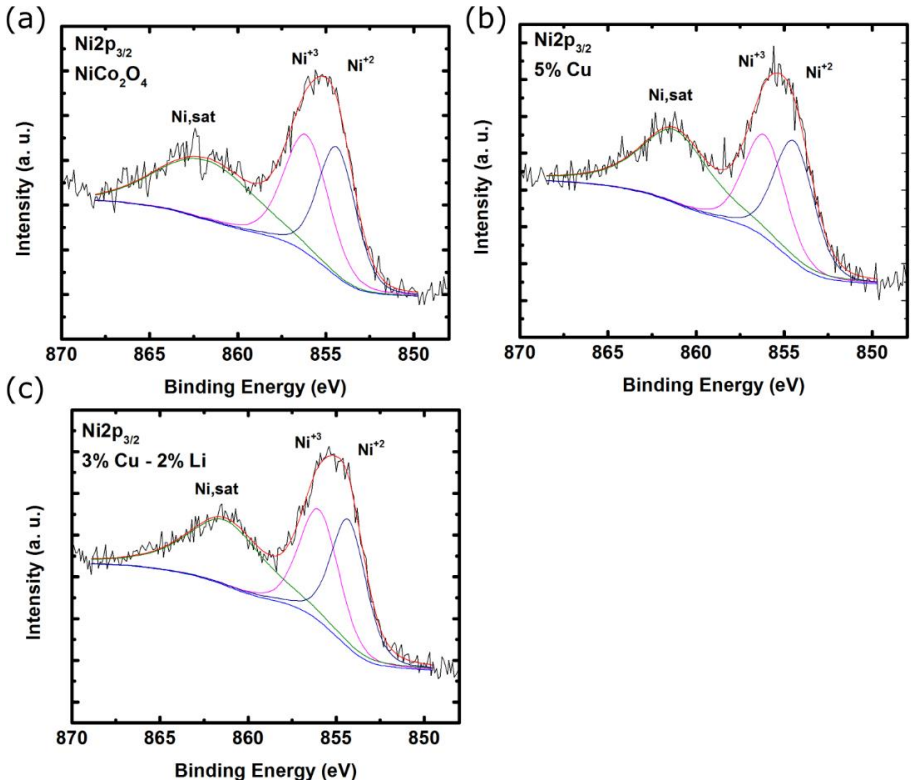

Figure 4.18 XPS spectra of the Ni2p$_{3/2}$ for (a) undoped, (b) 5% Cu doped $NiCo_2O_4$ (c) 3% Cu – 2 % Li co-doped $NiCo_2O_4$ films

For Cu doped films the Cu 2p spectra were recoded and are displayed in Figure 4.19. The Cu 2p doublet is well resolved. The Cu 2p3/2 peak at 934.6 eV and the satellite at higher binding energies indicate that Cu is oxidized and can be identified as Cu^{+2} ions in octahedral coordination.[140–142] The intensity of Cu 2p3/2 peak for the 3% Cu -2% Li $NiCo_2O_4$ is low and the satellite structure is not resolved. Nevertheless, the peak is located at BEs around 934.6 eV, thus even for lower concentration of Cu there are Cu^{+2} ions.

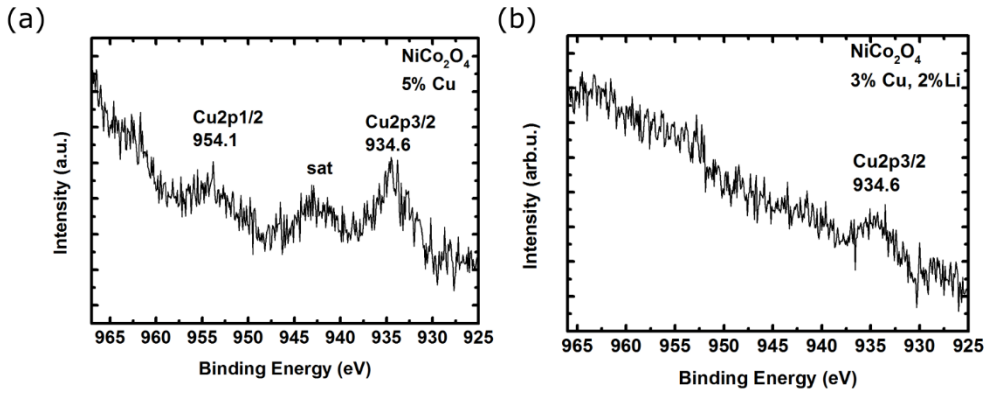

Figure 4.19 XPS spectra of the Cu2p for (a) 5% Cu doped $NiCo_2O_4$ (b) 3% Cu – 2 % Li co-doped $NiCo_2O_4$ films.

Table 4 summarizes the Ni:Co atomic ratio values obtained from the processing of the reported XPS spectra. The surface sensitivity of XPS and material precursor stoichiometry reveals that a small excess of Ni ions is identified at the surface of the un-doped $NiCo_2O_4$ as the XPS calculated Ni:Co ratio is 0.55. For 5% Cu doped and 3% Cu -2% Li co-doped $NiCo_2O_4$ a decrease at Ni:Co ratio confirms the deficiency of Ni ion at the surface, resulting in 0.43 and 0.45 ratios, respectively, which have been preferentially replaced by the Cu ions. These findings agree with previous reported results of A.C. Tavaresa *et al.*[142] where the introduction of Cu replace surface Ni ions at the $NiCo_2O_4$ electrodes, which indeed induces a similar effect to cathodic polarization (downshift of the energy bands).

Table 4 Nickel to cobalt (Ni:Co) ratio extracted by XPS analysis of undoped, 5% Cu, and 3% Cu – 2% Li co-doped $NiCo_2O_4$ samples.

Ratio	$NiCo_2O_4$	5 % Cu	3 % Cu -2 % Li
Ni:Co	0.55	0.43	0.45

Additional ultraviolet photoelectron spectroscopy (UPS) measurements were performed on doped and undoped $NiCo_2O_4$ films to determine the energy levels. Figure 4.20 (b) displays the UPS spectra of the valence band region near the Fermi level. The valence band maximum (VBM) for the $NiCo_2O_4$ was found at 0.2 eV bellow the Fermi level, while it is shifted to higher binding energies (~0.3 eV) when the $NiCo_2O_4$ is doped with 5% Cu and 3% Cu-2% Li. Figure 4.20 (a) shows the high binding energy region of UPS spectra, where the high energy cut-off region is used to determine the work function (Φ) of the interface. Φ for all films of $NiCo_2O_4$ was found at 5.1 eV and the ionization potential was calculated by adding the values of Φ and VBM. Thus, ionization potentials were found to be ~5.3 eV for the undoped $NiCo_2O_4$ and ~5.4 eV for 5% Cu and 3% Cu-2% Li doped $NiCo_2O_4$ HTLs, matching better with the VBM of perovskite. A schematic representation of PVSC energy band levels applying different types of $NiCo_2O_4$ layers is illustrated in Figure 4.20 (c) where the calculated values from the UPS and the E_g (~2.3 eV) from UV-Vis optical absorption spectra were utilized.

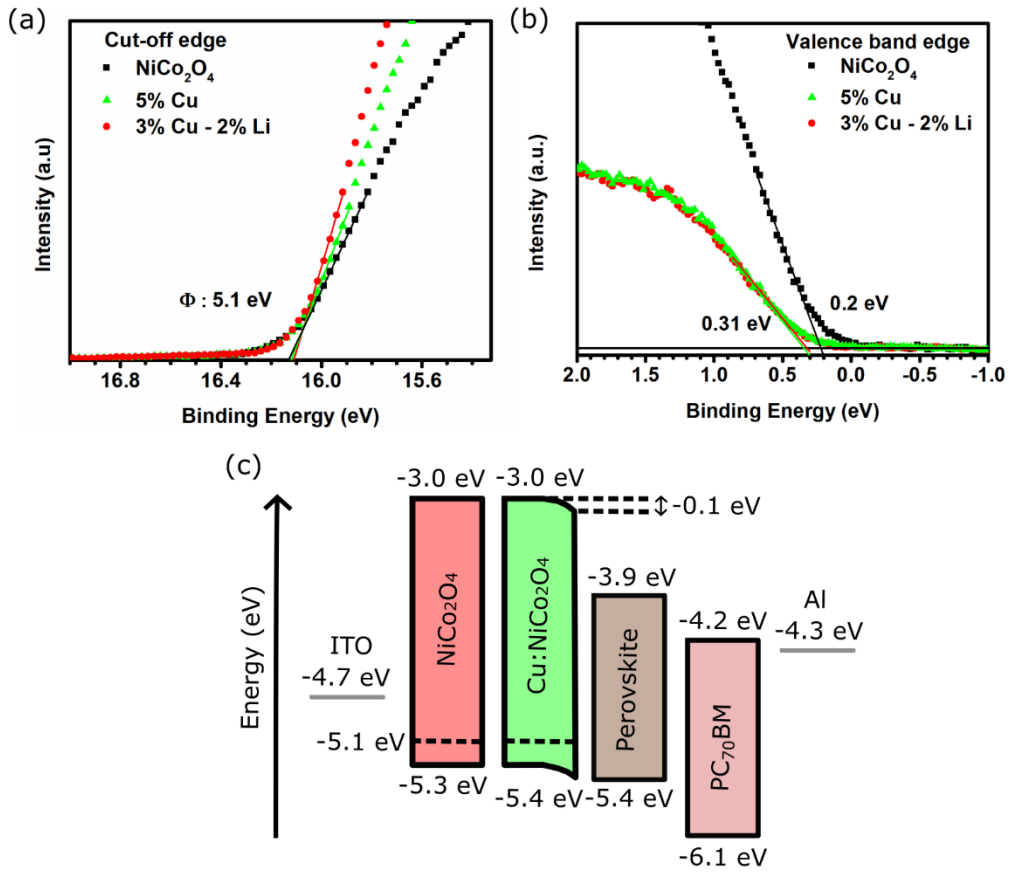

Figure 4.20 (a) The high binding energy region and (b) valance band region near the Fermi level of the UPS spectra for undoped, 5% Cu and 3% Cu – 2% Li co-doped $NiCo_2O_4$ HTLs. (c) Schematic representation of energy band levels of the corresponding perovskite solar cells incorporating 5% Cu and 3% Cu – 2% Li doped $NiCo_2O_4$ (green bar) and undoped $NiCo_2O_4$ HTLs (red bar). In the case of the doped $NiCo_2O_4$ the band bending represents the similar effect to cathodic polarization at the surface region of $NiCo_2O_4$ film induced by the doping.

4.4 Summary

In summary, solution combustion synthesized compact films of p-type $NiCo_2O_4$ NPs (~4 nm) using doctor blade technique were successfully developed and applied for the fabrication of PVSC. XRD, EDS and electron microscopy measurements confirm the crystallinity of $NiCo_2O_4$, while compact films using blade coating, which is a large-

scale compatible technique, were fabricated exhibiting high electrical conductivity (~4 $S.cm^{-1}$) and very low roughness (0.56 nm). The impact of $NiCo_2O_4$ film thickness on PVSCs (~230 nm thick perovskite) characteristics was investigated, where for ~15 nm optimum thickness enhanced charge extraction and negligible J-V hysteresis, compared to thicker films, was shown delivering a PCE of 15.5 %. Thereafter, co-doped $NiCo_2O_4$ with 5% Cu and 3% Cu – 2% Li where fabricated to increase the PCE of PVSC incorporating thicker perovskite layer (350 nm). 5% Cu doping increase the Voc of the corresponding PVSC but decrease the Jsc compared to undoped $NiCo_2O_4$ PVSC due to lower electrical conductivity. To overcome this effect 3% Cu – 2% Li co-doping was applied on solution combustion synthesized NiCo2O4-HTLinducing an increase on electrical conductivity resulting in inverted PVSCs with lower charge transfer resistance compared to 5% Cu doped $NiCo_2O_4$ -HTL based PVSCs and higher charge recombination resistance compared to undoped $NiCo_2O_4$-HTL based PVSCs. Mott Schottky measurements showed the higher built-in potential of the Cu doped NiCo2O4 PVSC while PL studies confirmed the better hole extraction of 3% Cu – 2% Li $NiCo_2O_4$-HTL/perovskite active layer interface. Further investigation for the origin of this enhancement was performed by XPS measurements on the co-doped and undoped $NiCo_2O_4$ revealing the tendency of Cu ions to replace preferably the surface Ni ions of NiCo2O4 changing the surface stoichiometry of Ni/Co which induces a cathodic polarization effect. UPS measurements reveled the increase of the ionization potential by 0.1 eV for the 3% Cu – 2% Li $NiCo_2O_4$ HTLs compared to undoped NiCo2O4-HTL a parameter which improves hole carrier extraction properties for the 3% Cu – 2% Li $NiCo_2O_4$-HTL based PVSCs reported. As a result, inverted PVSCs containing ~350 nm

thick perovskite and 3% Cu – 2% Li co-doped $NiCo_2O_4$ HTL shown an increased PCE of 16.54% compared to undoped $NiCo_2O_4$ HTL based PVSCs with PCE of 11.61%.

5 Thermal Analysis of Metal-Organic Precursors for Functional Cu:NiOx Hole Transporting Layer in Inverted Perovskite Solar Cells: Role of Solution Combustion Chemistry in Cu:NiOx Thin Films Processing

5.1 Abstract

Low temperature solution combustion synthesis emerges as a facile method for synthesis of functional metal oxides thin films for electronic applications. We study the solution combustion synthesis process of Cu:NiO_x using different molar ratios (w/o, 0.1 and 1.5) of fuel acetylacetone (Acac) to oxidizer (Cu, Ni Nitrates) as a function of thermal annealing temperatures 150, 200 and 300 ^oC. The solution combustion synthesis process, in both thin films and bulk Cu:NiO_x, is investigated. Thermal analysis studies reveal that the Cu:NiO_x thin films show a more gradual mass loss while the bulk Cu:NiO_x exhibits a distinct combustion process. The thin films can crystallize to Cu:NiO_x at annealing temperature of 300 ^oC irrespective to the Acac concentration whereas lower annealing temperatures (150 and 200 ^oC) produce amorphous materials

with the remnants. Finally, 50 nm Cu:NiO_x thin films are introduced as HTLs within the inverted perovskite solar cell device architecture. The Cu:NiO_x HTL annealed at 150 and 200 ^oC provided PVSCs with limited functionality whereas efficient triple-cation $Cs_{0.04}(MA_{0.17}FA_{0.83})_{0.96}Pb(I_{0.83}Br_{0.17})_3$ based PVSCs achieved for Cu:NiO_x HTLs annealed at temperature 300 ^oC

5.2 Results

5.2.1 TGA results of Cu:NiO_x (films versus bulk precursors)

The synthesis behavior of the Cu:NiO_x thin films and corresponding bulk mixtures onto alumina disc substrates was examined through thermogravimetric analysis (TGA) and differential thermal analysis (DTA). Figure 5.1(a) and Figure 5.1 (b) present the TGA and the corresponding DTA curves of the 50 nm thick Cu:NiO_x films prepared with different molar ratio of fuel (Acac) to oxidizer (Cu and Ni nitrates), namely without (w/o) Acac, 0.1 and 1.5, and drying the films at 80 ^oC. The Cu:NiO_x film w/o Acac shows a mass loss near ~130 °C, indicating the thermal instability of this precursor in the absence of any fuel additive. For the Cu:NiO_x films prepared with 0.1 and 1.5 Acac/oxidizer molar ratio, the TGA profiles show similar thermal decomposition behavior, exhibiting a gradual mass loss after $T>T_{ig}$. This is not consistent with a combustion process that occurs to the combustible precursors as will be shown below. Near 300 °C, the TGA profiles for all samples display an intense mass

loss, which is associated with an exothermic peak on the DTA curve. This is attributed to the decomposition of metal complexes and the crystallization of the Cu:NiO_x oxide. Thus, films present two stages of mass loss, at ~130 ^oC and ~300^oC for drying at 80^oC irrespective of Acac addition in precursor solution. The corresponding DTA results, presented in Figure 5.1(b), show a negligible exothermic peak at ~130 ^oC and a broad exotherm around ~300 ^oC, with corresponding low-grade abrupt and gradual mass losses, respectively. The latter suggests that the 2-methoxy ethanol, except its role as solvent, could also behave as a fuel. To support this, higher drying temperature (100 ^oC) for 1 hour was applied to the film's synthesis where most of 2-methoxy ethanol was evaporated. In this case, the TGA curve showed no mass loss and the corresponding DTA curve exhibited analogous behavior without any endothermic or exothermic reaction at 130 ^oC, while for the film prepared with a Acac/oxidizer molar ratio of 0.1 a marginal mass loss occurs during the first stage of combustion (at ~130 ^oC). This means for the films that non-combustive Cu:NiOx precursors require high temperatures of over 300 ^oC for the complete conversion of the precursors into the metal oxide lattice.

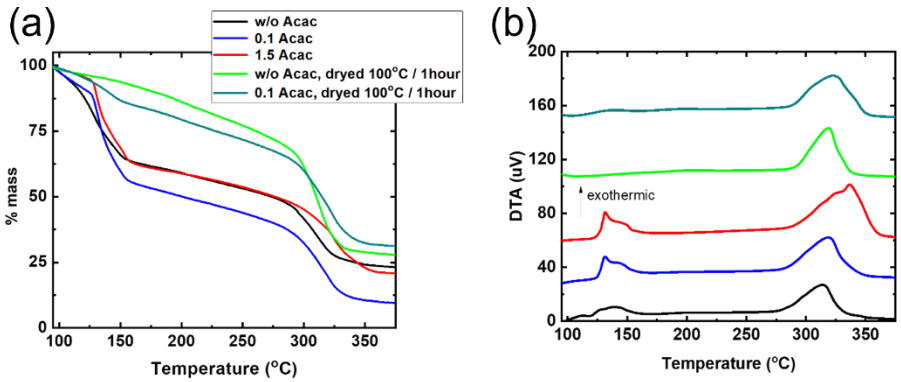

Figure 5.1 . (a) TGA curves of precursor films without (w/o) fuel and containing 0.1 and 1.5 molar ratio of fuel (Acac) to oxidizer (Cu, Ni nitrates) in 2-methoxy ethanol dried at 80 and 100 ^oC, and (b) the respective DTA curves.

Further, we compared the combustion synthesis behavior of Cu:NiO_x thin films (50, 200, 300 nm) and bulk analogues (thickness range of a few microns). TGA profiles (Figure 5.2(a)) show that by increasing the thickness of the film, a more intense gradual mass loss occurs at ~130 ^oC, with the second mass loss at ~300 ^oC becoming less prominent, while comparatively full combustion could occur at bulk materials at ~130 ^oC. Thus, we can infer that the mass of the precursor has a significant impact on the complete combustion synthesis reactions. The DTA results, in Figure 5.2(c), are in accordance with TGA profile where the raise of thickness in Cu:NiOx precursors layers shows a more intense exothermic peak at 130 ^oC; this corresponds to almost complete mass loss, decreasing gradually the exothermic peak at around 300 ^oC. Additionally, the absence of fuel (Acac) and the impact of solvent was examined once again during the combustion process for bulk materials. As observed in TGA profile (Figure 5.2(b)), a rapid mass loss occurs at ~130 ^oC w/o Acac for samples dried at 80 and 100 ^oC for 5 min, respectively. The corresponding DTA curves (Figure 5.2(d)) show single sharp exotherms at ~ 130 ^oC that corresponds exactly to the abrupt mass loss in the TGA (Figure 5.2b); this process is ample to lead the reaction rapidly to completion for metallic Ni formation. In contrast, in preheated sample at 100 ^oC for an extended period (48 h), where most of the solvent was evaporated, combustion reaction could not occur. This sample exhibits only an intense exothermic peak around ~300 ^oC, that corresponds to the crystal phase formation of NiO. These observations are in agreement with previous reports that the organic solvent 2-methoxy ethanol play a dual role of acting both as a solvent and also as a fuel in addition to Acac for the formation of the metal oxide lattices by the solution combustion synthesis.[143]

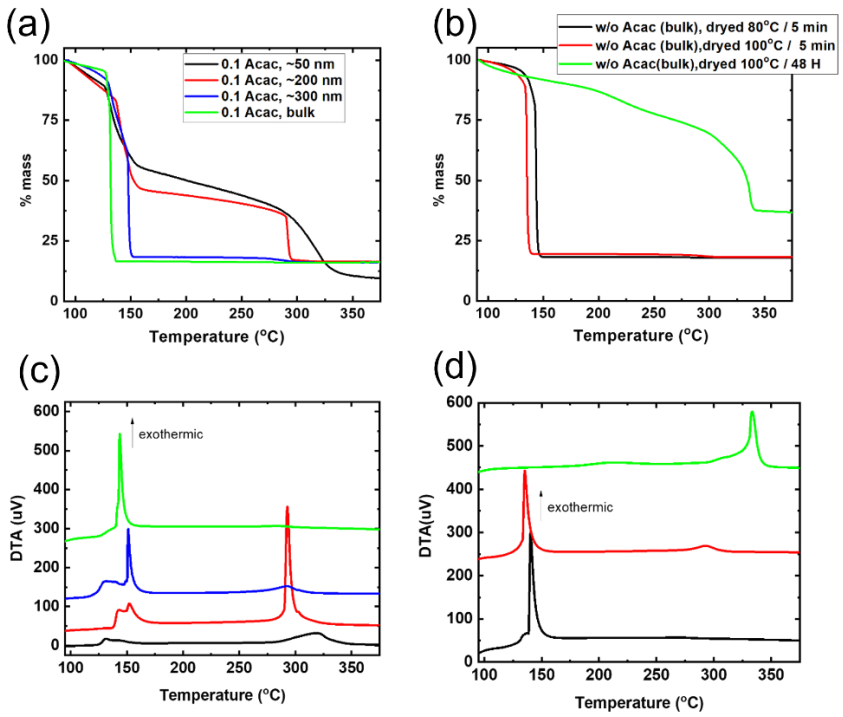

Figure 5.2 (a) TGA curves of different thickness (50, 200, 300 nm and bulk) films containing 0.1 molar ratio of fuel (Acac) to oxidizer (Cu, Ni nitrates) in 2-methoxy ethanol and (b) TGA curves of combustion-synthesized bulk samples prepared from precursor with Cu and Ni nitrates but without (w/o) Acac and 2-methoxy ethanol as solvent dried at 80 ºC and 100 ºC for 5 min and at 100 ºC for 48 h. The respective DTA curves for (c) different thickness (50, 200, 300 nm and bulk) and (d) bulk samples

5.2.2 XRD results of Cu:NiOx films and bulk precursors

The crystallinity of the SCS Cu:NiO_x thin films (identical to the Cu:NiO_x HTLs that were used within the inverted PVSCs) was examined using X-ray diffraction (XRD) analysis. Figure 5.3 presents the XRD patterns of the films prepared using w/o, 0.1 and 1.5 Acac and annealing temperatures of 150, 200 and 300 ºC. The crystal phase of NiO can be obtained for annealing temperature 300 ºC regardless of the containing amount of Acac, while for 150 and 200 ºC no crystal phase was detected. For 300 ºC annealing temperature, the characteristic diffraction peaks of NiO appeared at 2θ =

37.20°, 43.0°, 62.87° and 75.20°, which can be indexed to the cubic crystal structure of NiO as (111), (200), (220) and (311) planes, respectively (JCPDS No. 01-089-5881). For the film containing 1.5 Acac and annealed at 300 ºC, the formation of mixed crystal phases of NiO and metallic Ni was observed. Specifically, XRD patterns, along with the NiO diffractions, reveal additional peaks at 2θ = 44.0°, 52.3° and 76.5° assigned to (111), (200) and (220) planes, respectively, of the face-centered cubic (FCC) phase of Ni (JCPDS No.87-0712).

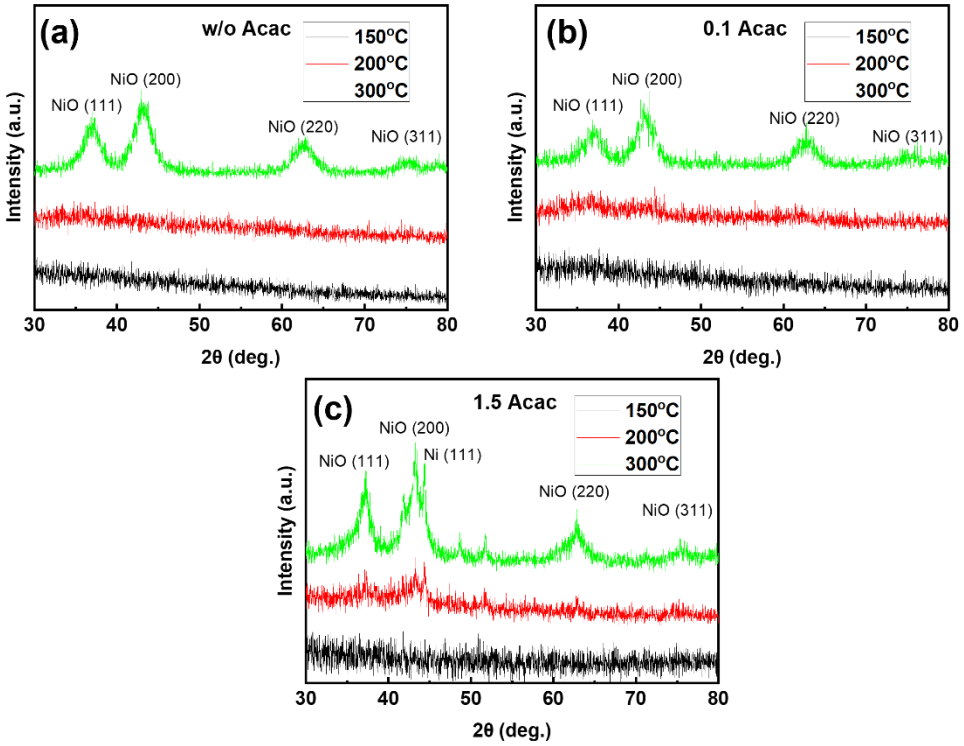

Figure 5.3 XRD patterns of the combustion synthesis of precursor films containing (a) w/o fuel (Acac), (b) 0.1 and (c) 1.5 molar ratio of fuel (Acac) to oxidizer (Cu, Ni nitrates) annealed at 150, 200 and 300 ºC .

The crystallinity of as-prepared materials obtained by combustion reaction of the bulk precursors was also examined using XRD analysis (Figure 5.4). Specifically, different initial molar ratios of the fuel to oxidizer (w/o, 0.1 and 1.5 Acac) at 200 ºC

annealing temperature of the bulk precursors were compared. The XRD results show significant improvement in the crystallinity of the bulk Cu:NiO_x compared to the corresponding thin films. Moreover, the required annealing temperature for the crystal phase formation is significantly reduced (as was also evidenced by TGA analysis) when using solution combustion synthesis of bulk materials as compared to the thin films. In the case of samples synthesized by bulk precursors, mixed crystal phases of metallic Ni (dominant species) and metal oxide NiO (residual species) were obtained, regardless of the molar ratio of fuel to oxidizer precursors. Specifically, XRD patterns reveal intense peaks appeared at 44.0°, 52.3° and 76.5° assigned to the (111), (200) and (220) planes, respectively, of face-centered cubic Ni (JCPDS No. 87-0712) (main product). The presence of Ni phase is an indication of combustion with a rich fuel precursor, so even in the precursor w/o Acac the Ni phase is the main product implying again that 2-methoxy ethanol plays a dual role of acting both as a solvent and fuel.[144] The high crystallinity of bulk materials, as evidenced by the sharper diffractions in XRD patterns, is attributed to the release of high energy in the exothermic reaction that occurred by solution combustion synthesis (SCS). Thus, in agreement with the findings from TGA measurements, the complete combustion occurs mainly due to the bulk precursor material, which has a higher mass compared to corresponding films.[117]

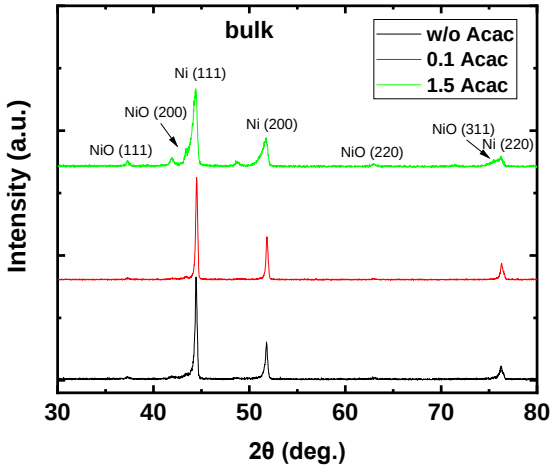

Figure 5.4 XRD patterns of combustion-synthesized samples (bulk) prepared from precursors containing w/o, 0.1 and 1.5 molar ratio of fuel (Acac) to oxidizer (Cu, Ni nitrates) annealed at 200 ºC.

5.2.3 Cu:NiOx thin films characterization

X-ray photoelectron spectroscopy (XPS) was employed to investigate the chemical state of the Cu:NiO_x surface. The XPS survey scans of the Cu:NiOx films synthesized with 0.1 Acac and annealed at 200 and 300 ºC evidenced the presence of Ni, Cu, O and C elements (Figure 5.5). In the Cu:NiOx film annealed at 200 ºC, the N1s spectrum indicated the presence of some reduced nitrogen (399.8 eV), and NiO_2^- (403.6 eV) and NiO_3^- (406.8 eV) containing species (Figure 5.6(a)), while the N1s scan of the 300 ºC annealed film showed the exist of reduced nitrogen (399.0) and NO_x (405.6 eV) residues (Figure 5.6b). For the film annealed at 200 ºC, the spectrum of the Ni 2p region (Figure 5.6c) showed a double peak at 856.3 eV (Ni $2p_{3/2}$) and 874.0 eV (Ni $2p_{1/2}$) binding energies, accompanying with shake-up satellite peaks at 862.0 eV and 879.7 eV, which are characteristic of Ni^{2+}–oxygen bonded complexes, possibly in the form of $Ni(acac)_2$. While the XPS Ni 2p spectrum of the 300 ºC annealed film (Figure 5.6(d)) indicated the presence of NiO, showing a characteristic double peak at

854.6 eV (Ni $2p_{3/2}$) and 872.3 eV (Ni $2p_{1/2}$) binding energies (spin-orbit splitting of 17.7 eV) along with shake-up satellite peaks at 861.2 and 878.8 eV. Furthermore, the XPS Cu 2p spectrum of the 300 ^{o}C annealed film (Figure 5.6e) exhibited a double peak at 934.2 eV and 953.9 eV due to the Cu $2p_{3/2}$ and Cu $2p_{1/2}$ core level components of the CuO (Cu $2p_{3/2}$: 934.7 eV and Cu $2p_{3/2}$: 954.5 eV for the 200 ^{o}C annealed film (Figure 5.6(f)) consistent with other reports. As for the broad signals located at 940.6 and 953.9 eV (943.0 eV for the 200 ^{o}C annealed film), they are assigned to the shake-up satellite peaks of paramagnetic Cu^{2+}. The incorporation of Cu^{2+} ions into the NiO lattice was also verified by the Auger α parameter, that is, the kinetic energy of the Cu $L_3M_{4,5}M_{4,5}$ Auger peak + binding energy of the Cu $2p_{3/2}$ peak. For the 300 ^{o}C annealed film, the Auger parameter is calculated to be 1851.8 eV, which respects the existing phase of CuO. Quantitative analysis from the XPS spectra also indicated that the film annealed at 200 ^{o}C contains 6.51 wt.% CH_xO_y and 3.32 wt.% NO_x containing organic compounds, while the corresponding remnants for the 300 ^{o}C annealed film was found to be 0.64 wt.% and 0.33%, respectively, see Table 5. The higher amount of remnants found in 200 ^{o}C annealed film suggests the incomplete combustion reaction of Cu:NiOx precursors, in agreement with the TGA results. Also, the Cu atomic concentration (Cu doping level) in the Cu:NiOx films annealed at 200 and 300 ^{o}C was found to be 5.64 % and 5.84 %, respectively, very close to the nominal composition.

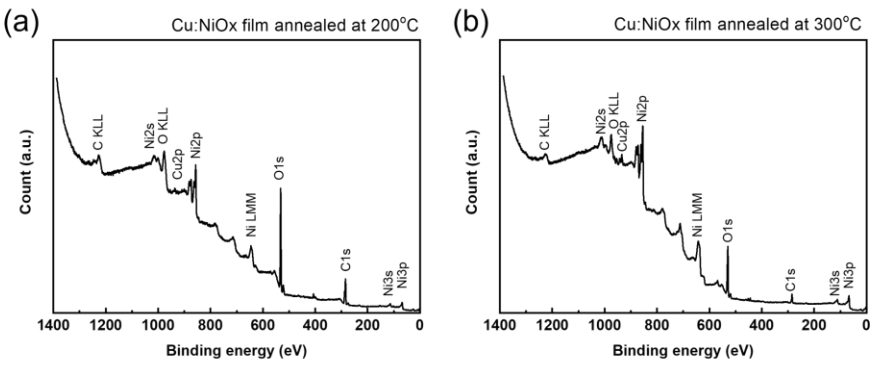

Figure 5.5 XPS survey spectra of the Cu:NiOx films fabricated form precursor containing 0.1 Acac and annealed at (a) 200 ºC and (b) 300 ºC.

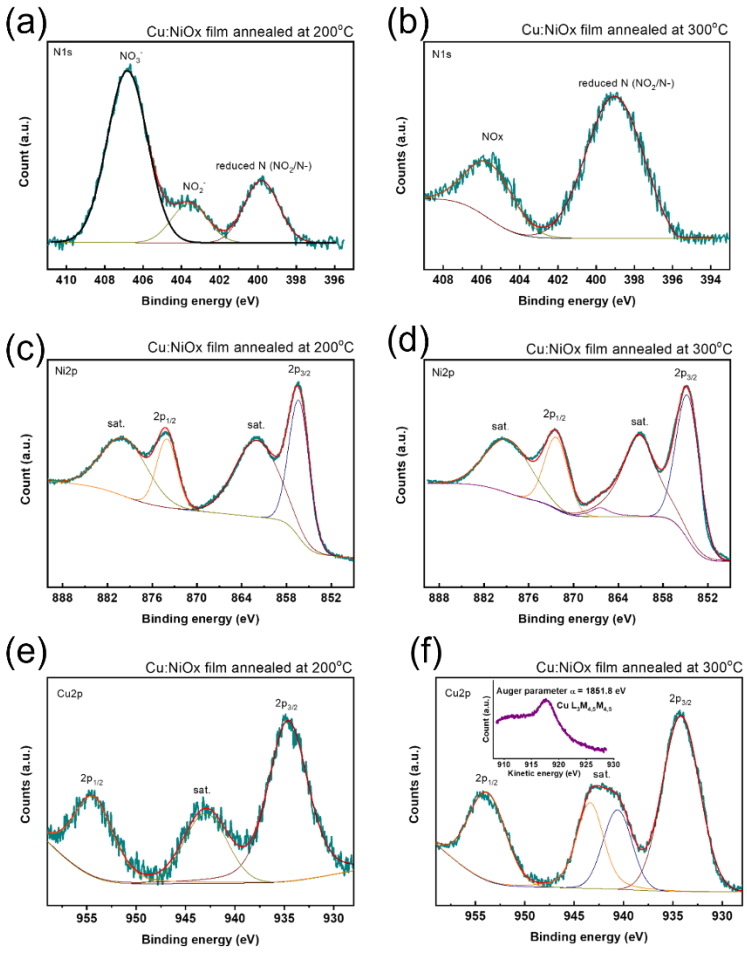

Figure 5.6 XPS spectra of the (a) ,(b) N 1s , (c),(d) Ni 2p and (e),(f) Cu 2p region of the Cu:NiOx films fabricated from precursor containing 0.1 Acac and annealed at 200ºC and 300 ºC. Inset of panel (f): the Cu $L_3M_{4,5}M_{4,5}$ Auger XPS spectrum

Table 5 XPS calculated atomic ratios for the Cu:NiOx films fabricated form precursor containing 0.1 Acac and annealed at 200 and 300 ºC.

Sample	C[a] (%)	N[b] (%)	Ni (%)	Cu (%)	O (%)
200 ºC annealed Cu:NiOx film	18.40	8.05	17.59	2.10	53.86
300 ºC annealed Cu:NiOx film	3.26	1.45	42.11	5.22	47.95

[a]C-oxygen/nitrogen bonded species corresponding to a 6.51 and 0.64 wt.% content for 200 and 300 ºC annealed Cu:NiOx films, respectively. [b]Nitrogen-containing species corresponding to a 3.32 and 0.33 wt.% content for 200 and 300 ºC annealed Cu:NiOx films, respectively.

Furthermore, we examined the film topography of Cu:NiO_x films fabricated on quartz substrates by contact angle and UV-Vis spectroscopy. Figure 5.7 shows the film morphology using AFM for the films synthesized from precursors containing 0.1 Acac and annealed at 150 and 300 ºC, respectively. It is clearly observed that the film treated at 150 ºC shows a featured structure of large particles, which possibly formed due to the presence of residues, with a surface roughness of 1.5 nm (Figure 5.7a). On the other hand, the film treated at 300 ºC does not show structured features due to the small size of the Cu:NiO_x particles, exhibiting a surface roughness of 0.7 nm (Figure 5.7b). The final thickness of the film annealed at 150 and 300 ºC is ~80 and ~50 nm, respectively, due to considerable amount of residues remained into 150 ºC annealed film.

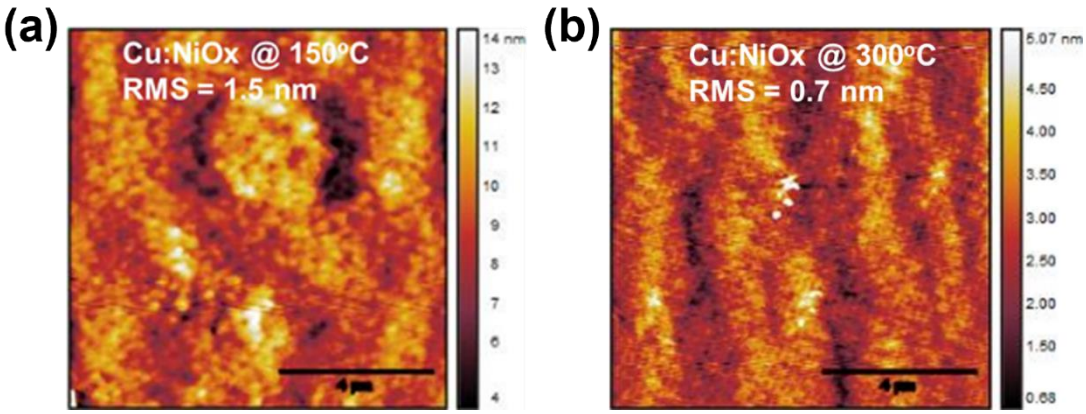

Figure 5.7 AFM images of Cu:NiOx films fabricated on quartz substrates from precursor containing 0.1 molar ratio of fuel (Acac) to oxidizer (Cu, Ni nitrates) annealed at (a) 150 and (b) 300 °C.

UV-vis measurements (Figure 5.8) on the films treated at 150 and 200 °C shows no prominent absorption due to the amorphous nature of metal oxides, while for 300 °C annealing film an absorption onset at ~400 nm (~3.1eV) and strong absorption at ~350 nm (~3.5 eV) is ascribed to the crystalline Cu:NiO_x phase.

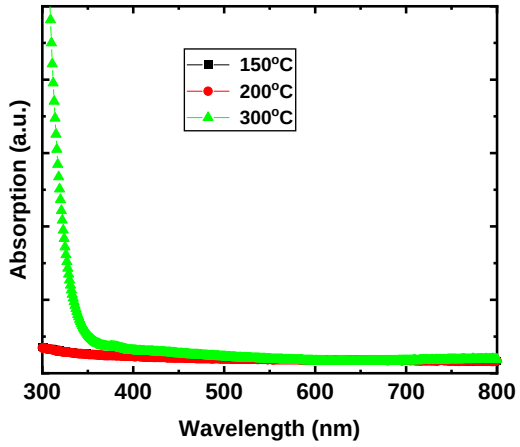

Figure 5.8 UV-Vis absorption of Cu:NiOx films fabricated on quartz substrates from precursor containing 0.1 molar ratio of fuel (Acac) to oxidizer (Cu, Ni nitrates) annealed at 150, 200 and 300 °C.

The contact angle of water was measured on films annealed at 150, 170 and 200 ^{o}C, using fuel to oxidizer ratio 0 (w/o), 0.1 and 1.5 and the measured values are plotted in Figure 5.9. All the contact angles are higher than 60 deg. irrespective to fuel concentration, in contrast to the contact angle of Cu:NiO_x film (0.1 molar ratio of Acac to oxidizer) annealed at 300 ^{o}C which is substantially lower (20 deg.). Thus, we infer that the remnants in the low temperature treated film form a Cu:NiO_x surface with moderate wettability, while the films annealed at 300 ^{o}C where the surface is almost free from remnants show an improved wettability.

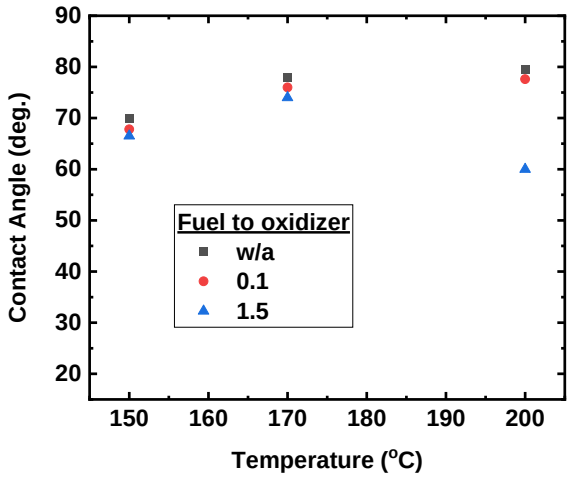

Figure 5.9 A graph presenting the contact angles of water on films prepared using precursor containing w/o Acac, 0.1 and 1.5 molar ratio of fuel (Acac) to oxidizer (Cu, Ni nitrates) annealed at 150, 170 and 200 ^{o}C.

5.2.4 J-V characterization of Cu:NiO_x films as HTLs in planar p-i-n PVSCs

To evaluate the functionality of the different Cu:NiO_x films as HTLs in solar cells, 50 nm thick Cu:NiO_x films, synthesized using the previous described conditions, were implemented in inverted perovskite solar cells with structure ITO/Cu:NiO_x/perovskite/$PC_{60}BM$/BCP/Ag and the J-V device characteristics under 1 sun simulated light were recorded.

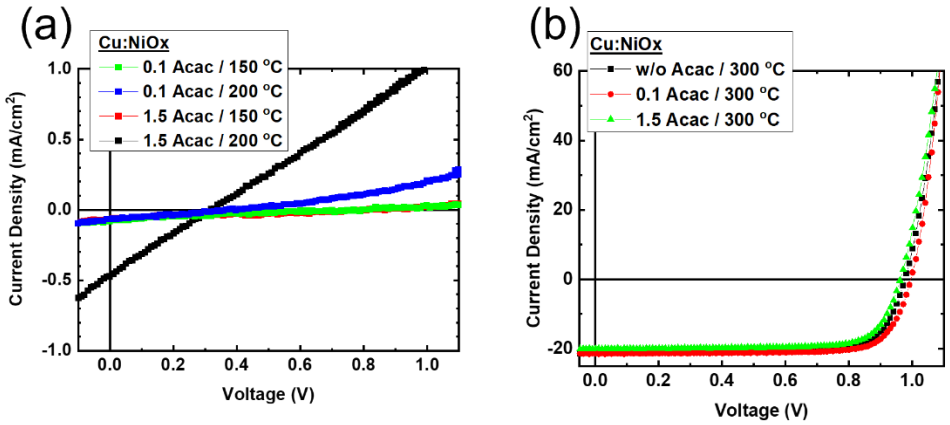

Figure 5.10 J-V curves of ITO/Cu:NiOx/perovskite/PC60BM/BCP/Ag devices under 1 sun simulated light for Cu:NiOx films fabricated from precursor containing 0.1 and 1.5 molar ratio of fuel (Acac) to oxidizer (Cu, Ni nitrates) annealed at 150 and 200 °C.

As it is presented in J-V curves of Figure 5.10(a) the devices that incorporate Cu:NiO_x films annealed at 150 °C and 200 °C exhibited a very limited functionality. All the devices show low V_{oc} in the range of 0.3 V and the generated current is below 1 mA/cm^2. The device with 1.5 molar ratio Acac to oxidizer and annealed at 200 °C shows almost linear response of the current density to the sweeping voltage, which can be attributed to partially formed metallic Ni, as can be inferred by the corresponding XRD

results. In contrast, the inverted perovskite solar cells which incorporate Cu:NiO_x HTLs prepared from precursor solutions containing w/o, 0.1 and 1.5 Acac annealed at 300 ^oC delivered higher efficiency. In Figure 5.10(b), the J-V curves of the best performing devices under 1 sun simulated light are illustrated and the extracted solar cell parameters of the studied devices are presented in Table 6 – in brackets are the average values of 12 devices for each batch. Regarding the impact of fuel to oxidizer ratio on the devices PCE, the devices with Cu:NiO_x HTL where the precursor contained no fuel (w/o Acac) and 0.1 Acac ratio showed similar PCE values and the devices which incorporate Cu:NiO_x film synthesized with 1.5 Acac/oxidizer ratio shows a reduced V_{oc} and J_{sc} efficiency, resulting in lower PCE.

Table 6 Extracted solar cell parameters of the best ITO/Cu:NiOx/perovskite/$PC_{60}BM$/BCP/Ag devices. In bracket the average values of 12 devices for each batch are shown.

Sample	V_{oc} (V)	J_{sc} (mA/cm^2)	FF (%)	PCE (%)
w/o Acac	0.98 (0.97)	21.11 (20.64)	77.1 (72.3)	15.97 (14.48)
0.1 Acac	0.99 (0.97)	21.40 (20.75)	78.2 (73.8)	16.58 (14.85)
1.5 Acac	0.96 (0.94)	20.03 (19.64)	77.3 (73.1)	14.90 (13.50)

The experimental results presented within this study using a triple cation $Cs_{0.04}(MA_{0.17}FA_{0.83})_{0.96}$ $Pb(I_{0.83}Br_{0.17})_3$ perovskite formulation infer that the Cu:NiO_x oxide's precursor films that were annealed at temperatures of 150 and 200 ^oC produce electronic films that cannot function as HTLs for efficient inverted perovskite solar cells. This is ascribed to the incomplete combustion that results in amorphous Cu:NiO_x films with remnants. This result is in agreement with previous report where amorphous NiO_x showed limited functionality as HTL when applied in organic solar cells.[145] On the other hand, as shown above pure crystalline phase of Cu:NiO_x HTL obtained with

annealing at 300 ^{o}C for the precursors w/o and 0.1 ratio of Acac/oxidizer whereas for 1.5 ratio metallic Ni are likely to be present within Cu:NiO_x films (as indicated within the XRD pattern in Figure 5.3(c)).

The pure crystalline phases (w/a and 0.1 ratio Acac/oxidizer) of Cu:NiOx resulted to better PCEs 15.97 % (average 14.48 %) and 16.58 % (average 14.85 %), respectively; while for 1.5 ratio the of metallic Ni influence delivers lower PCE devices 14.90 % (average 13.50 %).

5.3 Summary

In Summary, we examined the solution combustion synthesis of Cu:NiO_x films by using different molar ratios (w/o, 0.1 and 1.5) of fuel acetylacetone (Acac) to oxidizer (nitrates) precursors as well as various thermal processing annealing temperatures (150, 200 and 300 ^{o}C). Thermogravimetric analysis (TGA and DTA) results showed that complete combustion process at ~150 ^{o}C can occur in bulk analogues. XRD measurements revealed that the corresponding Cu:NiO_x films crystallize to NiO phase upon annealing temperature at 300 ^{o}C, irrespectively to Acac concentration, while for lower annealing temperatures (150, 200 ^{o}C) no crystal phase was observed. XPS, AFM, UV-Vis spectroscopy and contact angle measurements on the films strongly support the incomplete combustion of the Cu:NiO_x thin films for annealing temperatures at 150 ^{o}C and 200 ^{o}C. XPS measurements on Cu:NiO_x film revealed the presence of high atomic ratio of remnants for thermal annealing at 200 ^{o}C which are remarkably reduced for films annealed at 300 ^{o}C. Surface topography images and thickness measurements via AFM and profilometer showed that the Cu:NiO_x films

annealed at 300 ^{o}C have a lower thickness (~50 nm) and roughness (~0.7 nm) compared to ~80 nm thickness and ~1.5 nm roughness for the Cu:NiO_x films annealed at temperatures 150 ^{o}C due to remnants in the film. Moreover, Cu:NiO_x films annealed at 300 ^{o}C have an improved hydrophilicity, showing a contact angle of 20 deg., while the films annealed at 150 ^{o}C and 200 ^{o}C show angles more than 60 deg due to surface remnants. Regarding the optical absorption measurements, the 300 ^{o}C thermally annealed films exhibit a distinct absorption curve ascribed to the formed crystalline Cu:NiO_x, while the lower annealing temperature films at 150 ^{o}C and 200 ^{o}C lack any strong absorption in the range of measured wavelengths due to amorphous phase; these results are consistent with the paper reported XRD findings. The presented solution combustion chemistry findings in Cu:NiO_x thin films are confirmed by applying the various ratios of Acac/Oxidizer and annealing processing temperatures of SCS based Cu:NiO_x HTLs in triple cation based $Cs_{0.04}(MA_{0.17}FA_{0.83})_{0.96}$ $Pb(I_{0.83}Br_{0.17})_3$ inverted PVSCs. The Cu:NiOx HTLs annealed at temperatures 150 ^{o}C and 200 ^{o}C irrespective to Acac/Oxidizer ratios provided limited functionality PVSCs due to incomplete combustion process that resulted to amorphous Cu:NiO_x with remnants as confirmed by the presented XRD and XPS measurements respectively. The crystalline phase of Cu:NiO_x HTLs and efficient inverted PVSCs performance obtained at annealing temperature of 300 ^{o}C irrespective to Acac/Oxidizer ratio. Following the solution combustion synthesis route that have been investigated within this manuscript, the Cu:NiO_x crystalline HTLs annealed at 300 ^{o}C with 0.1 ratio of Acac/oxidizer resulted to 16.58 % PCE for the triple cation based $Cs_{0.04}(MA_{0.17}FA_{0.83})_{0.96}$ $Pb(I_{0.83}Br_{0.17})_3$ inverted PVSCs.

6 Nitrobenzene as Additive to Improve Reproducibility and Degradation Resistance of Highly Efficient Methylammonium-Free Inverted Perovskite Solar Cells

6.1 Abstract

We show that the addition of 1% (v/v) nitrobenzene within the perovskite formulation can be used as a method to improve the power conversion efficiency and reliability performance of methylammonium-free (CsFA) inverted perovskite solar cells. The addition of nitrobenzene increased power conversion efficiency (PCE) owing to defect passivation and provided smoother films, resulting in hybrid perovskite solar cells (PVSCs) with a narrower PCE distribution. Moreover, the nitrobenzene additive methylammonium-free hybrid PVSCs exhibit a prolonged lifetime compared with additive-free PVSCs owing to enhanced air and moisture degradation resistance.

6.2 Results

6.2.1 Perovskite Solar Cells

To investigate the additive engineering of methylammonium-free (CsFA) perovskite PVs with nitrobenzene, two batches (12 samples in each batch) of PVSC with the structure glass/ITO/NiOx/Perovskite/$PC_{60}BM$/BCP/Cu were prepared. For the methylammonium free (CsFA) perovskite, active layers were fabricated by applying deposition parameters similar to Kelly Schutt et al., while for the bottom electrode NiOx, hole transporting layers (HTLs) were fabricated on ITO by solution combustion process similar to Jae Woong Jung et al. .[106,122] The $PC_{60}BM$ electron transporting layer (ETL) was spin-coated followed by thermal evaporation of bathocuproine (BCP) and copper (Cu) to complete the inverted PVSCs top electrode. Full details are provided within the Materials and Methods section. For the first batch, the perovskite solution was prepared without any additive, while the other batch was prepared with the addition of nitrobenzene in perovskite solution, where for both batches, the used perovskite composition is the methylammonium-free (CsFA) $Cs_{0.17}FA_{.0.83}Pb(I_{0.87}Br_{0.13})_3$. By applying different concentrations of nitrobenzene in the methylammonium-free (CsFA) perovskite precursor solution, PCE as a function of additive concentration was investigated and the optimum amount of nitrobenzene additive was identified to be 1% v/v (Figure 6.1).

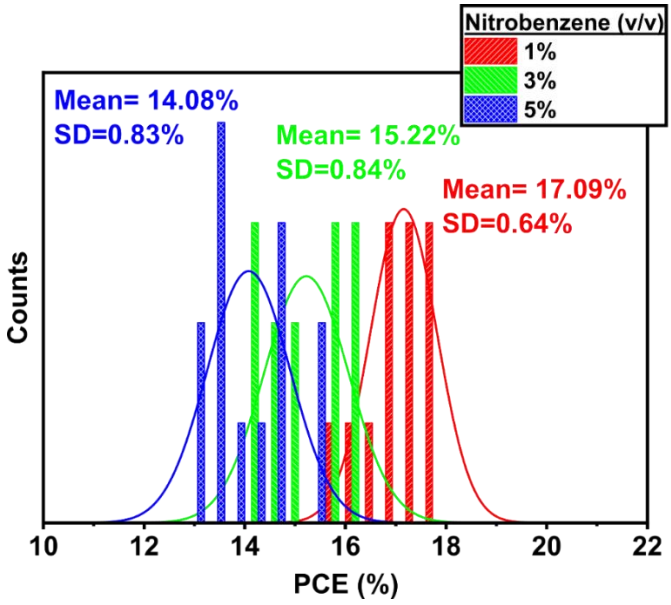

Figure 6.1 Mean PCE and standard deviation (SD) of PVSCs with different concentrations of nitrobenzene.

Figure 6.2(a) demonstrates the PCE distributions of the two batches of PVSC with and without 1% nitrobenzene, as well as the extracted mean and standard deviations, respectively. The batch with the nitrobenzene additive exhibits an increased mean PCE value of 17.09% compared with the reference (15.34%) with higher reproducibility, as the respective standard deviation of the former is almost half (0.64%) compared with the last (1.15%). Further, the best performing devices of each batch are presented in Figure 6.2(b) and the extracted photovoltaic (PV) parameters are in Table 7. The PVSC with the nitrobenzene delivers Voc = 0.92 V, Jsc = 24.36 mA/cm^2, and FF = 80.3%, delivering a PCE = 18.02%, while the reference device Voc = 0.89 V, Jsc = 23.99 mA/cm^2, and FF = 81.3%, delivering a PCE = 17.35%. The integrated current from the external quantum efficiency (EQE) (Figure 6.2(c)) is 22.78 and 23.17 mA/cm^2 for the nitrobenzene and reference device, respectively, consistent with the solar simulator

extracted values. The 1% nitrobenzene device shows an enhanced photo response for the wavelengths shorter than 500 nm compared with additive-free reference devices. It will be shown later through optical absorption measurements that nitrobenzene based methylammonium-free (CsFA) perovskite PVs exhibit an increased optical absorption at this range. The experimental results provide evidence that the addition of nitrobenzene results in better control of methylammonium-free (CsFA) perovskite active layer formation, while the observed increase in the reported Voc values indicates passivation of surface defects that consistently resulted in improving device performance reliability.

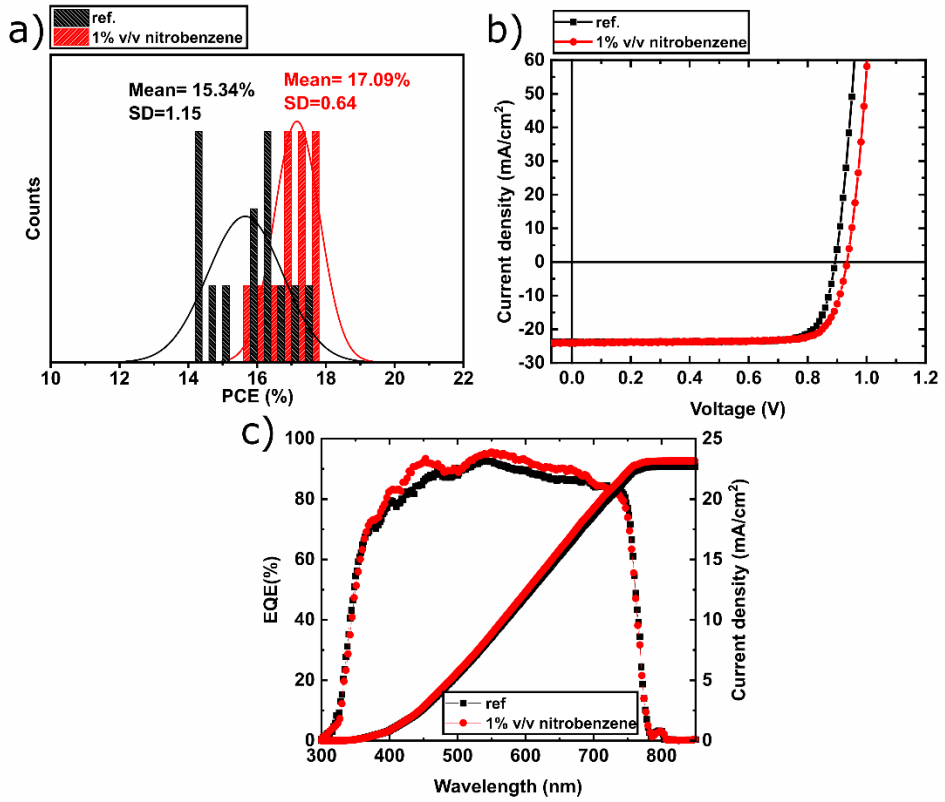

Figure 6.2 (a) The average power conversion efficiency (PCE) and standard deviation (SD) of methylammonium-free (CsFA) hybrid perovskite solar cells (PVSCs) with and without nitrobenzene and the corresponding (b) current density–voltage (J–V), (c) external quantum efficiency (EQE), and integrated current density of the best performing devices of each batch.

Table 7 Extracted photovoltaic (PV) parameters from the current density–voltage (J–V) curves of the best performing devices. PCE, power conversion efficiency.

Sample	V_{oc} (V)	J_{sc} (mA/cm^2)	FF (%)	PCE (%)
reference	0.89	23.99	81.3	17.35
1% v/v Nitrobenzene	0.92	24.36	80.3	18.02

6.2.2 Perovskite Solutions and Films' Characterization

Further measurements were performed to better clarify the effect of nitrobenzene addition into CsFA PVSCs. To probe the impact of nitrobenzene into the methylammonium-free (CsFA) perovskite formulation, UV–vis absorption measurements were conducted on each precursor solution, with their concentration being two-thirds the concentration used for the PVSC active layer formation in order to let enough light be transmitted through. Figure 6.3(a)shows the calculated Tauc-plots of the respective absorption spectra. It is revealed that the absorption band gap of the nitrobenzene-based PVSC formulations are red shifted (2.61 eV) compared with the reference solution (2.66 eV). As has been shown in previous reports, the formed complex of the perovskite precursors with molecules induces a red shift of the absorption edge for the solution under study. [146–149]Similarly, the observed red shift of the nitrobenzene containing solution compared with the reference is an indication of complex formation between the nitrobenzene additive and the colloidal particles of the perovskite precursor solution. Additional UV–vis measurements (Figure 6.3b) were performed on the ITO/NiOx/CsFA perovskite structure with and without nitrobenzene,

displaying similar spectra at the region up to ~500 nm, while an increase in the absorption of the nitrobenzene containing film was observed for wavelengths shorter than 500 nm. This change is ascribed to reduced light scattering owing to smoother active layer topography rather than to enhanced crystallinity, as the mean size of the grains exhibits a minor change, as shown by the AFM measurements analysis, which is provided below[150–156]To study grain boundary passivation effects, photoluminance (PL) (Figure 6.3c) measurements were performed on methylammonium-free (CsFA) perovskite films fabricated on glass substrates. The PL intensity of nitrobenzene containing methylammonium-free (CsFA) perovskite film exhibits an increased intensity compared with the reference, suggesting less defect mediated charge-carrier recombination (non-radiative process), and thus less grain boundary defects. [157]

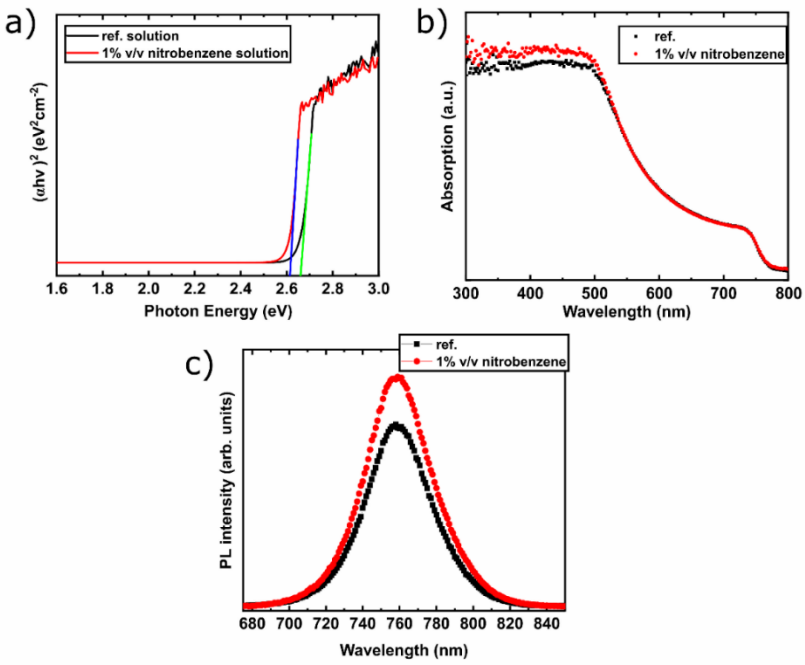

Figure 6.3 (a) Tauc plots of methylammonium-free (CsFA) perovskite with and without 1% v/v nitrobenzene additive calculated from the absorption measurements of precursor solutions and the corresponding (b) optical absorption and (c) photoluminescence (PL) of the resulting films fabricated on ITO/NiOx/CsFA and glass substrates, respectively.

To investigate the topography of methylammonium-free (CsFA) perovskite, films were fabricated following the exact same processing conditions that have been applied to corresponding PVSCs on ITO/NiOx substrates with thickness of ~500 nm (determined by profilometry measurements). Atomic force microscopy (AFM) measurements were conducted on the corresponding active layers, with the calculated roughness (root mean square) of the nitrobenzene containing active layer being reduced by ~30% compared with the additive free active layer. Specifically, for the 50 × 50 μm image (Figure 6.4(a),(c)), the roughness decreases from 29.9 nm to 22.8 nm and, for the 10 × 10 μm image (Figure 6.4(b),(d)), from 17.7 nm to 13.5 nm. From the grains' size distribution (Figure 6.5(a),(b)), it is calculated that the addition of nitrobenzene reduces both the mean grain size and the standard deviation to 304 nm from 329 nm and to 103% from 118%, respectively. Thus, the nitrobenzene containing methylammonium-free (CsFA) perovskite active layers show reduced thickness inhomogeneity and higher compactness, which can be ascribed to retarded crystal growth owing to the formed complex of nitrobenzene with the precursor particles.[158,159]

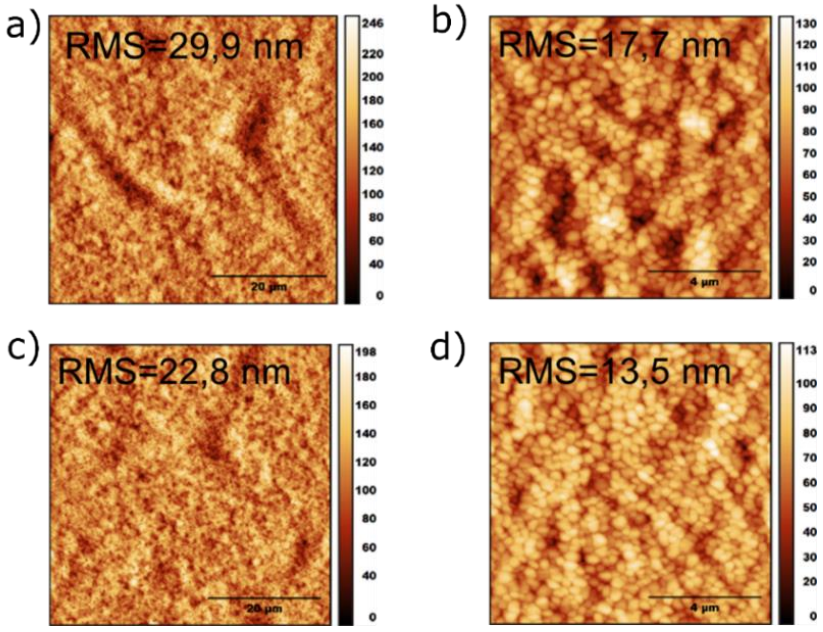

Figure 6.4 Topography pictures with sizes 50 × 50 µm (a,c) and 10 × 10 µm (b,d) obtained with atomic force microscopy (AFM) and the calculated roughness of the (a,b) reference and (c,d) nitrobenzene containing methylammonium-free (CsFA) perovskite films fabricated

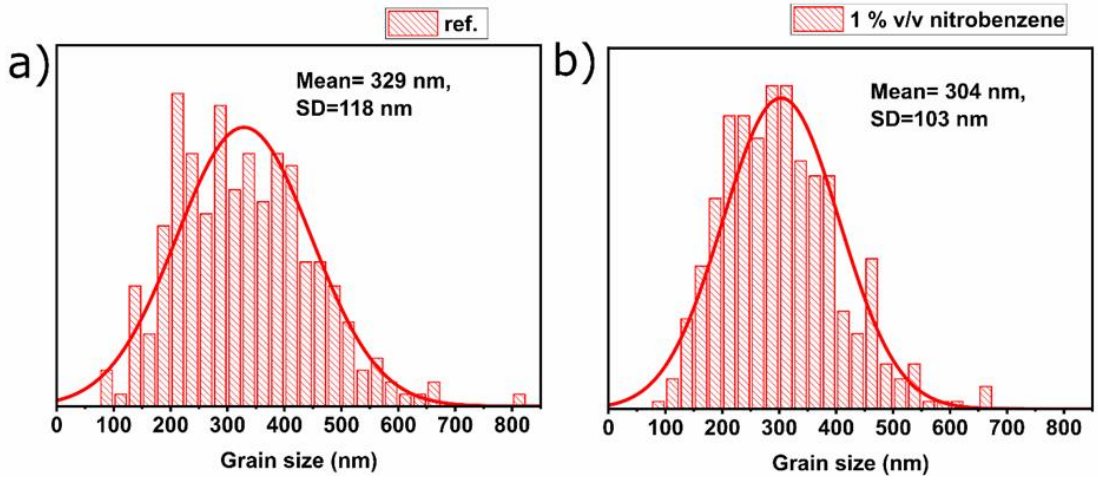

Figure 6.5 Grain size distribution of pristine and nitrobenzene containing perovskite films fabricated on top of ITO/NiOx substrates

We also examined whether the improved properties of the inverted PVSC were induced by the interaction of the additive with the hole transporting oxide layer (NiOx-

underlayer). As NiOx is a nanoparticulate-based functional layer, the high surface area/high number of surface defects could result in high reactivity with nitrobenzene, which might affect the perovskite formation process.[160] Two batches of PVSC were fabricated (with and without nitrobenzene) replacing the NiOx with the PEDOT/PSS as the most common organic hole transporting layer used within inverted PVSC. Consistent with our previously reported experimental evidence using NiOx HTLs, the inverted PVSCs containing nitrobenzene and PEDOT/PSS as HTL also exhibit improved PCE reproducibility with a standard deviation of 0.69% compared with additive-free PVSCs (1.61%), as shown in Figure 6.6. The above experimental results provide further indication that the origin of the improved performance of the PVSCs is owing to the interaction of the 1% (v/v) nitrobenzene additive with methylammonium-free (CsFA) perovskite precursors rather than nanoparticulate metal-oxide based underlayer effects.

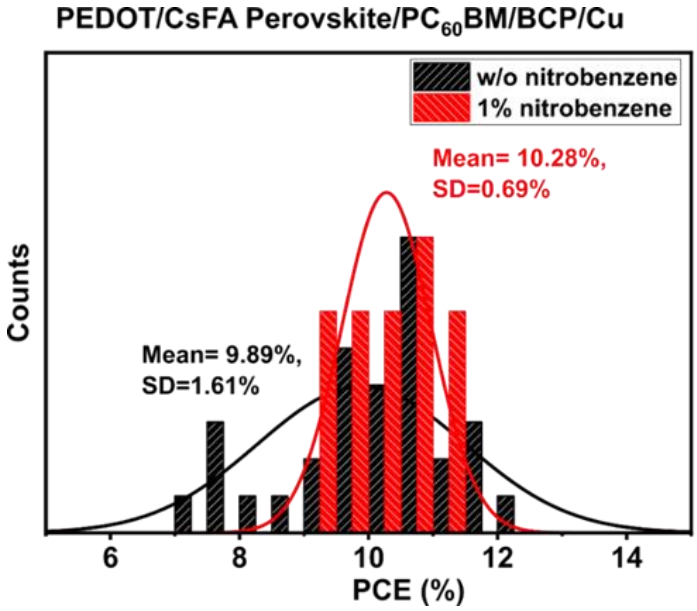

Figure 6.6 Mean PCE and standard deviation (SD) of PVSC with and without nitrobenzene fabricated on ITO/PEDOT:PSS substrate.

6.2.3 Lifetime Testing of Perovskite Solar Cells

Air stability measurements were performed on methylammonium-free (CsFA) PVSC with and without nitrobenzene, where all devices were encapsulated in inert atmosphere (N_2) before exposure to air. Figure 6.7(a) presents the mean PCE and the standard deviation measurements throughout ageing in ambient conditions. First, it can be observed that the mean PCE of the nitrobenzene containing PVSCs retain around 85% of the initial PCEs after 1500 h, in contrast to the reference PVSCs that decline to approximately 65%. Moreover, the PCE dispersion of reference PVSCs widens significantly during the ageing test compared with nitrobenzene PVSCs. Regarding the champion devices (Figure 6.7(b)), the nitrobenzene containing inverted PVSCs exhibit excellent performance, retaining 95% of the initial PCE after 1500 h in air. The results show that the addition of nitrobenzene into methylammonium-free (CsFA) perovskite improves the air stability of the corresponding encapsulated inverted PVSCs.

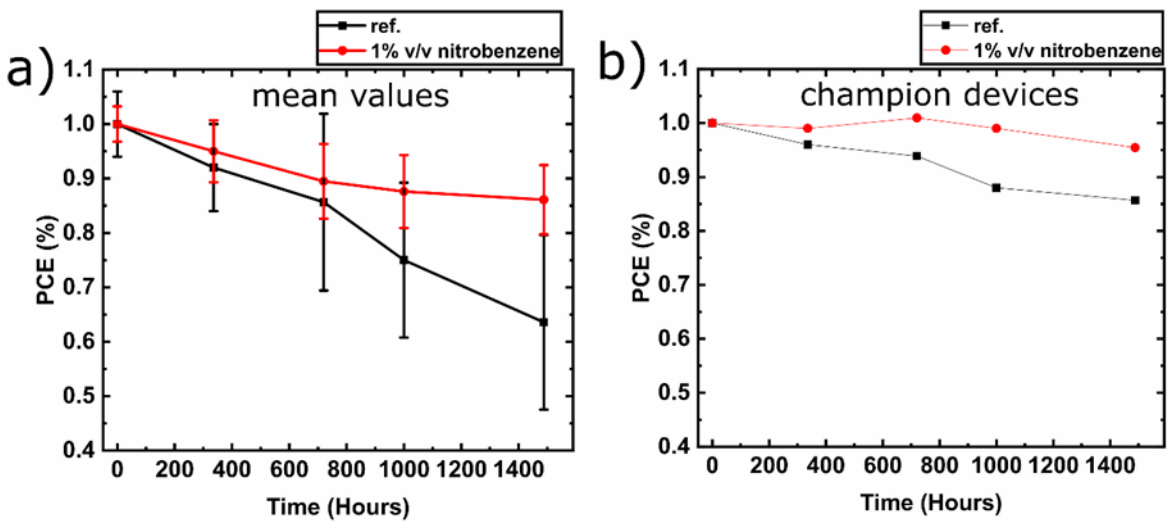

Figure 6.7 (a) Mean PCEs and standard deviations graph of air stability measurements for the encapsulated methylammonium-free (CsFA) PVSC with and without nitrobenzene and (b) the corresponding champion devices.

Further to the above air stability measurements, accelerated humidity lifetime testing was also investigated (75 RH% and 22 °C). During this ageing process, device lifetime performance was combined with corresponding photocurrent mapping (PCM) measurements. Figure 6.8 illustrates the PCE and the corresponding PCM images of the additive-free and nitrobenzene based PVSCs, while the additional normalized PV efficiency parameters Jsc, Voc, and FF as a function of lifetime are presented in Figure 6.9. The red color of the PCM represents the areas of high photogenerated current, while the yellow to blue color indicates the areas of lower photocurrent. Like the above presented air-stability measurements, the nitrobenzene containing device shows an increased humidity ageing resistance, retaining 85% of its initial PCE for over 400 h. Accordingly, from PCM, it can be seen that the generated photocurrent shows a marginal decrease after 350 h, mostly at the edges of the device area. On the other hand, the additive-free device shows a significant decrease of its initial PCE within the first

hours. The yellow spots (reduced photocurrent) at the PCM for the additive-free PVSCs are observed within the first 50 h, followed by a very aggressive photo-current degradation within the next 250 h.

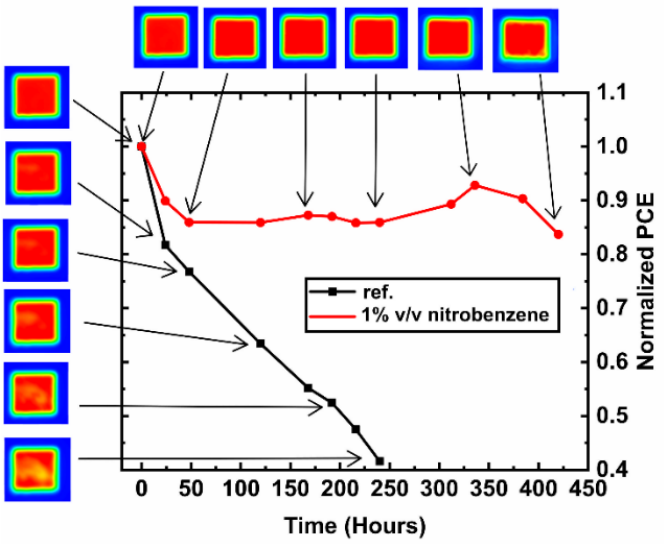

Figure 6.8 Stability measurements for the encapsulated methylammonium-free (CsFA) perovskite devices with and without nitrobenzene at 75% relative humidity (RH) and 22 °C under dark and the respective photocurrent map of the corresponding devices.

The photocurrent mapping observations show good agreement with the recorded normalize Jsc values, which also show an abrupt decrease during accelerated humidity testing at similar time-scales (Figure 6.9(b)), whereas the normalized Voc and FF (Figure 6.9(a),(c)) show a relatively small variance within the presented lifetime performance compared with the initial values. The cause of this degradation can be ascribed to the interaction of perovskite with the H_2O through the formation of the monohydrate perovskite and then the dihydrate perovskite, which finally leads to its decomposition.[161] However, it remains unclear to us whether the degradation occurs at the interface of perovskite with carrier transporting layers or at the bulk perovskite (or

both).[162,163] It has been reported for other perovskite formulations (e.g., $CH_3NH_3PbI_3$, $FAPbI_3$) that the degradation initiates at the grain boundaries and propagates to the interior.[164,165] Thus, because, in our report, the stoichiometry of perovskite (same perovskite solution is used) and the grain sizes (shown with AFM measurements) are the same for the additive free and nitrobenzene additive based methylammonium-free (CsFA) perovskite, we infer that the origin of the enhanced degradation resistance of the nitrobenzene containing CsFA-based PVSCs is owing to the passivation of perovskite defects, through the reaction of nitrobenzene with the grain boundaries, as well as owing to the inhibition of moisture permeation in the perovskite attributed to the hydrophobic benzene ring.[163–168] At this initial stage, we have shown that the additive of nitrobenzene can improve the humidity life-time performance of PVSCs under 75% RH and 22 °C conditions.

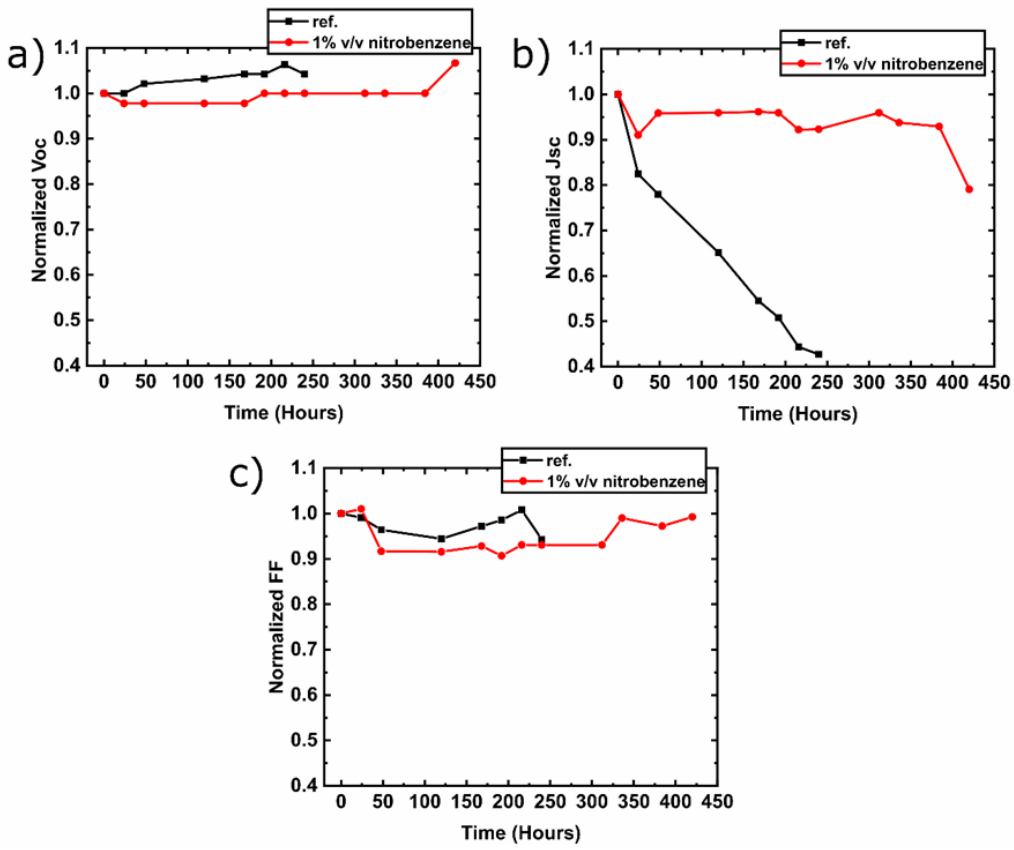

Figure 6.9 The normalized PV parameters current density (Jsc), Open circuit voltage (Voc) and fill factor (FF) of the corresponding PVSC with and without 1% nitrobenzene during accelerated lifetime testing

6.3 Summary

In Summary, the performance of methylammonium-free (CsFA) hybrid PVSCs that incorporate nitrobenzene additive is investigated. We have demonstrated that inverted methylammonium-free (CsFA) PVSCs using 1% v/v nitrobenzene additive provide an increased mean PCE from 15.34% to 17.09%, with a much narrower PCE standard deviation distribution (reduced from 1.15% to 0.64%) compared with corresponding additive-free PVSCs. The improved performance is attributed to the

interaction of perovskite's colloidal particles with nitrobenzene, as well as passivation of grain boundary defects. Importantly, the reported stability of the corresponding encapsulated air-exposed PVSCs under investigation is improved, retaining 85% of the initial PCEs after 1500 h compared with the additive-free devices, which decline to approximately 65% at the same air exposure time scales. Additional accelerated humidity lifetime testing (75% RH and 22 °C) shows that the nitrobenzene 1% v/v containing methylammonium-free (CsFA) inverted hybrid PVSCs exhibit enhanced humidity lifetime performance, retaining 85% of the initial PCE after more than 400 h compared with additive-free PVSCs, which decline within the first 50 h. The presented humidity-based accelerated lifetime studies (75% RH and 22 °C) combined with the photocurrent mapping measurements have shown that incorporation of nitrobenzene additive within the formulation of methylammonium-free (CsFA) hybrid inverted PVSCs can be used as a method to improve methylammonium-free (CsFA) hybrid PVSCs' lifetime performance owing to defect passivation and inhibition of moisture permeation.

7 Concluding Remarks

7.1 Conclusion

For the establishment of any new PV technology, it must provide certain advantages compare to already established or other emerging PV technologies. Accordingly, perovskite solar cells must owe these distinctive advantages to replace the established silicon solar cell technology. The triptych of success for the solar cells is the high-power conversion efficiency, environmental stability, and low fabrication cost. The much lower temperature requirements for hybrid (organic-inorganic) perovskite semiconductors compared to silicon, in combination with the achievable high PCE of the initial reported solar cells draw the attention of the research community on this novel hybrid semiconductor and motivated research and development efforts on hybrid perovskite solar cells. The rapid increment of PCE unveiled the needs for new processes and methods of fabricating the other components of perovskite solar cells device architecture (e.g. charge selective layers) as well as for major improvement of devices' environmental stability. This thesis has demonstrated novel HTL metal oxide materials using low cost and scalable fabrication techniques along with the improved perovskite solar cells' reliability as they are necessary steps toward industrialization of perovskite PV technology.

Within this thesis was first investigated the solution combustion synthesis of the p-type spinel films $NiCo_2O_4$ that was used as efficient HTL for perovskite solar cells. The scalable doctor blade technique used for the deposition method as well as the

implementation of the solution combustion synthesis method of the metal-oxide which requires relatively lower processing annealing temperatures, compared to commonly used sol-gel methods. Following the same perovskite fabrication process the solution combustion synthesized $NiCo_2O_4$ was further doped with Cu and Li improving HTL charge carrier selection properties. Thus, by the development of co-doped $NiCo_2O_4$ higher power conversion efficiency perovskite solar cells were achieved.

Next, it was examined in depth the solution combustion synthesis process of Cu:NiOx film, since it is a common high performing HTL for perovskite solar cells. Moreover, the simpler crystal structure of Cu:NiOx (rock salt structure) compared to much more complicated spinel structures allowed the easier investigation of the Cu:NiOx crystal formation under the various combustion synthesis conditions. The intention of this study was to find the lowest possible required annealing temperature for the solution combustion synthesis of the metal-oxide thin films, in order to reduce the energy demands for the production of the perovskite solar cells using metal-oxide based HTLs. Based on this work, the optimized conditions for the processing of functional Cu:NiOx HTLs are identified. Furthermore, it is shown that the combustion synthesis process of thin Cu:NiOx films differ from the bulk analogues, with the former requiring higher processing temperatures to crystallize. Thus, solution combustion synthesis behavior of thin-films cannot be deduced from the analogue bulk.

Finally, after the determination of the minimum required temperature for the solution combustion synthesis, solution combustion synthesized NiOx HTLs were used in perovskite solar cells. The perovskite active layer on this study was molecular engineered with the aim to improve fabrication reliability and humidity degradation resistance of the corresponding hybrid perovskite photovoltaics. Specifically, the

selected methyl ammonium free (Cs, FA) perovskite formulation was engineered with 1 % (v/v) Nitrobenzene resulting in more reproducible PCE devices with around three times prolonged lifetime under high humidity environmental conditions. The achieved higher mean and low distribution PCE combined with the reported prolonged humidity life-time performance of the corresponding hybrid perovskite PVs are important product development parameters towards commercialization.

7.2 Future perspectives

7.2.1 Solution process solar cells using n-type inorganic perovskite active layer

The UV intrinsic instability of the organic moieties within hybrid perovskite films leads to the appearance of various degradation processes of perovskite solar cells and thus sophisticated methods must be applied to increase the lifetime of the devices.[169] To mitigate this type of hybrid perovskite film's instability it can be investigated the replacement of hybrid perovskite films with inorganic perovskite materials suitable for photovoltaic applications. During this thesis inorganic perovskite solar cells using the solution combustion synthesis were developed and applied as absorbing layers in p-n type solar cells. In this study solution-processable iron manganite ($FeMnO_3$) nanoparticles were synthesized via chemical combustion. The formed ink was applied as n-type photoactive layer in all-oxide solar cells. Concretely,

functional combustion solution processed NiO/$FeMnO_3$ heterojunction photovoltaics was demonstrated fabricated on ITO back electrode (Figure 7.1).

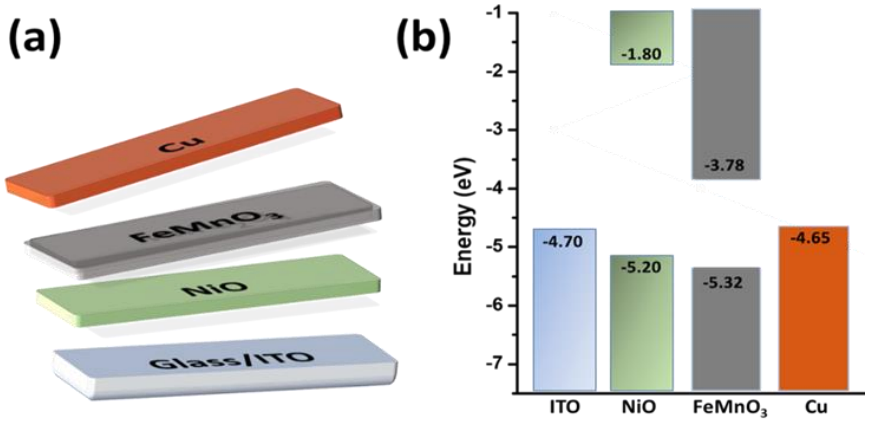

Figure 7.1 (a) Schematic representation, and (b) the corresponding energy level diagram of each component of the ITO/NiO/$FeMnO_3$/Cu device

The solar cell under study exhibited a high open circuit voltage of 1.31 V with sufficient fill factor of 54.3% and low short circuit current of 0.07 mA cm^{-2} resulting in a PCE of 0.05% under 100 mW cm^{-2} illumination (Table 8).

Table 8 Extracted solar cell parameters from the J–V characterization of the ITO/NiO/$FeMnO_3$/Cu device

Solar cell	V_{oc} (V)	J_{sc} (mA/cm^2)	FF (%)	PCE (%)
ITO/NiO/FMO/Cu	1.31	0.07	54.3	0.05

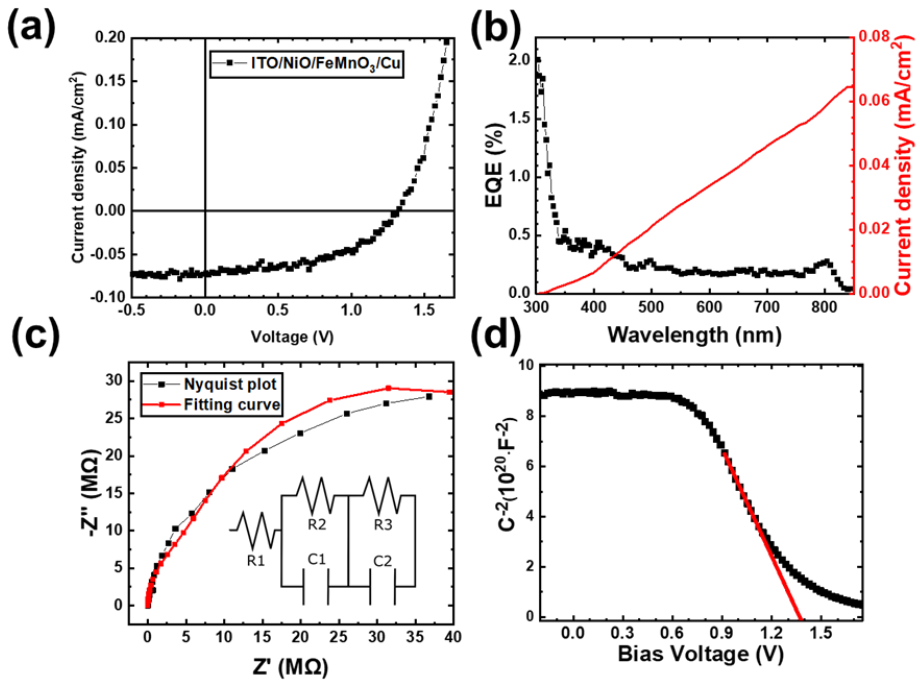

Figure 7.2 (a) J-V plot under illumination conditions for the representative p-n device under this study ITO/NiO/$FeMnO_3$/Cu. (b) EQE spectrum of NiO−$FeMnO_3$ (p−n) heterojunction sandwiched between ITO and Cu electrodes. The right axis represents the integrated photocurrent density of the corresponding device. (c) Nyquist, and (d) Mott–Schottky plots for the ITO/NiO/ $FeMnO_3$/Cu device.

Electrical characterization of the device revealed that the high charge transport resistance in a relative thick (~500 nm) n-type $FeMnO_3$ active layer limits the generated current. Optimizing the active layer thickness and improving the charge carrier transport properties can lead to $FeMnO_3$-based solar cells with higher delivering PCE. In parallel, incorporation of buffer layers within the ITO/NiO/$FeMnO_3$/Cu device structure can be used to improve charge carrier selectivity as well as a more appropriate n-type material can be applied with higher light harvesting capabilities and better aligned VB level edge to $FeMnO_3$ to facilitate the holes transfer.

Appendix A

A1. Publications related to this PhD Thesis

Ioannis T. Papadas, Apostolos Ioakeimidis, Gerasimos S. Armatas and Stelios A. Choulis, Low Temperature Combustion Synthesis of spinel $NiCo_2O_4$ Nanoparticles as Hole Selective Contact for p-i-n Perovskite Solar Cells, Advance Science, 2018, 1701029

Apostolos Ioakeimidis, Ioannis T. Papadas, Dimitris Tsikritzis, Gerasimos S. Armatas, Stella Kennou, Stelios A. Choulis Enhanced Photovoltaic Performance of Perovskite Solar Cells by Co-Doped Spinel Nickel Cobaltite Hole Transporting Layer , APL Materials 7, 021101 (2019)

Apostolos Ioakeimidis, Stelios A. Choulis, Nitrobenzene as Additive to Improve Reproducibility and Degradation Resistance of Highly Efficient Methylammonium-Free Inverted Perovskite Solar Cells, Apostolos Ioakeimidis, Stelios A. Choulis, Materials 2020, 13(15), 3289

Ioannis T. Papadas, Apostolos Ioakeimidis, Ioannis Vamvasakis, Polyvios Eleftheriou Gerasimos S. Armatas and Stelios A. Choulis, All-Inorganic p−n Heterojunction Solar Cells by Solution Combustion Synthesis using n-type FeMnO3 Perovskite Photoactive Layer, Frontiers in Chemistry., Published online 29 September 2021 | https://doi.org/10.3389/fchem.2021.754487

Apostolos Ioakeimidis, Ioannis T. Papadas, Eirini D. Koutsouroubi, Gerasimos S. Armatas & Stelios A. Choulis, Thermal Analysis of Metal-Organic Precursors for Functional Cu:NiOx Hole Transporting Layer in Inverted Perovskite Solar Cells: Role of Solution Combustion Chemistry in Cu:NiOx Thin Films Processing, Under Review, Nanomaterials, 2021

A2. Conference Presentations

Apostolos Ioakeimidis and Stelios A. Choulis, *Nitrobenzene as Additive to Improve Reproducibility and Degradation Resistance of Highly Efficient Methylammonium-Free Inverted Perovskite Solar Cells,* NanoGe Fall Meeting, Online conference, October 2020

Apostolos Ioakeimidis, Ioannis T. Papadas, Dimitris Tsikritzis, Gerasimos S. Armatas, Stella Kennou, Stelios A. Choulis, *Enhanced photovoltaic performance of perovskite solar cells by co-doped Spinel Nickel Cobaltite hole transporting layer*, next-gen IV:PV materials, June 2019, University of Groningen, Groningen, Netherlands.

A. Kottaras, D. Karageorgopoulos, S. Sakkopoulos, E. Vitoratos, **A. Ioakeimidis**, I. T. Papadas, S. A. Choulis *D.C. conductivity dependence of NiCo2O4 on thermal aging* XXXIII Panhellenic Conference on Solid State Physics and Materials Science University of Cyprus, 2018, Nicosia, Cyprus

Apostolos Ioakeimidis, Ioannis T. Papadas, Dimitris Tsikritzis, Gerasimos S. Armatas, Stella Kennou, Stelios A. Choulis, *Doped NiCo2O4 Spinel as Hole Transporting Layer For Highly Efficient Inverted perovskite solar cells*, XXXIII Panhellenic Conference on Solid State Physics and Materials Science University of Cyprus, 2018, Nicosia, Cyprus

I. T. Papadas, A. Ioakeimidis, S. M. Pozov, F. Galatopoulos, A. Z Chrusou and S. A. Choulis, *Materials and Device Engineering Concepts for High Performance Printed Photovoltaics*, EUTINN (workshop for the development of collaborations in the field of 'nano' in the broad sense amongst the partners of the EUt+), online Workshop (Organized by Université de Technologie de Troyes, France), 2021.

References

1. *Food, Energy, and Society, Third Edition*. (CRC Press, 2007). doi:10.1201/9781420046687

2. Smil, V. *Energy Transitions: History, Requirements, Prospects*. **1**, (ABC-CLIO, LLC, 2010).

3. Carbonnier, G. & Grinevald, J. Energy and Development. *Rev. Int. Polit. développement* **2**, (2011).

4. Our World in Data. Available at: https://ourworldindata.org/energy-mix. (Accessed: 13th September 2021)

5. Our World in Data. Available at: https://ourworldindata.org/emissions-by-fuel. (Accessed: 13th September 2021)

6. Baños, R. *et al.* Optimization methods applied to renewable and sustainable energy: A review. *Renew. Sustain. Energy Rev.* **15**, 1753–1766 (2011).

7. European Council. Council Directive 2009/28/EC of the European Parliament and of the Council of 23 April 2009 on the promotion of the use of energy from renewable sources and amending and subsequently repealing repealing Directives 2001/77/EC and 2003/30/EC. *Off. J. Eur. Union* **L 140/17**, 1–47 (2009).

8. Hepbasli, A. A key review on exergetic analysis and assessment of renewable energy resources for a sustainable future. *Renew. Sustain. Energy Rev.* **12**, 593–

661 (2008).

9. BP. 67 th edition Contents is one of the most widely respected. *Stat. Rev. World Energy* 1–56 (2018).

10. University, S. Global Climate & Energy Project An Assessment of Solar Energy Conversion Technologies and Research Opportunities. *Assessment* 1–20 (2006).

11. El Chaar, L., Lamont, L. A. & El Zein, N. Review of photovoltaic technologies. *Renew. Sustain. Energy Rev.* **15**, 2165–2175 (2011).

12. Agency, I. R. E. *Renewable Power Generation Costs in 2019*. *International Renewable Energy Agency* (2020).

13. Our World in Data. Available at: https://ourworldindata.org/grapher/installed-solar-pv-capacity?yScale=log&time=2000..2019&country=CHN~OWID_WRL~Europe~RUS~USA. (Accessed: 13th September 2021)

14. Dimroth, F. *et al.* Wafer bonded four-junction GaInP/GaAs//GaInAsP/GaInAs concentrator solar cells with 44.7% efficiency. *Prog. Photovoltaics Res. Appl.* **22**, 277–282 (2014).

15. Ansari, M. I. H., Qurashi, A. & Nazeeruddin, M. K. Frontiers, opportunities, and challenges in perovskite solar cells: A critical review. *J. Photochem. Photobiol. C Photochem. Rev.* **35**, 1–24 (2018).

16. Green, M. A. Third generation photovoltaics: Ultra-high conversion efficiency at low cost. *Prog. Photovoltaics Res. Appl.* **9**, 123–135 (2001).

17. Ibn-Mohammed, T. *et al.* Perovskite solar cells: An integrated hybrid lifecycle assessment and review in comparison with other photovoltaic technologies. *Renew. Sustain. Energy Rev.* **80**, 1321–1344 (2017).

18. Kojima, A., Teshima, K., Shirai, Y. & Miyasaka, T. Organometal Halide Perovskites as Visible-light Sensitizers for Photovoltaic Cells. *J. Am. Chem. Soc.* **131**, 6050–6051 (2009).

19. NREL. Best Research-Cell Efficiency Chart. (2019).

20. Gray, J. L. The Physics of the Solar Cell. in *Handbook of Photovoltaic Science and Engineering* 61–112 (John Wiley & Sons, Ltd, 2005). doi:10.1002/0470014008.ch3

21. Johnsson, M. & Lemmens, P. Crystallography and Chemistry of Perovskites. in *Handbook of Magnetism and Advanced Magnetic Materials* 1–11 (John Wiley & Sons, Ltd, 2007). doi:10.1002/9780470022184.hmm411

22. Kubicek, M., Bork, A. H. & Rupp, J. L. M. Perovskite oxides-a review on a versatile material class for solar-to-fuel conversion processes. *J. Mater. Chem. A* **5**, 11983–12000 (2017).

23. Chen, Y., Zhang, L., Zhang, Y., Gao, H. & Yan, H. Large-area perovskite solar cells-a review of recent progress and issues. *RSC Adv.* **8**, 10489–10508 (2018).

24. Stoumpos, C. C., Malliakas, C. D. & Kanatzidis, M. G. Semiconducting tin and lead iodide perovskites with organic cations: Phase transitions, high mobilities, and near-infrared photoluminescent properties. *Inorg. Chem.* **52**, 9019–9038 (2013).

25. Goldschmidt, V. M. Laws of crystal chemistry Naturwissenschaften. *Elsevier* **14**, 477–485 (1926).

26. Park, N.-G. Perovskite solar cells: an emerging photovoltaic technology. *Mater. Today* **18**, 65–72 (2015).

27. Calabrese, J. *et al.* Preparation and characterization of layered lead halide compounds. *J. Am. Chem. Soc.* **113**, 2328–2330 (1991).

28. Paritmongkol, W. *et al.* Synthetic Variation and Structural Trends in Layered Two-Dimensional Alkylammonium Lead Halide Perovskites. *Chem. Mater.* acs.chemmater.9b01318 (2019). doi:10.1021/acs.chemmater.9b01318

29. Zhou, Y., Huang, F., Cheng, Y.-B. & Gray-Weale, A. Photovoltaic performance and the energy landscape of CH 3 NH 3 PbI 3. *Phys. Chem. Chem. Phys.* **17**, 22604–22615 (2015).

30. Brandt, R. E., Stevanović, V., Ginley, D. S. & Buonassisi, T. Identifying defect-tolerant semiconductors with high minority-carrier lifetimes: beyond hybrid lead halide perovskites. *MRS Commun.* **5**, 265–275 (2015).

31. Yang, J.-P. *et al.* Band Dispersion and Hole Effective Mass of Methylammonium Lead Iodide Perovskite. *Sol. RRL* **2**, 1800132 (2018).

32. Giorgi, G., Fujisawa, J.-I., Segawa, H. & Yamashita, K. Small Photocarrier Effective Masses Featuring Ambipolar Transport in Methylammonium Lead Iodide Perovskite: A Density Functional Analysis. *J. Phys. Chem. Lett.* **4**, 4213–4216 (2013).

33. Motta, C. *et al.* Revealing the role of organic cations in hybrid halide perovskite

CH3NH3PbI3. *Nat. Commun.* **6**, 7026 (2015).

34. Saidaminov, M. I. *et al.* High-quality bulk hybrid perovskite single crystals within minutes by inverse temperature crystallization. *Nat. Commun.* **6**, 7586 (2015).

35. Green, M. a., Ho-Baillie, A. & Snaith, H. J. The emergence of perovskite solar cells. *Nat. Photonics* **8**, 506–514 (2014).

36. Huang, H., Bodnarchuk, M. I., Kershaw, S. V., Kovalenko, M. V. & Rogach, A. L. Lead Halide Perovskite Nanocrystals in the Research Spotlight: Stability and Defect Tolerance. *ACS Energy Lett.* **2**, 2071–2083 (2017).

37. Wang, Q. *et al.* Qualifying composition dependent p and n self-doping in CH 3 NH 3 PbI 3. *Appl. Phys. Lett.* **105**, 163508 (2014).

38. Lim, J. *et al.* Elucidating the long-range charge carrier mobility in metal halide perovskite thin films. *Energy Environ. Sci.* **12**, 169–176 (2019).

39. Noh, J. H., Im, S. H., Heo, J. H., Mandal, T. N. & Seok, S. Il. Chemical management for colorful, efficient, and stable inorganic-organic hybrid nanostructured solar cells. *Nano Lett.* **13**, 1764–1769 (2013).

40. Zhang, X., Li, L., Sun, Z. & Luo, J. Rational chemical doping of metal halide perovskites. *Chem. Soc. Rev.* **48**, 517–539 (2019).

41. Liu, S. *et al.* A Review on Additives for Halide Perovskite Solar Cells. *Adv. Energy Mater.* **1902492**, 1–28 (2019).

42. Yang, J. *et al.* A review on improving the quality of Perovskite Films in

Perovskite Solar Cells via the weak forces induced by additives. *Appl. Sci.* **9**, (2019).

43. Mangrulkar, M. & Stevenson, K. J. The Progress of Additive Engineering for CH 3 NH 3 PbI 3 Photo-Active Layer in the Context of Perovskite Solar Cells. (2021).

44. Collavini, S., Cabrera-Espinoza, A. & Delgado, J. L. Organic Polymers as Additives in Perovskite Solar Cells. *Macromolecules* **54**, 5451–5463 (2021).

45. Liang, P. W. *et al.* Additive enhanced crystallization of solution-processed perovskite for highly efficient planar-heterojunction solar cells. *Adv. Mater.* **26**, 3748–3754 (2014).

46. Shen, C. *et al.* Stabilizing Formamidinium Lead Iodide Perovskite by Sulfonyl-Functionalized Phenethylammonium Salt via Crystallization Control and Surface Passivation. *Sol. RRL* 2000069 (2020). doi:10.1002/solr.202000069

47. Jeon, N. J. *et al.* Solvent engineering for high-performance inorganic-organic hybrid perovskite solar cells. *Nat. Mater.* **13**, 1–7 (2014).

48. McMeekin, D. P. *et al.* A mixed-cation lead mixed-halide perovskite absorber for tandem solar cells. *Science (80-.).* **351**, 151–155 (2016).

49. Hao, F., Stoumpos, C. C., Cao, D. H., Chang, R. P. H. & Kanatzidis, M. G. Lead-free solid-state organic-inorganic halide perovskite solar cells. *Nat. Photonics* **8**, 489–494 (2014).

50. Eperon, G. E., Burlakov, V. M., Docampo, P., Goriely, A. & Snaith, H. J. Morphological control for high performance, solution-processed planar

heterojunction perovskite solar cells. *Adv. Funct. Mater.* **24**, 151–157 (2014).

51. Saliba, M. *et al.* Incorporation of rubidium cations into perovskite solar cells improves photovoltaic performance. *Science (80-.).* **354**, 206–209 (2016).

52. Jeon, N. J. *et al.* Compositional engineering of perovskite materials for high-performance solar cells. *Nature* **517**, 476–480 (2015).

53. Liu, M., Johnston, M. B. & Snaith, H. J. Efficient planar heterojunction perovskite solar cells by vapour deposition. *Nature* **501**, 395–8 (2013).

54. Liu, D. & Kelly, T. L. Perovskite solar cells with a planar heterojunction structure prepared using room-temperature solution processing techniques. *Nat. Photonics* **8**, 133–138 (2014).

55. Burschka, J. *et al.* Sequential deposition as a route to high-performance perovskite-sensitized solar cells. *Nature* **499**, 316–319 (2013).

56. Chen, Q. *et al.* Planar heterojunction perovskite solar cells via vapor-assisted solution process. *J. Am. Chem. Soc.* **136**, 622–625 (2014).

57. Bi, D. *et al.* Using a two-step deposition technique to prepare perovskite (CH3NH3PbI3) for thin film solar cells based on ZrO2 and TiO2 mesostructures. *RSC Adv.* **3**, 18762 (2013).

58. Huang, F. *et al.* Gas-assisted preparation of lead iodide perovskite films consisting of a monolayer of single crystalline grains for high efficiency planar solar cells. *Nano Energy* **10**, 10–18 (2014).

59. Li, X. *et al.* A vacuum flash-assisted solution process for high-efficiency large-

area perovskite solar cells. *Science (80-.).* **353**, 58–62 (2016).

60. Chen, C. W. *et al.* Efficient and uniform planar-type perovskite solar cells by simple sequential vacuum deposition. *Adv. Mater.* **26**, 6647–6652 (2014).

61. Ioakeimidis, A., Christodoulou, C., Lux-Steiner, M. & Fostiropoulos, K. Effect of PbI2deposition rate on two-step PVD/CVD all-vacuum prepared perovskite. *J. Solid State Chem.* **244**, 20–24 (2016).

62. Abbas, H. A. *et al.* High efficiency sequentially vapor grown n-i-p CH3NH3PbI3 perovskite solar cells with undoped P3HT as p-type heterojunction layer. *APL Mater.* **3**, (2015).

63. Docampo, P., Ball, J. M., Darwich, M., Eperon, G. E. & Snaith, H. J. Efficient organometal trihalide perovskite planar-heterojunction solar cells on flexible polymer substrates. *Nat. Commun.* **4**, 2761 (2013).

64. Conings, B. *et al.* Perovskite-based hybrid solar cells exceeding 10% efficiency with high reproducibility using a thin film sandwich approach. *Adv. Mater.* **26**, 2041–2046 (2014).

65. Zhou, H. P. *et al.* Interface engineering of highly efficient perovskite solar cells. *Science (80-.).* **345**, 542–546 (2014).

66. Im, J.-H., Lee, C.-R., Lee, J.-W., Park, S.-W. & Park, N.-G. 6.5% Efficient Perovskite Quantum-Dot-Sensitized Solar Cell. *Nanoscale* **3**, 4088 (2011).

67. Kim, H.-S. *et al.* Lead Iodide Perovskite Sensitized All-Solid-State Submicron Thin Film Mesoscopic Solar Cell with Efficiency Exceeding 9%. *Sci. Rep.* **2**, 591 (2012).

68. Polander, L. E. *et al.* Hole-transport material variation in fully vacuum deposited perovskite solar cells. *APL Mater.* **2**, 081503 (2014).

69. Malinkiewicz, O. *et al.* Perovskite solar cells employing organic charge-transport layers. *Nat. Photonics* **8**, 128–132 (2014).

70. Ye, M. *et al.* Recent advances in interfacial engineering of perovskite solar cells. *J. Phys. D. Appl. Phys.* **50**, 373002 (2017).

71. Zardetto, V. *et al.* Atomic layer deposition for perovskite solar cells: research status, opportunities and challenges. *Sustain. Energy Fuels* **1**, 30–55 (2017).

72. Bakr, Z. H. *et al.* Advances in hole transport materials engineering for stable and efficient perovskite solar cells. *Nano Energy* **34**, 271–305 (2017).

73. Wen, T. Y. *et al.* Surface Electronic Modification of Perovskite Thin Film with Water-Resistant Electron Delocalized Molecules for Stable and Efficient Photovoltaics. *Adv. Energy Mater.* **8**, 1703143 (2018).

74. Ouyang, D. *et al.* Strategic Synthesis of Ultrasmall NiCo 2 O 4 NPs as Hole Transport Layer for Highly Efficient Perovskite Solar Cells. *Adv. Energy Mater.* **8**, 1702722 (2018).

75. Li, M.-H., Shen, P.-S., Wang, K.-C., Guo, T.-F. & Chen, P. Inorganic p-type contact materials for perovskite-based solar cells. *J. Mater. Chem. A* **3**, 9011–9019 (2015).

76. Bi, C. *et al.* Non-wetting surface-driven high-aspect-ratio crystalline grain growth for efficient hybrid perovskite solar cells. *Nat. Commun.* **6**, 7747 (2015).

77. Nishihara, Y., Chikamatsu, M., Kazaoui, S., Miyadera, T. & Yoshida, Y. Influence of O2 plasma treatment on NiO x layer in perovskite solar cells. *Jpn. J. Appl. Phys.* **57**, 04FS07 (2018).

78. Liang, Q. *et al.* Enhancing the crystallization and optimizing the orientation of perovskite films via controlling nucleation dynamics. *J. Mater. Chem. A* **4**, 223–232 (2016).

79. Climent-Pascual, E. *et al.* Influence of the substrate on the bulk properties of hybrid lead halide perovskite films. *J. Mater. Chem. A* **4**, 18153–18163 (2016).

80. Lilliu, S. *et al.* Mapping Morphological and Structural Properties of Lead Halide Perovskites by Scanning Nanofocus XRD. *Adv. Funct. Mater.* **26**, 8221–8230 (2016).

81. Olthof, S. & Meerholz, K. Substrate-dependent electronic structure and film formation of MAPbI3 perovskites. *Sci. Rep.* **7**, 40267 (2017).

82. Miller, E. M. *et al.* Substrate-controlled band positions in CH 3 NH 3 PbI 3 perovskite films. *Phys. Chem. Chem. Phys.* **16**, 22122–22130 (2014).

83. Schulz, P. *et al.* Electronic Level Alignment in Inverted Organometal Perovskite Solar Cells. *Adv. Mater. Interfaces* **2**, 1400532 (2015).

84. Pitchaiya, S. *et al.* A review on the classification of organic/inorganic/carbonaceous hole transporting materials for perovskite solar cell application. *Arab. J. Chem.* (2018). doi:10.1016/j.arabjc.2018.06.006

85. Schulz, P., Cahen, D. & Kahn, A. Halide perovskites: Is it all about the interfaces? 1–181 (2018).

86. Fu, Q. *et al.* Recent Progress on the Long-Term Stability of Perovskite Solar Cells. *Adv. Sci.* **5**, 1700387 (2018).

87. Liu, J. *et al.* A dopant-free hole-transporting material for efficient and stable perovskite solar cells. *Energy Environ. Sci.* **7**, 2963–2967 (2014).

88. Huang, D. *et al.* Perovskite solar cells with a DMSO-treated PEDOT:PSS hole transport layer exhibit higher photovoltaic performance and enhanced durability. *Nanoscale* **9**, 4236–4243 (2017).

89. Snaith, H. J. & Grätzel, M. Enhanced charge mobility in a molecular hole transporter via addition of redox inactive ionic dopant: Implication to dye-sensitized solar cells. *Appl. Phys. Lett.* **89**, 262114 (2006).

90. Abate, A. *et al.* Lithium salts as "redox active" p-type dopants for organic semiconductors and their impact in solid-state dye-sensitized solar cells. *Phys. Chem. Chem. Phys.* **15**, 2572–2579 (2013).

91. Tang, L. J. *et al.* A Solution-Processed Transparent NiO Hole-Extraction Layer for High-Performance Inverted Perovskite Solar Cells. *Chem. - A Eur. J.* **24**, 2845–2849 (2018).

92. Christians, J. A., Fung, R. C. M. & Kamat, P. V. An Inorganic Hole Conductor for Organo-Lead Halide Perovskite Solar Cells. Improved Hole Conductivity with Copper Iodide. *J. Am. Chem. Soc.* **136**, 758–764 (2014).

93. Wijeyasinghe, N. *et al.* Copper(I) Thiocyanate (CuSCN) Hole-Transport Layers Processed from Aqueous Precursor Solutions and Their Application in Thin-Film Transistors and Highly Efficient Organic and Organometal Halide

Perovskite Solar Cells. *Adv. Funct. Mater.* **27**, 1701818 (2017).

94. Zhang, H. *et al.* Low-Temperature Solution-Processed CuCrO 2 Hole-Transporting Layer for Efficient and Photostable Perovskite Solar Cells. *Adv. Energy Mater.* **8**, 1702762 (2018).

95. Chen, L.-C. *et al.* Nano-structured CuO-Cu2O Complex Thin Film for Application in CH3NH3PbI3 Perovskite Solar Cells. *Nanoscale Res. Lett.* **11**, 402 (2016).

96. Habisreutinger, S. N. *et al.* Carbon Nanotube/Polymer Composites as a Highly Stable Hole Collection Layer in Perovskite Solar Cells. *Nano Lett.* **14**, 5561–5568 (2014).

97. Yeo, J.-S. *et al.* Highly efficient and stable planar perovskite solar cells with reduced graphene oxide nanosheets as electrode interlayer. *Nano Energy* **12**, 96–104 (2015).

98. Chen, W. *et al.* Understanding the Doping Effect on NiO: Toward High-Performance Inverted Perovskite Solar Cells. *Adv. Energy Mater.* **8**, 1703519 (2018).

99. Kim, J. H. *et al.* High-Performance and Environmentally Stable Planar Heterojunction Perovskite Solar Cells Based on a Solution-Processed Copper-Doped Nickel Oxide Hole-Transporting Layer. *Adv. Mater.* **27**, 695–701 (2015).

100. Qiu, Z. *et al.* Enhanced physical properties of pulsed laser deposited NiO films via annealing and lithium doping for improving perovskite solar cell efficiency. *J. Mater. Chem. C* **5**, 7084–7094 (2017).

101. Chen, W. *et al.* Cesium Doped NiOx as an Efficient Hole Extraction Layer for Inverted Planar Perovskite Solar Cells. *Adv. Energy Mater.* **7**, 1700722 (2017).

102. Wei, Y. *et al.* Improving the efficiency and environmental stability of inverted planar perovskite solar cells via silver-doped nickel oxide hole-transporting layer. *Appl. Surf. Sci.* **427**, 782–790 (2018).

103. Huang, A. B. *et al.* Achieving high-performance planar perovskite solar cells with co-sputtered Co-doping NiOx hole transport layers by efficient extraction and enhanced mobility. *J. Mater. Chem. C* **4**, 10839–10846 (2016).

104. Qin, P.-L. *et al.* Copper-Doped Chromium Oxide Hole-Transporting Layer for Perovskite Solar Cells: Interface Engineering and Performance Improvement. *Adv. Mater. Interfaces* **3**, 1500799 (2016).

105. Li, G. *et al.* Overcoming the Limitations of Sputtered Nickel Oxide for High-Efficiency and Large-Area Perovskite Solar Cells. *Adv. Sci.* **4**, 1700463 (2017).

106. Jung, J. W., Chueh, C. C. & Jen, A. K. Y. A Low-Temperature, Solution-Processable, Cu-Doped Nickel Oxide Hole-Transporting Layer via the Combustion Method for High-Performance Thin-Film Perovskite Solar Cells. *Adv. Mater.* **27**, 7874–7880 (2015).

107. Han, W. *et al.* Improving the performance of perovskite solar cells by surface passivation. *J. Energy Chem.* **46**, 202–207 (2020).

108. He, J. *et al.* Improvement of red light harvesting ability and open circuit voltage of Cu:NiOx based p-i-n planar perovskite solar cells boosted by cysteine enhanced interface contact. *Nano Energy* **45**, 471–479 (2018).

109. Kim, H. S. *et al.* Effect of cs-incorporated NiOx on the performance of perovskite solar cells. *ACS Omega* **2**, 9074–9079 (2017).

110. Liu, Z. *et al.* High-Performance Planar Perovskite Solar Cells Using Low Temperature, Solution–Combustion-Based Nickel Oxide Hole Transporting Layer with Efficiency Exceeding 20%. *Adv. Energy Mater.* **8**, 1–9 (2018).

111. Thiruchelvan, P. S., Lai, C. C. & Tsai, C. H. Combustion processed nickel oxide and zinc doped nickel oxide thin films as a hole transport layer for perovskite solar cells. *Coatings* **11**, (2021).

112. Liu, Y. *et al.* Cu-doped nickel oxide hole transporting layer via efficient low-temperature spraying combustion method for perovskite solar cells. *J. Mater. Sci. Mater. Electron.* **30**, 15627–15635 (2019).

113. Cochran, E. A. *et al.* Role of Combustion Chemistry in Low-Temperature Deposition of Metal Oxide Thin Films from Solution. *Chem. Mater.* **29**, 9480–9488 (2017).

114. Roura, P. *et al.* Thermal analysis of metal organic precursors for functional oxide preparation: Thin films versus powders. *Thermochim. Acta* **601**, 1–8 (2015).

115. Sánchez-Rodriguez, D., Farjas, J. & Roura, P. The critical conditions for thermal explosion in a system heated at a constant rate. *Combust. Flame* **186**, 211–219 (2017).

116. Sánchez-Rodríguez, D., Eloussifi, H., Farjas, J., Roura, P. & Dammak, M. Thermal gradients in thermal analysis experiments: Criterions to prevent inaccuracies when determining sample temperature and kinetic parameters.

Thermochim. Acta **589**, 37–46 (2014).

117. Sanchez-Rodriguez, D. *et al.* Thermal analysis for low temperature synthesis of oxide thin films from chemical solutions. *J. Phys. Chem. C* **117**, 20133–20138 (2013).

118. Cochran, E. A., Woods, K. N., Johnson, D. W., Page, C. J. & Boettcher, S. W. Unique chemistries of metal-nitrate precursors to form metal-oxide thin films from solution: Materials for electronic and energy applications. *J. Mater. Chem. A* **7**, 24124–24149 (2019).

119. Liu, M.-H. *et al.* p-type Li, Cu-codoped NiOx hole-transporting layer for efficient planar perovskite solar cells. *Opt. Express* **24**, A1349 (2016).

120. Chen, W. *et al.* Efficient and stable large-area perovskite solar cells with inorganic charge extraction layers. *Science (80-.).* **350**, 944–948 (2015).

121. Xia, X. *et al.* Lithium and Silver Co-Doped Nickel Oxide Hole-Transporting Layer Boosting the Efficiency and Stability of Inverted Planar Perovskite Solar Cells. *ACS Appl. Mater. Interfaces* **10**, 44501–44510 (2018).

122. Schutt, K. *et al.* Overcoming Zinc Oxide Interface Instability with a Methylammonium-Free Perovskite for High-Performance Solar Cells. *Adv. Funct. Mater.* (2019). doi:10.1002/adfm.201900466

123. Kim, H. S. *et al.* Control of I-V Hysteresis in CH3NH3PbI3 Perovskite Solar Cell. *J. Phys. Chem. Lett.* **6**, 4633–4639 (2015).

124. Guerrero, A. *et al.* Properties of Contact and Bulk Impedances in Hybrid Lead Halide Perovskite Solar Cells Including Inductive Loop Elements. *J. Phys.*

Chem. C **120**, 8023–8032 (2016).

125. Guerrero, A. *et al.* Interfacial Degradation of Planar Lead Halide Perovskite Solar Cells. *ACS Nano* **10**, 218–224 (2016).

126. Stolterfoht, M. *et al.* Approaching the fill factor Shockley–Queisser limit in stable, dopant-free triple cation perovskite solar cells. *Energy Environ. Sci.* **10**, 1530–1539 (2017).

127. Zarazua, I., Bisquert, J. & Garcia-Belmonte, G. Light-Induced Space-Charge Accumulation Zone as Photovoltaic Mechanism in Perovskite Solar Cells. *J. Phys. Chem. Lett.* **7**, 525–528 (2016).

128. Papadas, I. T., Ioakeimidis, A., Armatas, G. S. & Choulis, S. A. Low-Temperature Combustion Synthesis of a Spinel NiCo 2 O 4 Hole Transport Layer for Perovskite Photovoltaics. *Adv. Sci.* **5**, 1701029 (2018).

129. Guerrero, A. *et al.* Properties of Contact and Bulk Impedances in Hybrid Lead Halide Perovskite Solar Cells Including Inductive Loop Elements. *J. Phys. Chem. C* **120**, 8023–8032 (2016).

130. Kim, H.-S. *et al.* Control of I – V Hysteresis in CH 3 NH 3 PbI 3 Perovskite Solar Cell. *J. Phys. Chem. Lett.* **6**, 4633–4639 (2015).

131. Kim, J.-H., Lee, H. Y. & Lee, J.-Y. Characteristics of the Li–Ni Doped Cobalt Oxide Thin Films Prepared by Pulsed Laser Deposition. *J. Nanosci. Nanotechnol.* **18**, 2021–2025 (2018).

132. Boix, P. P. *et al.* Determination of gap defect states in organic bulk heterojunction solar cells from capacitance measurements. *Appl. Phys. Lett.* **95**,

233302 (2009).

133. Zhao, D. *et al.* High-Efficiency Solution-Processed Planar Perovskite Solar Cells with a Polymer Hole Transport Layer. *Adv. Energy Mater.* **5**, 1401855 (2015).

134. Shockley, W. & Read, W. T. Statistics of the Recombinations of Holes and Electrons. *Phys. Rev.* **87**, 835–842 (1952).

135. Hall, R. N. Electron-Hole Recombination in Germanium. *Phys. Rev.* **87**, 387–387 (1952).

136. Mandoc, M. M., Kooistra, F. B., Hummelen, J. C., de Boer, B. & Blom, P. W. M. Effect of traps on the performance of bulk heterojunction organic solar cells. *Appl. Phys. Lett.* **91**, 263505 (2007).

137. Cowan, S. R., Roy, A. & Heeger, A. J. Recombination in polymer-fullerene bulk heterojunction solar cells. *Phys. Rev. B* **82**, 245207 (2010).

138. Marco, J. F. *et al.* Characterization of the Nickel Cobaltite, NiCo2O4, Prepared by Several Methods: An XRD, XANES, EXAFS, and XPS Study. *J. Solid State Chem.* **153**, 74–81 (2000).

139. Chuang, T. J., Brundle, C. R. & Rice, D. W. Interpretation of the x-ray photoemission spectra of cobalt oxides and cobalt oxide surfaces. *Surf. Sci.* **59**, 413–429 (1976).

140. Tavares, A. C., Cartaxo, M. A. M., da Silva Pereira, M. I. & Costa, F. M. Electrochemical study of spinel oxide systems with nominal compositions Ni 1− x Cu x Co 2 O 4 and NiCo 2− y Cu y O 4. *J. Solid State Electrochem.* **5**, 57–67 (2001).

141. Tavares, a. C., Cartaxo, M. a M., Da Silva Pereira, M. I. & Costa, F. M. Effect of the partial replacement of Ni or Co by Cu on the electrocatalytic activity of the NiCo2O4 spinel oxide. *J. Electroanal. Chem.* **464**, 187–197 (1999).

142. Tavares, A. . *et al.* XPS and voltammetric studies on Ni1−xCuxCo2O4 spinel oxide electrodes. *J. Electroanal. Chem.* **449**, 91–100 (1998).

143. Salgueiro, D. *et al.* Solution based zinc tin oxide TFTs: The dual role of the organic solvent. *J. Phys. D. Appl. Phys.* **50**, (2017).

144. Varma, A., Mukasyan, A. S., Rogachev, A. S. & Manukyan, K. V. Solution Combustion Synthesis of Nanoscale Materials. *Chem. Rev.* **116**, 14493–14586 (2016).

145. Singh, A., Gupta, S. K. & Garg, A. Inkjet printing of NiO films and integration as hole transporting layers in polymer solar cells. *Sci. Rep.* **7**, 1–12 (2017).

146. McMeekin, D. P. *et al.* Crystallization Kinetics and Morphology Control of Formamidinium–Cesium Mixed-Cation Lead Mixed-Halide Perovskite via Tunability of the Colloidal Precursor Solution. *Adv. Mater.* **29**, (2017).

147. Rahimnejad, S., Kovalenko, A., Forés, S. M., Aranda, C. & Guerrero, A. Coordination Chemistry Dictates the Structural Defects in Lead Halide Perovskites. *ChemPhysChem* 2795–2798 (2016). doi:10.1002/cphc.201600575

148. Guo, X. *et al.* Identification and characterization of the intermediate phase in hybrid organic-inorganic MAPbI3 perovskite. *Dalt. Trans.* **45**, 3806–3813 (2016).

149. Yan, K. *et al.* Hybrid Halide Perovskite Solar Cell Precursors: Colloidal

Chemistry and Coordination Engineering behind Device Processing for High Efficiency. *J. Am. Chem. Soc.* **137**, 4460–4468 (2015).

150. Li, B. *et al.* Constructing water-resistant CH3NH3PbI3 perovskite films: Via coordination interaction. *J. Mater. Chem. A* **4**, 17018–17024 (2016).

151. Wu, T. *et al.* Solvent engineering for high-quality perovskite solar cell with an efficiency approaching 20%. *J. Power Sources* **365**, 1–6 (2017).

152. Fei, C. *et al.* Controlled growth of textured perovskite films towards high performance solar cells. *Nano Energy* **27**, 17–26 (2016).

153. Cao, X. *et al.* Fabrication of Perovskite Films with Large Columnar Grains via Solvent-Mediated Ostwald Ripening for Efficient Inverted Perovskite Solar Cells. *ACS Appl. Energy Mater.* **1**, 868–875 (2018).

154. Fei, C. *et al.* Highly Efficient and Stable Perovskite Solar Cells Based on Monolithically Grained CH3NH3PbI3 Film. *Adv. Energy Mater.* **7**, 1–10 (2017).

155. Liu, C. *et al.* Grain Boundary Modification via F4TCNQ to Reduce Defects of Perovskite Solar Cells with Excellent Device Performance. *ACS Appl. Mater. Interfaces* **10**, 1909–1916 (2018).

156. Chaudhary, B. *et al.* Mixed-Dimensional Naphthylmethylammoinium-Methylammonium Lead Iodide Perovskites with Improved Thermal Stability. *Sci. Rep.* **10**, 1–11 (2020).

157. Zhang, H. *et al.* Improving the stability and performance of perovskite solar cells: Via off-the-shelf post-device ligand treatment. *Energy Environ. Sci.* **11**, 2253–2262 (2018).

158. Wu, Y. *et al.* Retarding the crystallization of PbI 2 for highly reproducible planar-structured perovskite solar cells via sequential deposition. *Energy Environ. Sci.* **7**, 2934 (2014).

159. Lee, J. W. *et al.* A Bifunctional Lewis Base Additive for Microscopic Homogeneity in Perovskite Solar Cells. *Chem* **3**, 290–302 (2017).

160. Mei, A. *et al.* A hole-conductor–free, fully printable mesoscopic perovskite solar cell with high stability. *Science (80-.).* **345**, 295–298 (2014).

161. Howard, J. M. *et al.* Humidity-Induced Photoluminescence Hysteresis in Variable Cs/Br Ratio Hybrid Perovskites. *J. Phys. Chem. Lett.* **9**, 3463–3469 (2018).

162. Barbé, J. *et al.* Localized effect of PbI2 excess in perovskite solar cells probed by high-resolution chemical-optoelectronic mapping. *J. Mater. Chem. A* **6**, 23010–23018 (2018).

163. Wang, Q. *et al.* Scaling Behavior of Moisture-induced Grain Degradation in Polycrystalline Hybrid Perovskite Thin Films(SUPP).

164. Yun, J. S. *et al.* Humidity-Induced Degradation via Grain Boundaries of HC(NH2)2PbI3 Planar Perovskite Solar Cells. *Adv. Funct. Mater.* **28**, 1–8 (2018).

165. Wang, M. *et al.* Improving the Performance and Reproducibility of Inverted Planar Perovskite Solar Cells Using Tetraethyl Orthosilicate as the Antisolvent. *ACS Appl. Mater. Interfaces* **11**, 3909–3916 (2019).

166. Yun, S. C. *et al.* Amino acid salt-driven planar hybrid perovskite solar cells with

enhanced humidity stability. *Nano Energy* **59**, 481–491 (2019).

167. Wu, T. *et al.* Efficient and stable tin-based perovskite solar cells by introducing π-conjugated Lewis base. *Sci. China Chem.* **63**, 107–115 (2020).

168. Wang, F. *et al.* Phenylalkylamine Passivation of Organolead Halide Perovskites Enabling High-Efficiency and Air-Stable Photovoltaic Cells. *Adv. Mater.* **28**, 9986–9992 (2016).

169. Mazumdar, S., Zhao, Y. & Zhang, X. Stability of Perovskite Solar Cells: Degradation Mechanisms and Remedies. *Front. Electron.* **2**, 1–34 (2021).